Master Thesis

Mechanical properties and thermal stability of non-reactively sputtered Ti-Al-N coatings

carried out for the purpose of obtaining the degree of Dipl.-Ing.,
submitted at TU Wien, Faculty of Mechanical and Industrial Engineering,
by

Sarah Christine Bermanschläger
Matriculation number: 01626114

under the supervision of

Univ.Prof. Dipl.-Ing. Dr.mont. Paul Heinz Mayrhofer
and
Univ.Ass. Dipl.-Ing. Bálint István Hajas, BSc

Institute of Material Sciences and Technology, E308

Vienna, November 2023

Die approbierte gedruckte Originalversion dieser Diplomarbeit ist an der TU Wien Bibliothek verfügbar
The approved original version of this thesis is available in print at TU Wien Bibliothek.
TU WIEN Bibliothek Your knowledge hub

Die approbierte gedruckte Originalversion dieser Diplomarbeit ist an der TU Wien Bibliothek verfügbar
The approved original version of this thesis is available in print at TU Wien Bibliothek.
TU WIEN Bibliothek Your knowledge hub

Die approbierte gedruckte Originalversion dieser Diplomarbeit ist an der TU Wien Bibliothek verfügbar
The approved original version of this thesis is available in print at TU Wien Bibliothek.
TU Bibliothek WIEN Your knowledge hub

I confirm that going to press of this thesis
needs the confirmation of the examination committee.

Affidavit

I declare in lieu of oath, that I wrote this thesis and performed the associated research myself, using only literature cited in this volume. If text passages from sources are used literally, they are marked as such.

I confirm that this work is original and has not been submitted elsewhere for any examination, nor is it currently under consideration for a thesis elsewhere.

I acknowledge that the submitted work will be checked electronically-technically using suitable and state-of-the-art means (plagiarism detection software). On the one hand, this ensures that the submitted work was prepared according to the high-quality standards within the applicable rules to ensure good scientific practice "Code of Conduct" at the TU Wien. On the other hand, a comparison with other student theses avoids violations of my personal copyright.

City and Date *Signature*

Die approbierte gedruckte Originalversion dieser Diplomarbeit ist an der TU Wien Bibliothek verfügbar
The approved original version of this thesis is available in print at TU Wien Bibliothek.
TU WIEN Bibliothek Your knowledge hub

Acknowledgements

I would like to express my sincerest gratitude to my supervisors, without whom this thesis would still be a blank sheet of paper. To **Bálint**, who is the most helpful person I know and who finds a solution to every problem. Who supported me at any time of the day and never got tired of answering my questions. And thank you for your endless supply of cookies, they save lives! I also thank **Paul**, who brings so much motivation and joy to his field of research that it would be enough for two people. His knowledge and experience always showed me new aspects of thin-film technology, whether it was in a lecture hall or in a personal conversation. If more lecturers were like you, the university would be a much more interesting place.

I would also like to thank **Kathi**, my partner in crime/thin films. Knowing that there is someone out there going through the exact same thing, whether it was long hours in the lab or trying to get an image out of the SEM, was incredibly helpful and encouraging. I hope it was the same for you.

My thanks go to the entire **research group**, who made me feel welcome and were always available for a good lunch or good advice about my work. They also go to all those who have taken the time to explain to me how various machines work or who have supported me in my research.

Last but not least, I would like to thank my friends and family who, although they understood very little of my work, took the effort to read it and give me advice. Throughout my career, they have given me the strength to keep going and created a good balance to the stress of everyday university life. Special thanks go to **Roland**, who never tires of encouraging me and showing me that everything is not so bad at all.

Die approbierte gedruckte Originalversion dieser Diplomarbeit ist an der TU Wien Bibliothek verfügbar
The approved original version of this thesis is available in print at TU Wien Bibliothek.
TU WIEN Bibliothek Your knowledge hub

Die approbierte gedruckte Originalversion dieser Diplomarbeit ist an der TU Wien Bibliothek verfügbar
The approved original version of this thesis is available in print at TU Wien Bibliothek.
TU WIEN Bibliothek Your knowledge hub

Table of Contents

Abstract III

Kurzfassung IV

List of Figures.. VI

List of Tables XIII

List of Abbreviations and Symbols XIV

1 Introduction..1

2 Titanium Aluminum Nitride 3

3 Physical Vapor Deposition 6

3.1 Sputter Deposition...6

3.1.1 Plasma Generation...7

3.1.2 Magnetron Sputtering...9

3.2 Experimental Implementation...10

4 Film Growth and Structure 14

4.1 Nucleation..14

4.2 Growth...15

4.3 Structure Zone Models – SZM 17

5 Characterization – Methods and Parameters 20

5.1 Hardness and Elastic Modulus...20

5.2 X-Ray Diffraction – XRD 24

5.3 Electron Microscopy 28

5.3.1 Scanning Electron Microscopy – SEM 28

5.3.2 (Scanning) Transmission Electron Microscopy – (S)TEM 32

5.3.3 Energy Dispersive X-Ray Spectroscopy – EDX..35

5.3.4 Electron Energy Loss Spectroscopy – EELS..39

5.4 Elastic Recoil Detection Analysis – ERDA...40

6 Results and Discussion 41

6.1 Deposition Rate..41

6.2 Analysis of the Cross Section 43

Die approbierte gedruckte Originalversion dieser Diplomarbeit ist an der TU Wien Bibliothek verfügbar
The approved original version of this thesis is available in print at TU Wien Bibliothek.
TU WIEN Bibliothek Your knowledge hub

6.3 Chemical Composition 51
6.3.1 EDX 51
6.3.2 EELS 55
6.3.3 ERDA 56
6.4 Crystallographic Properties 58
6.4.1 Crystal Structure – Diffractogram Analysis 58
6.4.2 Crystal Structure – TEM Analysis 70
6.5 Mechanical Properties 74
6.6 Thermal Stability 79
6.6.1 Appearance of the Surface after Annealing 79
6.6.2 Crystal Structure during and after Annealing 82
6.6.3 Mechanical Properties after Annealing 89
7 Summary and Conclusion 91
References 94
Appendices 97

Die approbierte gedruckte Originalversion dieser Diplomarbeit ist an der TU Wien Bibliothek verfügbar
The approved original version of this thesis is available in print at TU Wien Bibliothek.
TU WIEN Bibliothek Your knowledge hub

Abstract

Non-reactive magnetron sputtering of titanium aluminum nitride Ti-Al-N has been little studied despite some advantages over the reactive variant. For example, the so-called "poisoning" effect does not occur, which can sometimes severely hinder the sputtering and deposition process. This thesis addresses the question of the effects of non-reactive sputtering on the properties of Ti-Al-N coatings. For this purpose, three different targets with the following compositions were selected: $Ti_{0.5}Al_{0.5}N$ (50/50), $Ti_{0.33}Al_{0.67}N$ (33/67) and $Ti_{0.2}Al_{0.8}N$ (20/80). At different substrate temperatures (no additional heating, 200 °C, 300 °C, 450 °C and 600 °C), the depositions were performed with direct current or bipolar pulsed direct current (50 kHz and 250 kHz) sputtering.

The direct current mode has been shown to be favorable for the depositions of the 50/50 target. However, with increasing aluminum content in the target, the bipolar pulsed direct current modes, especially with 250 kHz, are more suitable. If a single-phase coating is produced, the structure is more columnar than if multiple phases are formed. The latter is characterized by a more globular structure. The chemical composition of the coatings depends primarily on the sputter mode. Both the direct current mode and the 50 kHz bipolar pulsed direct current mode resulted in overstoichiometry of aluminum compared to the target concentrations, while the thin films produced with the 250 kHz bipolar pulsed direct current mode are overstoichiometric in titanium. Nitrogen, on the other hand, is always understoichiometric and its content depends strongly on the titanium content, so that the 50/50 target leads to the highest nitrogen concentrations. In all coatings from the 50/50 target, the main phase is a cubic solid solution. This was observed in only one other sample from the 33/67 target, while all other coatings formed either a pure hexagonal solid solution phase or a hexagonal main phase. The 33/67 and the 20/80 target led also to the formation of X-ray amorphous thin films at substrate temperatures below 200 °C. The highest hardness (38.21 GPa) could be achieved with the sample produced with the 50/50 target using the 50 kHz bipolar pulsed direct current mode at 600 °C. The highest hardness value of the 33/67 and 20/80 targets, which showed similar values in general, is 29.91 GPa. It has also been found that the hardness depends mainly on the crystal structure and not on the chemical composition. After annealing experiments, some coatings cracked multiple times or showed spalling. Depending on which phases and crystal structures were present at the beginning, the coatings developed very differently with regard to the formation of further phases or decomposition. Due to the resulting surface damage, the hardness has dropped very sharply, whereas it shows an increase when further phases have formed.

Die approbierte gedruckte Originalversion dieser Diplomarbeit ist an der TU Wien Bibliothek verfügbar
The approved original version of this thesis is available in print at TU Wien Bibliothek.
TU Bibliothek WIEN Your knowledge hub

Kurzfassung

Nicht-reaktives Magnetronsputtern von Titanaluminiumnitrid (Ti-Al-N) wurde trotz einiger Vorteile gegenüber der reaktiven Variante bisher nur wenig untersucht. So tritt beispielsweise der sogenannte "poisoning"-Effekt nicht auf, der den Sputter- und Abscheidungsprozess in manchen Fällen stark beeinträchtigen kann. Diese Arbeit geht daher der Frage nach, welche Auswirkungen das nicht-reaktive Sputtern auf die Eigenschaften von Ti-Al-N-Schichten hat. Zu diesem Zweck wurden drei verschiedene Targets mit den folgenden Zusammensetzungen ausgewählt: $Ti_{0.5}Al_{0.5}N$ (50/50), $Ti_{0.33}Al_{0.67}N$ (33/67) und $Ti_{0.2}Al_{0.8}N$ (20/80). Bei verschiedenen Substrattemperaturen (ohne zusätzliche Heizung, 200 °C, 300 °C, 450 °C und 600 °C) wurde die Abscheidung mit Gleichstrom oder bipolar gepulstem Gleichstrom (50 kHz und 250 kHz) durchgeführt.

Es hat sich gezeigt, dass der Gleichstrommodus für die Beschichtung mit dem 50/50-Target vorteilhaft ist. Mit zunehmendem Aluminium-Gehalt im Target sind jedoch die bipolar gepulsten Gleichstromverfahren, insbesondere mit 250 kHz, besser geeignet. Wird eine einphasige Dünnschicht erzeugt, bilden sich eher Säulen aus, als wenn mehrerer Phasen vorliegen. Letzteres führt zu einer feineren Struktur. Die chemische Zusammensetzung der Schichten hängt in erster Linie vom Sputtermodus ab. Sowohl der Gleichstrommodus als auch der bipolar gepulste 50-kHz-Gleichstrommodus ergaben eine Überstöchiometrie von Aluminium im Vergleich zu den Target-Konzentrationen, während die mit dem bipolar gepulsten 250-kHz-Gleichstrommodus hergestellten dünnen Schichten überstöchiometrisch in Titan sind. Stickstoff hingegen ist immer unterstöchiometrisch und der Gehalt hängt stark vom Titan-Gehalt ab, sodass das 50/50-Target beispielsweise zu den höchsten Stickstoff-Konzentrationen führt. In allen Dünnschichten vom 50/50-Target ist die Hauptphase ein kubischer Mischkristall. Dies wurde bei nur einer weiteren Probe vom 33/67-Target beobachtet. Alle anderen Schichten bildeten entweder eine hexagonale Mischkristallphase oder eine hexagonale Hauptphase aus. Das 33/67- und das 20/80-Target führten auch zur Bildung von röntgenamorphen Dünnschichten bei Substrattemperaturen von unter 200 °C. Die höchste Härte (38,21 GPa) konnte in der Probe erreicht werden, die mit dem 50/50-Target unter Verwendung des bipolar gepulsten 50-kHz-Gleichstrommodus bei 600 °C hergestellt wurde. Der höchste Härtewert der 33/67- und 20/80-Targets, die im Allgemeinen ähnliche Werte aufwiesen, beträgt 29,91 GPa. Weiters hat sich ergeben, dass die Härte hauptsächlich von der Kristallstruktur und nicht von der chemischen Zusammensetzung abhängt. Nach Glühexperimenten zeigten einige

Die approbierte gedruckte Originalversion dieser Diplomarbeit ist an der TU Wien Bibliothek verfügbar
The approved original version of this thesis is available in print at TU Wien Bibliothek.
TU Bibliothek Your knowledge hub WIEN

Schichten mehrfach Risse oder Abplatzungen. Je nachdem, welche Phasen und Kristallstrukturen zu Beginn vorhanden waren, entwickelten sich die Dünnschichte sehr unterschiedlich in Bezug auf die Bildung weiterer Phasen oder Entmischung. Durch die entstandenen Oberflächenschäden ist die Härte sehr stark gesunken, während sie durch die Bildung weiterer Phasen gestiegen ist.

TU WIEN Bibliothek Your knowledge hub
Die approbierte gedruckte Originalversion dieser Diplomarbeit ist an der TU Wien Bibliothek verfügbar
The approved original version of this thesis is available in print at TU Wien Bibliothek.

List of Figures

Figure 2.1. Hardness as a function of the annealing temperature of TiN and Ti-Al-N. [5]...... 4

Figure 2.2. Stable phase diagram of TiN-AlN calculated with the CALPHAD approach (adapted from [8])........ 5

Figure 2.3. Metastable "PVD" phase diagram of cubic TiN and cubic AlN calculated with the CALPHAD approach and compared to actual experimental data. [9]........ 5

Figure 3.1. Graphical representation of the signals for current and voltage of the bipolar pulsed direct current mode (50 kHz)........ 9

Figure 3.2. Scheme of the magnetron sputtering process in top-to-down configuration (top: target; down: substrate). Due to the circular plasma, the sputtering of target atoms leaves “racetracks” (adapted from [11])........ 10

Figure 3.3. Racetracks on a target after magnetron sputtering........ 10

Figure 3.4. The different targets used for the deposition: **a)** $Ti_{0.5}Al_{0.5}N$ (50/50), **b)** $Ti_{0.33}Al_{0.67}N$ (33/67) and **c)** $Ti_{0.2}Al_{0.8}N$ (20/80)........ 12

Figure 4.1. Schematic depiction of the three different growth modes. **a)** island growth (Volmer-Weber), **b)** layer-by-layer growth (Frank-van der Merwe), **c)** mixed growth (Stranski-Krastanov) – adapted from [14]........ 15

Figure 4.2. Illustration of the different interface types (adapted from [1])........ 16

Figure 4.3. SZM after Anders. It shows the influence of the generalized temperature T*, the normalized energy flux E* and the net film thickness t* on the growth morphology. [15] 17

Figure 5.1. Example of a load-displacement curve obtained during a nanoindentation test. The indicated parameters are necessary for the calculation of the hardness and elastic modulus of the specimen: P_{max} – maximum applied load, S – contact stiffness, h_f – final depth, h_c – contact depth, h_{max} – maximum depth. For further explanation see text........ 20

Figure 5.2. Example of a curve showing hardness against maximum penetration depth and the plateau from which the hardness values were obtained for the evaluation........ 22

Figure 5.3. Example of a curve showing elastic modulus against the maximum penetration depth. As one can see, the power law fit (red) is more suitable to describe the data than the linear fit (blue) or the arithmetic mean (green)........ 23

Figure 5.4. Graphical interpretation of Bragg's Law (adapted from [21])........ 25

Die approbierte gedruckte Originalversion dieser Diplomarbeit ist an der TU Wien Bibliothek verfügbar
The approved original version of this thesis is available in print at TU Wien Bibliothek.
TU WIEN Bibliothek Your knowledge hub

Figure 5.5. Diffractogram of a monocrystalline sapphire substrate, cut along the (1102) plane. The spectral lines of copper $K_{\alpha 1}$, $K_{\alpha 2}$ and K_{β} radiation and the peak produced by tungsten L radiation are indicated. 26
Figure 5.6. Diffractogram of a polycrystalline austenitic substrate. 26
Figure 5.7. Interaction volume of different signals created after primary electrons hit the sample. [28] SEs can only escape maximum depths of 10 nm due to their low energy. [27] . 29
Figure 5.8. Schematic illustration of **a)** spherical aberration (adapted from [29]) and **b)** astigmatism while changing the focus from overfocused to underfocused. 30
Figure 5.9. Topography contrast in a SE image (10 000 X). The edges are brighter than flat areas or averted surfaces. 31
Figure 5.10. Schematic setup of a TEM. [32] 32
Figure 5.11. Different imaging modes in STEM and the positions of their detectors after the beam passed the sample: bright field, low-angle annular dark field and high-angle annular dark field. [33] 34
Figure 5.12. Relation between N and Ti contents in EDX measurements. It is clearly shown that the N concentration increases with increasing Ti content and is thus falsified. The data point labels refer to the Ti/Al ratio of the targets. 36
Figure 5.13. EDX spectrum of Ti-Al-N, showing K_{α} peaks of Ti, Al, and N and also the Ti K_{β} peak. At approximately 3 keV, the Al sum peak is indicated. 37
Figure 6.1. Rate of deposition in *µm/h* of the three different targets varying with temperatures and sputter modes. 42
Figure 6.2. Cross section of the samples made from the 50/50 target with DC mode and **a)** no additional heating and **b)** at 600 °C substrate temperature. 43
Figure 6.3. Cross section of the samples made from the 50/50 target with BPDC-50 mode and **a)** no additional heating and **b)** at 600 °C substrate temperature. 44
Figure 6.4. Cross section of the samples made from the 50/50 target with BPDC-250 mode and **a)** no additional heating and **b)** at 600 °C substrate temperature. 44
Figure 6.5. Cross section of the samples made from the 33/67 target with DC mode and **a)** no additional heating and **b)** at 600 °C substrate temperature. 45
Figure 6.6. Cross section of the samples made from the 33/67 target with BPDC-50 mode and **a)** no additional heating and **b)** at 600 °C substrate temperature. 46
Figure 6.7. Cross section of the samples made from the 33/67 target with BPDC-250 mode and **a)** no additional heating and **b)** at 600 °C substrate temperature. 46

TU WIEN Bibliothek Your knowledge hub
Die approbierte gedruckte Originalversion dieser Diplomarbeit ist an der TU Wien Bibliothek verfügbar
The approved original version of this thesis is available in print at TU Wien Bibliothek.

Figure 6.8. Cross section of the samples made from the 20/80 target with DC mode and **a)** no additional heating and **b)** at 600 °C substrate temperature. 47

Figure 6.9. Cross section of the samples made from the 20/80 target with BPDC-50 mode and **a)** no additional heating and **b)** at 600 °C substrate temperature. 48

Figure 6.10. Cross section of the samples made from the 20/80 target with BPDC-250 mode and **a)** no additional heating and **b)** at 600 °C substrate temperature. 48

Figure 6.11. Cross section of the samples made from the 50/50 target at 600 °C with different sputter modes: **a)** DC, **b)** BPDC-50 and **c)** BPDC-250. 49

Figure 6.12. Cross section of the samples made from the 33/67 target at 600 °C with different sputter modes: **a)** DC, **b)** BPDC-50 and **c)** BPDC-250. 49

Figure 6.13. Cross section of the samples made from the 20/80 target at 600 °C with different sputter modes: **a)** DC, **b)** BPDC-50 and **c)** BPDC-250. 50

Figure 6.14. Angular distributions of sputtered atoms of the elements Al and Ti from pure Al and Ti targets respectively. The solid line represents the approximation of the experimental data (dots) and the dashed line is from a computer simulation (adapted from [37]). 51

Figure 6.15. Concentration of Ti and Al in at% for the three different targets with varying temperatures and sputter modes, measured with EDX. The horizontal lines indicate the concentration levels of Ti, Al and N of the respective targets. 53

Figure 6.16. Concentration of Ti, Al and N in at% for the three different targets with varying temperatures and sputter modes measured with EDX. The horizontal lines indicate the concentration levels of Ti, Al and N of the respective targets. 54

Figure 6.17. Concentration of Ti, Al and N in at% measured with EELS compared to the EDX results for specific samples. The horizontal lines indicate the concentration levels of Ti, Al and N of the respective targets. 55

Figure 6.18. Concentration of Ti, Al, N and O in at% measured with ERDA and compared to EDX values (sample: 50/50 target, DC mode, 300 °C). The dashed line marks the transition from the oxidized region to the homogeneous coating material. The indicated values in at% are the mean concentration values of each element and the horizontal lines indicate the concentration levels of Ti, Al and N of the target. 56

Figure 6.19. Concentration of Ti, Al, N and O in at% measured with ERDA and compared to EDX values (sample: 33/67 target, BPDC-50 mode, 200 °C). The dashed line marks the transition from the oxidized region to the homogeneous coating material. The indicated values in at% are the mean concentration values of each element and the horizontal lines indicate the concentration levels of Ti, Al and N of the target. 57

Die approbierte gedruckte Originalversion dieser Diplomarbeit ist an der TU Wien Bibliothek verfügbar
The approved original version of this thesis is available in print at TU Wien Bibliothek.
TU Bibliothek WIEN Your knowledge hub

Figure 6.20. Concentration of Ti, Al, N and O in at% measured with ERDA and compared to EDX values (sample: 20/80 target, DC mode, 450 °C). The dashed line marks the transition from the oxidized region to the homogeneous coating material. The indicated values in at% are the mean concentration values of each element and the horizontal lines indicate the concentration levels of Ti, Al and N of the target. 57
Figure 6.21. Diffractograms of samples made from the 50/50 target with the DC mode at varying substrate temperatures showing fcc-(Ti,Al)N and hexagonal (Al,Ti)N phases.......... 59
Figure 6.22. Diffractograms of samples made from the 50/50 target with the BPDC-50 mode at varying substrate temperatures showing fcc-(Ti,Al)N and hexagonal (Al,Ti)N phases...... 60
Figure 6.23. Diffractograms of samples made from the 50/50 target with the BPDC-250 mode at varying substrate temperatures showing fcc-(Ti,Al)N phases and perhaps initial precipitation of hexagonal (Al,Ti)N phases.. 62
Figure 6.24. Diffractograms of samples made from the 33/67 target with the DC mode at varying substrate temperatures showing fcc-(Ti,Al)N and hexagonal (Al,Ti)N phases.......... 64
Figure 6.25. Diffractograms of samples made from the 33/67 target with the BPDC-50 mode at varying substrate temperatures showing fcc-(Ti,Al)N and hexagonal (Al,Ti)N phases...... 65
Figure 6.26. Diffractograms of samples made from the 33/67 target with the BPDC-250 mode at varying substrate temperatures showing fcc-(Ti,Al)N and hexagonal (Al,Ti)N phases...... 66
Figure 6.27. Diffractograms of samples made from the 20/80 target with the DC mode at varying substrate temperatures showing hexagonal (Al,Ti)N phases.................................. 67
Figure 6.28. Diffractograms of samples made from the 20/80 target with the BPDC-50 mode at varying substrate temperatures showing hexagonal (Al,Ti)N phases. 68
Figure 6.29. Diffractograms of samples made from the 20/80 target with the BPDC-250 mode at varying substrate temperatures showing fcc-(Ti,Al)N and hexagonal (Al,Ti)N phases...... 69
Figure 6.30. HAADF image with SAED area indicated – substrate on the left and SEM image in the left corner (50/50 target)... 71
Figure 6.31. Integrated line graph with **a)** fcc-TiN and **b)** hexagonal AlN reference (50/50 target). 71
Figure 6.32. SAED ring pattern and assigned lattice planes of fcc-TiN (50/50 target).......... 71
Figure 6.33. SAED ring pattern and assigned lattice planes of hexagonal AlN (50/50 target). 71
Figure 6.34. HAADF image with SAED area indicated – substrate on the left and SEM image in the left corner (33/67 target)... 72

Die approbierte gedruckte Originalversion dieser Diplomarbeit ist an der TU Wien Bibliothek verfügbar
The approved original version of this thesis is available in print at TU Wien Bibliothek.
TU WIEN Bibliothek Your knowledge hub

Figure 6.35. Integrated line graph with **a)** fcc-TiN and **b)** hexagonal AlN reference (33/67 target). 72
Figure 6.36. SAED ring pattern and assigned lattice planes of fcc-TiN (33/67 target). 72
Figure 6.37. SAED ring pattern and assigned lattice planes of hexagonal AlN (33/67 target). 72
Figure 6.38. HAADF image with SAED area indicated – substrate on the left and SEM image in the left corner (20/80 target). 73
Figure 6.39. Integrated line graph with **a)** fcc-TiN and **b)** hexagonal AlN reference (20/80 target). 73
Figure 6.40. SAED ring pattern and assigned lattice planes of fcc-TiN (20/80 target). 73
Figure 6.41. SAED ring pattern and assigned lattice planes of hexagonal AlN (20/80 target). 73
Figure 6.42. Hardness and Elastic Modulus in GPa for the three different targets with varying temperatures and sputter modes before annealing. 78
Figure 6.43. Surface of the coating **a)** before and **b)** after annealing (50/50 target, DC mode, 200 °C). 80
Figure 6.44. Surface of the coating **a)** before and **b)** after annealing (50/50 target, BPDC-50 mode, 600 °C). 80
Figure 6.45. Surface of the coating **a)** before and **b)** after annealing (33/67 target, DC mode, 200 °C). 80
Figure 6.46. Surface of the coating **a)** before and **b)** after annealing (33/67 target, BPDC-50 mode, no heating). 81
Figure 6.47. Surface of the coating after annealing (33/67 target, BPDC-50 mode, no heating); image taken at a five hundred magnification. 81
Figure 6.48. Surface of the coating **a)** before and **b)** after annealing (20/80 target, BPDC-50 mode, 300 °C). 81
Figure 6.49. Evolution of the crystal structure during annealing from 600 °C to 1125 °C and diffractograms before and after annealing (sample: 50/50 target, DC mode, 200 °C). The cubic Ti-Al-N solid solution forms Ti-rich and Al-rich regions. 84
Figure 6.50. Evolution of the crystal structure during annealing from 600 °C to 1125 °C and diffractograms before and after annealing (sample: 50/50 target, BPDC-50 mode, 600 °C). Hexagonal (Al,Ti)N precipitates from the cubic Ti-Al-N matrix, making it richer in Ti. 85

TU Bibliothek WIEN Your knowledge hub
Die approbierte gedruckte Originalversion dieser Diplomarbeit ist an der TU Wien Bibliothek verfügbar
The approved original version of this thesis is available in print at TU Wien Bibliothek.

Figure 6.51. Evolution of the crystal structure during annealing from 600 °C to 1050 °C and diffractograms before and after annealing (sample: 33/67 target, DC mode, 200 °C). The hexagonal Ti-Al-N solid solution decomposes into hexagonal AlN and fcc-TiN.................. 86
Figure 6.52. Evolution of the crystal structure during annealing from 500 °C to 1190 °C and diffractograms before and after annealing (sample: 33/67 target, BPDC-50 mode, no heating). Hexagonal AlN and fcc-TiN form from the X-ray amorphous matrix and SiO_2 (here in rutile structure) occurs between approximately 700 °C and 1150 °C.. 87
Figure 6.53. Evolution of the crystal structure during annealing from 600 °C to 1125 °C and diffractograms before and after annealing (sample: 20/80 target, BPDC-50 mode, 300 °C). The fcc-(Ti,Al)N phase precipitates from the hexagonal Ti-Al-N matrix, making it richer in Al. 88
Figure 6.54. Hardness and Elastic Modulus in GPa for chosen samples before and after annealing. 90

Figure A. 1. 50/50 target - DC mode - 200 °C. 105
Figure A. 2. 50/50 target - DC mode - 300 °C. 105
Figure A. 3. 50/50 target - DC mode - 450 °C. 105
Figure A. 4. 50/50 target - BPDC-50 mode - 200 °C.. 105
Figure A. 5. 50/50 target - BPDC-50 mode - 300 °C.. 105
Figure A. 6. 50/50 target - BPDC-50 mode - 450 °C.. 105
Figure A. 7. 50/50 target - BPDC-250 mode - 200 °C.. 105
Figure A. 8. 50/50 target - BPDC-250 mode - 300 °C.. 105
Figure A. 9. 50/50 target - BPDC-250 mode - 450 °C.. 105
Figure A. 10. 33/67 target - DC mode - 200 °C. 105
Figure A. 11. 33/67 target - DC mode - 300 °C. 105
Figure A. 12. 33/67 target - DC mode - 450 °C. 105
Figure A. 13. 33/67 target - BPDC-50 mode - 200 °C.. 106
Figure A. 14. 33/67 target - BPDC-50 mode - 300 °C.. 106
Figure A. 15. 33/67 target - BPDC-50 mode - 450 °C.. 106
Figure A. 16. 33/67 target - BPDC-250 mode - 200 °C.. 106
Figure A. 17. 33/67 target - BPDC-250 mode - 300 °C.. 106
Figure A. 18. 33/67 target - BPDC-250 mode - 450 °C.. 106
Figure A. 19. 20/80 target - DC mode - 200 °C. 106
Figure A. 20. 20/80 target - DC mode - 300 °C. 106
Figure A. 21. 20/80 target - DC mode - 450 °C. 106

Die approbierte gedruckte Originalversion dieser Diplomarbeit ist an der TU Wien Bibliothek verfügbar
The approved original version of this thesis is available in print at TU Wien Bibliothek.
TU WIEN Bibliothek Your knowledge hub

Figure A. 22. 20/80 target - BPDC-50 mode - 200 °C.. 106
Figure A. 23. 20/80 target - BPDC-50 mode - 300 °C.. 106
Figure A. 24. 20/80 target - BPDC-50 mode - 450 °C.. 106
Figure A. 25. 20/80 target - BPDC-250 mode - 200 °C.. 107
Figure A. 26. 20/80 target - BPDC-250 mode - 300 °C.. 107
Figure A. 27. 20/80 target - BPDC-250 mode - 450 °C.. 107

Die approbierte gedruckte Originalversion dieser Diplomarbeit ist an der TU Wien Bibliothek verfügbar
The approved original version of this thesis is available in print at TU Wien Bibliothek.
TU Bibliothek Your knowledge hub
TU WIEN

List of Tables

Table 3.1. Major advantages and disadvantages of different plasma generating methods [1] .. 8

Table 3.2. Process parameters for etching 11

Table 3.3. Process parameters for deposition 13

Table 5.1. Poisson's ratios of indenter and the targets 24

Table 5.2. Wavelength of characteristic X-rays of copper (Cu) and tungsten (W) and corresponding *2θ* angles of α-Al_2O_3 for d = 0.174 nm [20], [22] 25

Table 5.3. Parameters for EDX analysis 38

Table A. 1. Process parameters of the 50/50 Target 98

Table A. 2. Process parameters of the 33/67 target 99

Table A. 3. Process parameters of the 20/80 target 100

Table A. 4. Values of thickness and deposition rate of all samples 101

Table A. 5. Values of the EDX measurements 102

Table A. 6. Values of the EELS and ERDA measurements 103

Table A. 7. Values of the hardness and the elastic modulus after annealing 103

Table A. 8. Values of the hardness and the elastic modulus before annealing 104

Die approbierte gedruckte Originalversion dieser Diplomarbeit ist an der TU Wien Bibliothek verfügbar
The approved original version of this thesis is available in print at TU Wien Bibliothek.
TU WIEN Bibliothek Your knowledge hub

List of Abbreviations and Symbols

(Al,Ti)N *Hexagonal Al-rich Ti-Al-N solid solution phase*

(S)TEM *(Scanning) Transmission Electron Microscopy/Microscope*

(Ti,Al)N *Cubic Ti-rich Ti-Al-N solid solution phase*

20/80 *Target; titanium aluminum nitride: 20 at% Ti, 80 at% Al*

33/67 *Target; titanium aluminum nitride: 33 at% Ti, 67 at% Al*

50/50 *Target; titanium aluminum nitride: 50 at% Ti, 50 at% Al*

Å *Ångström*

ADF *Annular dark field*

Al *Aluminum*

AlN *Aluminum nitride*

Ar^+ *Argon ion*

at% *Atomic percentage*

BF *Bright field*

BPDC *Bipolar pulsed direct current*

BPDC-250 *Bipolar pulsed direct current with 250 kHz*

BPDC-50 *Bipolar pulsed direct current with 50 kHz*

BSE *Backscattered electron*

CBED *Convergent Beam Electron Diffraction*

DC *Direct current*

DF *Dark field*

EDX *Energy Dispersive X-Ray Spectroscopy*

EELS *Electron Energy Loss Spectroscopy*

ERDA *Elastic Recoil Detection Analysis*

eV *Electron volt*

fcc *Face-centered cubic*

FEG-SEM *Field Emission Gun Scanning Electron Microscope*

FIB *Focused Ion Beam Technique*

GPa *Gigapascal (unit)*

HAADF *High-angle annular dark field*

hcp *Hexagonal close-packed*

HIPIMS *High Power Impulse Magnetron Sputtering*

Die approbierte gedruckte Originalversion dieser Diplomarbeit ist an der TU Wien Bibliothek verfügbar
The approved original version of this thesis is available in print at TU Wien Bibliothek.
TU Bibliothek Your knowledge hub WIEN

LAADF *Low-angle annular dark field*

N_2 *Nitrogen gas*

NaCl *Sodium chloride*

O *Oxygen*

PVD *Physical Vapor Deposition*

SAED *Selected Area Electron Diffraction*

sccm *Standard cubic centimeters per minute*

SE *Secondary electron*

SEM *Scanning Electron Microscopy/Microscope*

STEM *Scanning Transmission Electron Microscopy/Microscope*

SZM *Structure Zone Model*

TEM *Transmission Electron Microscopy/Microscope*

$Ti_{1-x}Al_xN$ *Titanium aluminum nitride with variable amounts of Ti and Al*

Ti-Al-N *Titanium aluminum nitride*

TiN *Titanium nitride*

USTEM *University Service Center for Transmission Electron Microscopy, TU Wien, Austria*

XRD *X-Ray Diffraction*

Z *Atomic number*

ZnS *Tin sulfide*

Die approbierte gedruckte Originalversion dieser Diplomarbeit ist an der TU Wien Bibliothek verfügbar
The approved original version of this thesis is available in print at TU Wien Bibliothek.
TU WIEN Bibliothek Your knowledge hub

Die approbierte gedruckte Originalversion dieser Diplomarbeit ist an der TU Wien Bibliothek verfügbar
The approved original version of this thesis is available in print at TU Wien Bibliothek.
TU WIEN Bibliothek Your knowledge hub

1 Introduction

Since the earliest development of basic tools, humans were interested in modifying the surfaces according to their wishes. Still, it was a long way from simple paint to high performance hard coatings which get more and more important nowadays. They have a great impact on prolonging the lifetime of a tool by reducing friction and wear or increase the corrosion resistance or thermal stability. One important coating method is sputter deposition: Particles of a plasma transfer momentum to particles of the source material by bombardment. These source particles are ejected and transferred in the gaseous state to a substrate where they are deposited. Besides the different methods to generate the plasma, the sputter deposition process can be conducted in two ways: Either reactive or non-reactive. In contrast to the latter that uses a material source which already contains all components necessary for the coating, the former needs a constant inlet of a reactive gas which forms, in combination with the source material, the wanted coating compound. A major downside of the reactive method is the "poisoning" effect of the source material, where the source is covered with the resulting coating material reducing the efficiency of the process. Some widespread applications of sputter deposition are, for example, magnetic films, hard coatings, decorative coatings or reflective coatings on CDs. [1]

In the early 1980s, scientists and the industry showed increasing interest in titanium nitride (TiN) coatings and even today their application is of great economic importance. Since it is electrically conductive, it is well suitable for sputter deposition and hard coatings are easily produced. [2] To increase the oxidation resistance, aluminum (Al) was introduced into the crystal lattice, which additionally led to higher hardness even at high temperatures. [3] These titanium aluminum nitride (Ti-Al-N) coatings produced with reactive sputter deposition are well studied, but little in depth research has been done on the non-reactive way. As mentioned above, poisoning of the source is a major problem in reactive sputtering, therefore, the non-reactive method can be a great improvement of the whole production chain. In order to determine the limits of the process regarding the amount of aluminum nitride (AlN) which can be incorporated into the TiN crystal lattice, different source material compositions were used. The way in which the plasma is generated has also a great influence on the thin film (for example, concerning deposition rate, crystal structure or texture), hence different procedures were examined.

Die approbierte gedruckte Originalversion dieser Diplomarbeit ist an der TU Wien Bibliothek verfügbar
The approved original version of this thesis is available in print at TU Wien Bibliothek.
TU WIEN Bibliothek Your knowledge hub

To determine the properties of the produced thin films, several test methods were applied: Hardness measurements were performed with the nanoindentation process; the microstructure, the film thickness and the chemical composition were investigated with a Scanning Electron Microscope (also with Energy Dispersive X-Ray Spectroscopy); with a Transmission Electron Microscope and X-Ray Diffraction the crystal structure was examined, and further investigations regarding the chemical composition were conducted with Electron Energy Loss Spectroscopy and Elastic Recoil Detection Analysis. In addition, in situ X-Ray Diffraction measurements were performed while the temperature was constantly increased to determine the thermal stability of the thin films.

This thesis first explains the properties of Ti-Al-N coatings, then the fundamentals of the sputter deposition process and subsequently the major aspects which need to be considered if a thin film is produced with a physical vapor deposition process. A brief overview about the applied test methods follows, where also the used parameters are mentioned in each chapter. The results regarding the deposition rate, the microstructure, the chemical composition, crystallographic and mechanical properties, and the thermal stability are presented in individual chapters.

Die approbierte gedruckte Originalversion dieser Diplomarbeit ist an der TU Wien Bibliothek verfügbar
The approved original version of this thesis is available in print at TU Wien Bibliothek.
TU WIEN Bibliothek Your knowledge hub

2 Titanium Aluminum Nitride

Titanium nitride (TiN) is a ceramic hard material, more precisely an intermetallic Hägg phase, and shows a cubic crystal structure of the sodium chloride (NaCl) type, where the Ti atoms form a face-centered cubic (fcc) lattice, and the nitrogen (N) atoms fill in the octahedral sites. The lattice parameter is slightly different for thin films compared to the bulk material (4.24 Å) because of intrinsic stresses. These can be caused by different thermal expansion coefficients of coating and substrate, high defect concentrations (for example impurities) or small grain sizes. The hardness depends on the microstructure, especially on defects like voids at grain boundaries, whereby values around 20 to 30 GPa are common for stoichiometric films. Due to this high hardness and a good toughness, TiN coatings were already used on high-speed tools at an early stage and are still applied nowadays to increase the wear or corrosion resistance. [2]

Because of the good electrical conductivity in its bulk form, TiN is very suitable for physical vapor deposition processes (see Chapter 3). In contrast, the conductivity of the thin films depends highly on the growth conditions. [2] Nonetheless, TiN coatings are used as electrically conductive diffusion barriers in applications such as semiconductor devices. [1] Another favorable property is the golden color of TiN in the range of visible light. Therefore, it is also used for decorative applications. [2]

One of the major drawbacks of TiN coatings is the decreasing hardness with increasing temperatures (see Figure 2.1) and the low oxidation resistance upon heating above 550 °C. [3] As temperatures up to 1000 °C can be reached during machining [4], new compounds or ternary systems like titanium-aluminum-nitrogen (Ti-Al-N) were researched in the 1980s. Aluminum (Al) was chosen as it shows a good oxidation resistance at elevated temperatures due to the formation of aluminum oxide. Early tests showed that Ti was substituted by Al, resulting in a decreasing lattice parameter with increasing Al content as Al atoms are smaller than Ti atoms. [3] With Ti-Al-N systems it is possible to produce hard coatings (around 28 to 30 GPa) with lower compressive stresses compared to pure TiN coatings (compressive stresses: TiN – up to 10 GPa, Ti-Al-N – around 5 GPa). This leads to an improved adhesion to the substrate. [4] Moreover, the hardness increases with rising temperatures (see Figure 2.1) due to age hardening by spinodal decomposition. [5] Further, Ti-Al-N coatings form an aluminum oxide layer on top which reduces diffusion towards or away from the thin film and results in

TU Bibliothek Your knowledge hub WIEN
Die approbierte gedruckte Originalversion dieser Diplomarbeit ist an der TU Wien Bibliothek verfügbar
The approved original version of this thesis is available in print at TU Wien Bibliothek.

oxidation processes not starting before 700 °C. [4] Not only the oxidation resistance can be improved, but also the cutting performance as the flank wear is reduced by a third. [3]

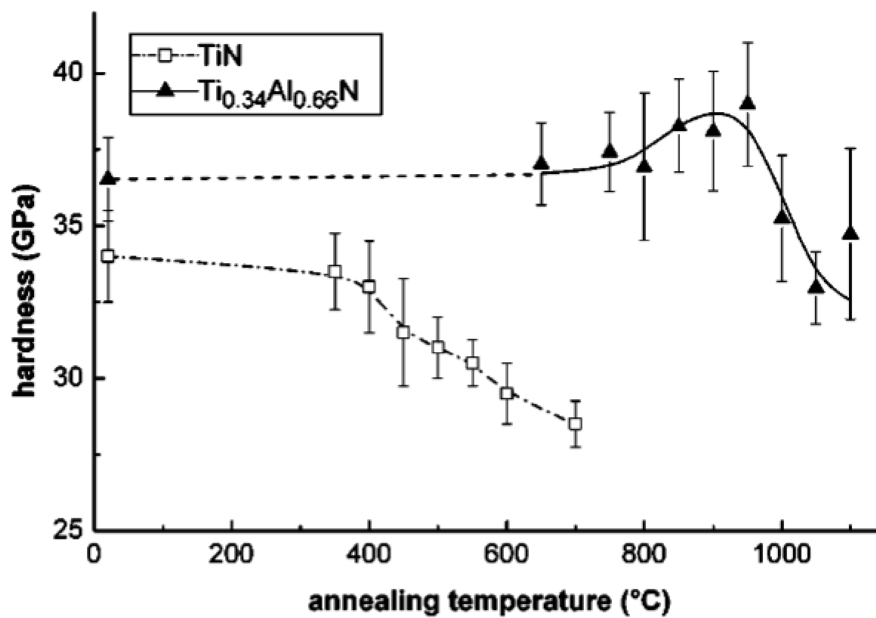

Figure 2.1. Hardness as a function of the annealing temperature of TiN and Ti-Al-N. [5]

To reach the high hardness, a cubic NaCl structure must also be formed in the Ti-Al-N system. Only 65 to 75 at% of Al can be incorporated into the cubic crystal lattice which is the limit of solid solubility of Al in the cubic structure for the metastable state. Above this point a mixture of the NaCl and the hexagonal tin sulfide (ZnS, wurtzite) structure or even pure wurtzite coatings are formed. The wurtzite structure is the preferred crystal structure of aluminum nitride (AlN), which reduces the hardness and the wear resistance of the coating. [6]

As mentioned above, Ti-Al-N coatings are not only capable of keeping a high hardness upon heating, but even show a hardness increase. This is possible due to the age hardening effect by spinodal decomposition. [5] The latter occurs if the gradient of the chemical potential is against the concentration gradient whereby a single-phase solid solution can decompose in situ into at least two phases which are then richer in one component. It can only happen if the solid solution is in an unstable state regarding the Gibbs free energy and any fluctuation in composition leads to a decrease of this energy. [7] This is fulfilled for the Ti-Al-N as TiN and AlN are not miscible at room temperatures (see Figure 2.2), but high energies and high cooling rates in the sputter deposition process enable the formation of a metastable solid solution phase (see Figure 2.3). The spinodal decomposition starts with the formation of coherent cubic domains within the cubic $Ti_{1-x}Al_xN$ matrix, which are either TiN- or AlN-rich. This hinders the movement of dislocations through the material and therefore increases the hardness. If the energy input is

Die approbierte gedruckte Originalversion dieser Diplomarbeit ist an der TU Wien Bibliothek verfügbar
The approved original version of this thesis is available in print at TU Wien Bibliothek.
TU WIEN Bibliothek Your knowledge hub

high enough, for example due to high temperatures, the domains develop into new phases (fcc-TiN and fcc-AlN) within the matrix and finally to stable fcc-TiN and hexagonal close-packed (hcp) AlN without any matrix left which leads to a decrease in hardness. [5]

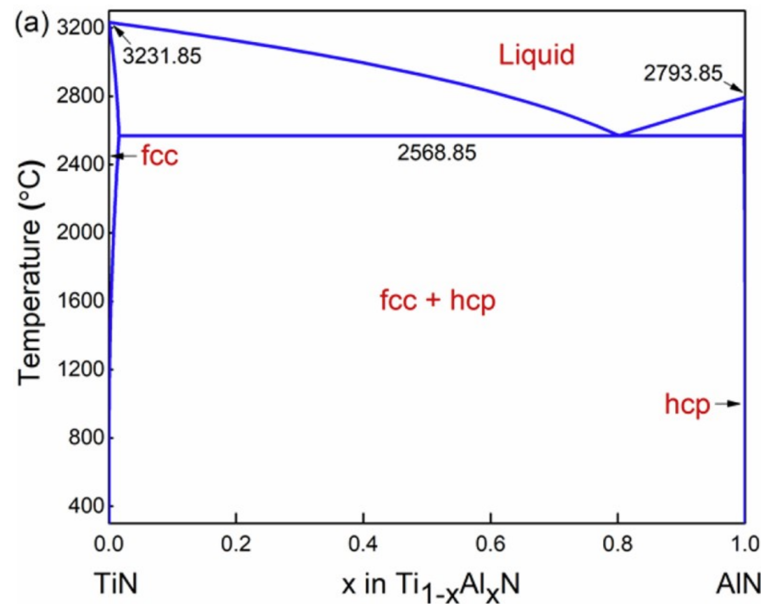

Figure 2.2. Stable phase diagram of TiN-AlN calculated with the CALPHAD approach (adapted from [8]).

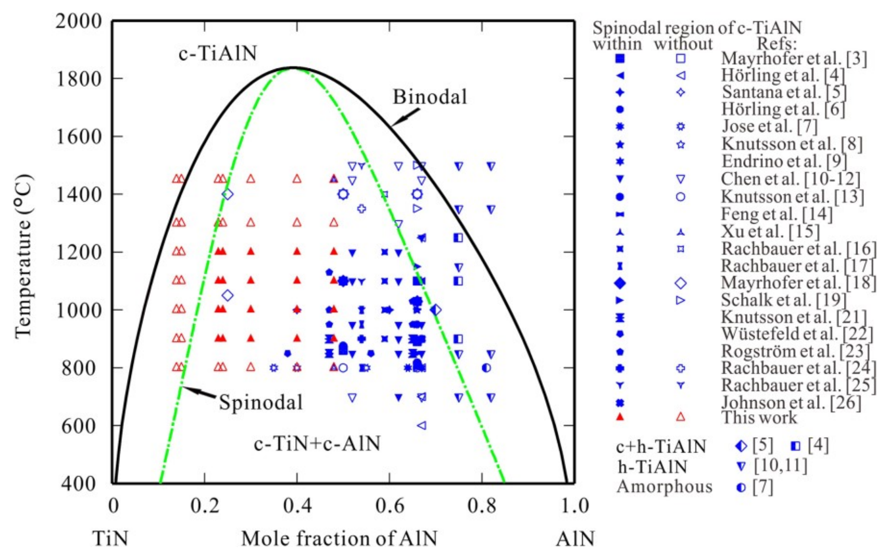

Figure 2.3. Metastable "PVD" phase diagram of cubic TiN and cubic AlN calculated with the CALPHAD approach and compared to actual experimental data. [9]

Die approbierte gedruckte Originalversion dieser Diplomarbeit ist an der TU Wien Bibliothek verfügbar
The approved original version of this thesis is available in print at TU Wien Bibliothek.
TU WIEN Bibliothek Your knowledge hub

3 Physical Vapor Deposition

The term "Surface Engineering" describes each form of changing the properties of a surface, whether it is a deposition process (covering the substrate with an additional material) or a modification process (mechanical, thermal, or chemical conversion of the outer region of a material). Often, a combination of both processes is applied. [1]

One important method is Physical Vapor Deposition (PVD), where a solid or liquid source material ("target") gets physically vaporized, then transported in the vaporized state to a substrate where the vapor condenses and forms coatings (thin films of a few micrometers). The major types of PVD are sputtering, evaporation, arc vaporization and ion plating. The applications reach from optical and decorative coatings to barrier films, or coatings for better wear and erosion resistance or better electrical conductivity. Compared to their bulk form, thin films can show unique and completely different properties, enabling applications which could not be realized with the bulk form. [1]

3.1 Sputter Deposition

Sputtering became important in the last few decades as the processes behind its physics were understood and proven: Due to a momentum transfer from an impacting high-energy particle, atoms are ejected from the target. Usually, ions (for example argon ions, Ar^+) are used, which are created in a cold plasma and then accelerated by an electrical field towards the target (cathode; the substrates are connected to the anode). Sputtering is not energy efficient as only a hundredth of the incident energy is transferred to the sputtered atom and more than 95 % of the energy is converted into heat. Therefore, the target must be cooled so that it is not damaged. Still, the process is easily reproduceable and nearly every material can be sputtered. It can be either performed *reactively* where the source material reacts with an ambient gas to form compounds or *non-reactively* where the target already has the wanted composition. A mixture of both (a quasi-reactive process) uses a target with the right composition and, in addition, a gas inlet to compensate the loss of volatile species. For the entire process, it is beneficial to use metallic targets as they are more easily produced than ceramic ones and ease the sputter deposition. This can be realized with reactive sputtering, but it has its downsides, for example reaction gas adsorption on the target. The adsorbed gas atoms or ions can react with the target

Die approbierte gedruckte Originalversion dieser Diplomarbeit ist an der TU Wien Bibliothek verfügbar
The approved original version of this thesis is available in print at TU Wien Bibliothek.
TU WIEN Bibliothek Your knowledge hub

atoms to form compounds which cover the target. This problem arises especially if the sputter rate is low and can lead to the formation of insulating materials which changes the conditions for plasma generation. Next to this so-called "poisoning" of the target, also non-reactive species of the reaction gas can be adsorbed onto the substrate (for example nitrogen gas, N_2), which impedes or alters the growth process. [1]

To reach a sufficiently high deposition rate, the sputter yield (the mean number of sputtered atoms per impacting ion) must be also high. It depends on the mass and energy of the ion, the angle-of-incident (best sputter yield around 60-70°), and the threshold energy. The latter is the minimum energy that is needed to eject an atom from the target and is related to the binding energy of this atom within the solid. The energy of an impacting ion can be controlled by the pressure within the chamber and the mean free path (see Chapter 3.1.1). [1]

In order to improve the properties of the produced film, a negative bias can be applied to the anode (substrate): Ions are accelerated towards the anode (≥ 100 eV) which leads to high ion bombardment of the formed coating. This can increase the film's density, but also leads to compressive stresses, lattice defects and discharge gas incorporation. To overcome these disadvantages, it is beneficial to use low energy ions and to obtain a high ratio between argon ions and target atoms in the plasma, which still transfers sufficient energy to the thin film, but reduces stresses. [10]

3.1.1 Plasma Generation

To generate a cold (non-thermal) plasma, electrical current must be applied, and electrons must ionize atoms of the process gas by inelastic electron-atom collisions. This is possible after a certain gas pressure is reached and results in a glow discharge. The electrons need to gain a certain energy level so that the collisions are effective which means that the mean free path must be long enough. This is the average distance a particle in the gaseous state can travel until it collides with another particle and is mainly determined by the partial pressure of the process gas. If the pressure is low, the mean free path is long, and particles can freely accelerate and gain a high energy level. However, there is a minimal pressure limit, because if it gets too low either the plasma is extinguished or there are not enough ions generated. On the other hand, too high pressures result in excess collisions of sputtered atoms with the process gas, which also decreases the deposition rate. For the same reasons, the deposition chamber should be under an ultra-high vacuum to minimize contamination and to optimize the sputter deposition

TU Bibliothek, WIEN Your knowledge hub
Die approbierte gedruckte Originalversion dieser Diplomarbeit ist an der TU Wien Bibliothek verfügbar
The approved original version of this thesis is available in print at TU Wien Bibliothek.

process. [1] The plasma can be only sustained if a continuous supply of energy is given, and new free electrons are generated to ionize further atoms. The latter is important because ions and electrons are lost to different surfaces in the deposition chamber. However, during the ion bombardment, secondary electrons can leave the target, which can generate new ions. Since electrons are the lighter species and more of them are lost to surfaces, the plasma is positively charged compared to the surfaces – including the cathode. Therefore, ions can be accelerated towards the target and can transfer more energy to the target atoms. [1]

Usually, sputter deposition is performed with a weakly ionized plasma in which more neutrals than ions are present. The neutral atoms occur either in their ground state or in an excited state, where outer-shell electrons are raised to higher energy levels. During de-excitation, the excess energy is emitted as a photon which results in a glow. Other plasma species are radicals or fragments of molecules which are created by electrons. [1]

There are diverse ways to produce a plasma: direct current (DC) discharge, pulsed power discharge, radio frequency discharge, arc discharge or laser-induced discharge. The major advantages and disadvantages of these methods are listed in Table 3.1. [1]

Table 3.1. Major advantages and disadvantages of different plasma generating methods [1]

Sputter Deposition Method	Advantages	Disadvantages
Direct Current	High power	Electrically conductive material needed
Pulsed Direct Current Pulsed Alternating Current	Neutralization of positive charge build-up on cathode during off-time → insulators suitable	Low power
HIPIMS (High Power Impulse Magnetron Sputtering)	High power; insulators suitable; high ionization of metals	Low sputter rate due to short on-time
Radio Frequency	Neutralization of positive charge build-up	Difficult to perform
Arc	Multiple-charged high energy ions	
Laser-Induced	High ionization rate	

Die approbierte gedruckte Originalversion dieser Diplomarbeit ist an der TU Wien Bibliothek verfügbar
The approved original version of this thesis is available in print at TU Wien Bibliothek.
TU Bibliothek WIEN Your knowledge hub

For the depositions of this thesis, the direct current (DC) and the bipolar pulsed direct current (BPDC) mode were applied (for the latter see Figure 3.1). The BPDC mode is a special form of pulsed modes where two separate circuits either produce positive or negative pulses, which results in a "pseudo-alternating" signal as a direct current is applied to both circuits. This mode can be also used for poorly conductive targets because the positive charge build-up of argon ions on the cathode is neutralized with electrons during the positive bias, whereas the target is sputtered during the negative bias. [1]

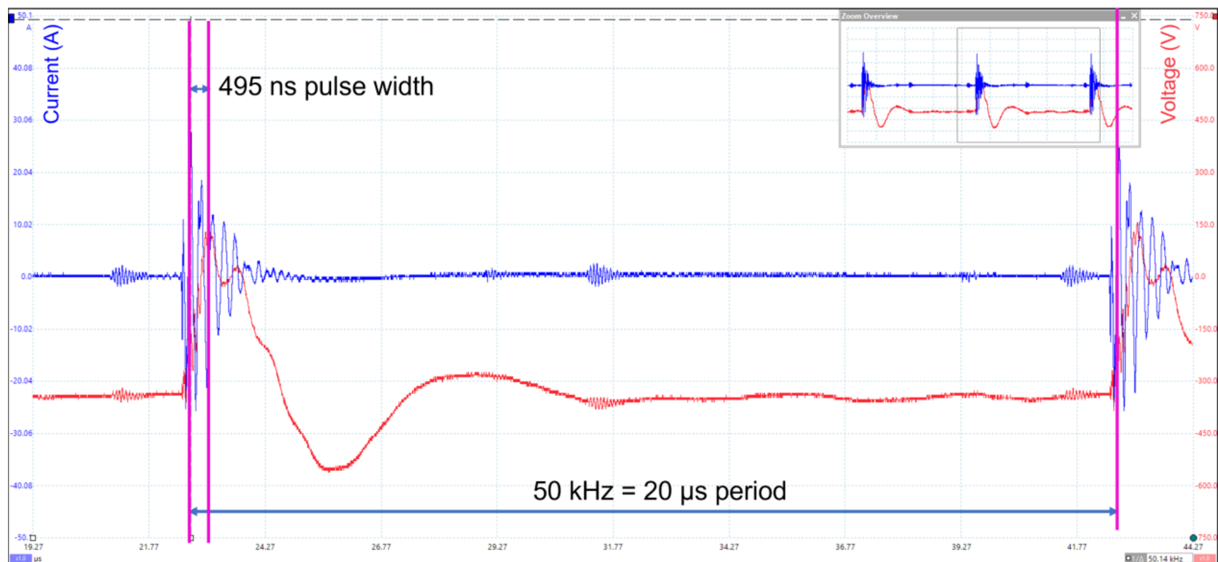

Figure 3.1. Graphical representation of the signals for current and voltage of the bipolar pulsed direct current mode (50 kHz).

3.1.2 Magnetron Sputtering

Magnetron sputtering uses magnets which are placed behind the target so that electrons are forced onto a closed path (see Figure 3.2). The magnetic field lines trap the electrons near the cathode surface which increases the ionization efficiency. Subsequently, the sputtering efficiency increases, and the plasma can be generated and sustained with lower pressure whereby sputtered atoms experience less collisions. Magnetron sputtering can be performed in two ways: Either no electrons are allowed to escape the near-target region (balanced magnetron), or some electrons can escape and form a plasma further away from the cathode (unbalanced magnetron). This is beneficial for ion plating and reactive sputtering. [1]

Die approbierte gedruckte Originalversion dieser Diplomarbeit ist an der TU Wien Bibliothek verfügbar
The approved original version of this thesis is available in print at TU Wien Bibliothek.
TU WIEN Bibliothek Your knowledge hub

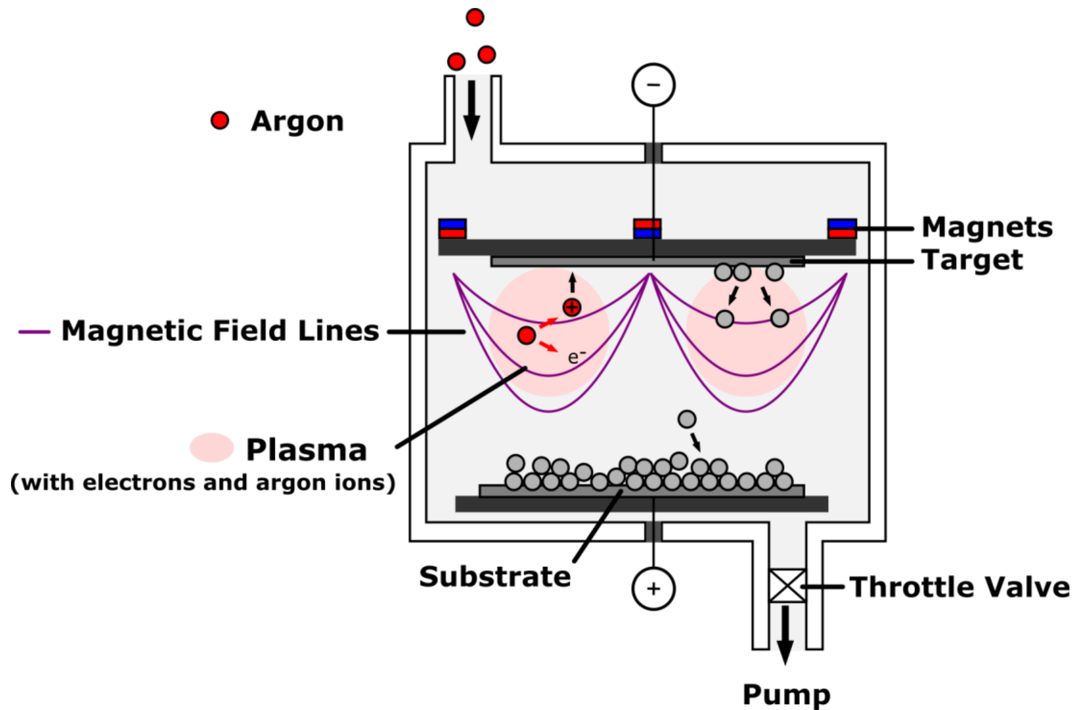

Figure 3.2. Scheme of the magnetron sputtering process in top-to-down configuration (top: target; down: substrate). Due to the circular plasma, the sputtering of target atoms leaves "racetracks" (adapted from [11]).

Due to the circular arrangement of the magnets, the plasma shows a toroidal shape, and the target is mainly sputtered in this region, leaving so-called "racetracks" (see Figure 3.3).

Figure 3.3. Racetrack on a target after magnetron sputtering.

3.2 Experimental Implementation

The sputter deposition was performed with a modified *Leybold Heraeus Z400 Laboratory* PVD system in a down-to-top configuration, where the target sits on the bottom of the chamber and the substrates are placed above it. This is advantageous because material which flakes off the

Die approbierte gedruckte Originalversion dieser Diplomarbeit ist an der TU Wien Bibliothek verfügbar
The approved original version of this thesis is available in print at TU Wien Bibliothek.
TU Bibliothek Your knowledge hub WIEN

chamber wall or other surfaces does not drop onto the substrates and therefore does not interrupt the deposition process. However, if the substrates themselves break during the deposition, parts of them can fall onto the target, which can either change the thin film composition or the system is short-circuited if the cathode is electrically connected to the clamp ring.

For this thesis, polished platelets of single-crystal sapphire (cut along the $(1\bar{1}02)$ plane), single-crystal silicon, and austenitic Cr-Ni steel were used as substrates. Because the properties of the substrate surface, like morphology and chemistry, can have a great influence on the sputtering process and the thin film properties, it is important to obtain a surface with defined and favorable conditions. [1] Therefore, the substrates were cleaned in an ultrasonic bath in acetone and isopropanol, and then by plasma etching in the sputter chamber. Plasma etching is a three-step process starting with contamination removal. It is followed by surface activation and plasma etching which works like the sputtering process, whereby argon gas was used as process gas. [12] Etching was performed when the chamber was already vacuumized (pressure of 10^{-6} mbar) and, if necessary, heated with a light radiation heater which transfers the heat via infrared radiation. As the temperature sensor in this machine sits at the heat source and not on the substrate, there is a heat discrepancy between the set/displayed temperature and the one of the substrates. It can be calculated with a reference function (see Equation (1)) how much hotter the heat source must be so that the substrates reach the right temperature. Further process parameters during etching can be seen in Table 3.2.

$$T_{substrate} = \frac{T_{set} + 27.407}{1.2984} \,°C \qquad (1)$$

Table 3.2. Process parameters for etching

Parameter	Value
Mode	Bipolar pulsed direct current: 150 kHz, 2656 ns on-time; voltage-controlled
Bias Voltage (V)	-150
Power (W)	21
Gas Flow (sccm)	120 / 60
Total Pressure (mbar)	0.012 / 0.006
Time period (min)	15

Die approbierte gedruckte Originalversion dieser Diplomarbeit ist an der TU Wien Bibliothek verfügbar
The approved original version of this thesis is available in print at TU Wien Bibliothek.
TU WIEN Bibliothek Your knowledge hub

During the last five minutes of the etching process, a second plasma was ignited at the target (substrates and target were separated with a shutter) to clean the target surface from oxides and adsorbed gases, and to enable a soft crossover to the deposition process. This can be especially useful for the generation of the plasma if the target has a low electrical conductivity. For this thesis, the parameters were chosen in a way that a current of 0.3 to 0.5 A was reached.

The method used for the deposition was non-reactive magnetron sputtering with argon gas as process gas and targets with a diameter of three inches, which were powder metallurgically produced by plasma sintering (see Figure 3.4).

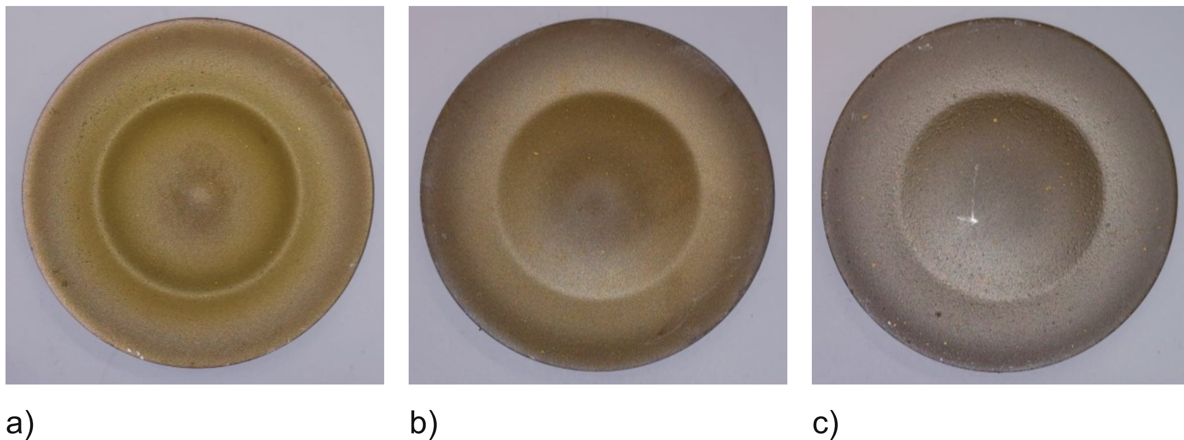

Figure 3.4. The different targets used for the deposition: **a)** $Ti_{0.5}Al_{0.5}N$ (50/50), **b)** $Ti_{0.33}Al_{0.67}N$ (33/67) and **c)** $Ti_{0.2}Al_{0.8}N$ (20/80).

Because one aim of this thesis was to determine the limits of the solubility of aluminum (Al) in titanium aluminum nitride (Ti-Al-N) during non-reactive sputtering, three targets with different compositions were utilized: $Ti_{0.5}Al_{0.5}N$ (50/50), $Ti_{0.33}Al_{0.67}N$ (33/67) and $Ti_{0.2}Al_{0.8}N$ (20/80). For all these targets a temperature and sputter mode study was conducted, whereby for each mode the substrates were either not additionally heated or heated to 245 °C, 375 °C, 550 °C or 750 °C (set temperature; the corresponding substrate temperatures calculated with Equation (1) are: 200 °C, 300 °C, 450 °C and 600 °C). The sputter modes were: direct current (DC) – current-controlled; bipolar pulsed DC with 50 kHz and 496 ns on-time (BPDC-50) – power-controlled; bipolar pulsed DC with 250 kHz and 1616 ns (BPDC-250) – power-controlled). The distance between target and substrates was 39 mm, the argon gas flow was between 32 and 36 sccm with a total pressure of 0.004 mbar, the substrate bias was set to -50 V and the deposition was performed for up to 60 min with the aim to build up thin films with a thickness of at least 2 to 3 µm. Other process parameters for each sputter mode can be gathered from Table 3.3. It was attempted to reach the highest possible power for each combination of target and sputter method to see what was feasible and still sustain a stable plasma. With an increasing content of

Die approbierte gedruckte Originalversion dieser Diplomarbeit ist an der TU Wien Bibliothek verfügbar
The approved original version of this thesis is available in print at TU Wien Bibliothek.
TU WIEN Bibliothek Your knowledge hub

aluminum in the target, the electrical conductivity declines considerably which explains why the 20/80 target was set to lower currents compared to the others.

Table 3.3. Process parameters for deposition

		Parameter		
Target	Sputter Mode	Current (A)	Voltage (V)	Power (W)
50/50	DC	1.00	390 – 437	390 – 437
	BPDC-50	0.94 – 1.01	376 – 404	380
	BPDC-250	1.14 – 1.17	222 – 263	300
33/67	DC	0.60	472 – 502	283 – 301
	BPDC-50	0.48 – 0.51	490 – 521	250
	BPDC-250	0.96 – 0.98	306 – 313	300
20/80	DC	0.25	688 – 696	172 – 174
	BPDC-50	0.28 – 0.34	588 – 714	200
	BPDC-250	0.85 – 0.90	333 – 353	300

BPDC-50 – Bipolar Pulsed DC, 50 kHz, 496 ns; BPDC-250 – Bipolar Pulsed DC, 250 kHz, 1616 ns.

Die approbierte gedruckte Originalversion dieser Diplomarbeit ist an der TU Wien Bibliothek verfügbar
The approved original version of this thesis is available in print at TU Wien Bibliothek.
TU WIEN Bibliothek Your knowledge hub

4 Film Growth and Structure

On an atomistic scale, film growth starts when target atoms hit the substrate surface, undergo a phase transformation from vapor to solid (condensation) and are bound to this surface in a way that they cannot be re-evaporated. If these atoms show certain mobility after the impact, they are called "adatoms". These atoms have a significant effect on the growth mechanism. During the growth itself, three major factors influence the resulting film properties: the substrate surface condition (for example the surface roughness or contamination), the deposition process (for example system geometry and incident angle distribution) and the film growth mechanisms (mobility of adatoms, nucleation, ion bombardment). Especially the surface properties can have a major influence, for example contamination as it can affect the nucleation process and lead – like a rough surface – to shadowing effects. Both result in high porosity, poor surface coverage and low film density of the deposited film. [1]

4.1 Nucleation

In a PVD process, the sputtered target atoms reach the substrates where they are chemically bonded to the atoms of the substrate surface. A mandatory requirement for the success of this process is a high temperature difference between the vapor and the substrate so that the vapor is supersaturated in front of the substrate. After condensation on the surface, the strength of the interaction between adatoms and surface atoms, the mobility of adatoms and the reaching of a (meta-)stable equilibrium position determine the morphology of the thin film: A strong interaction results in a low mobility which in turn enables many atoms to act as a nucleation site, resulting in fine-grained structures. It is also possible that amorphous films are formed as the adatoms are prevented from "finding" an equilibrium position of a crystal structure. Otherwise, the atoms diffuse on the surface until they find a preferential nucleation site, for example places of stronger bonding or increased coordination number (due to different chemistry or crystallographic orientation) or places which are morphologically beneficial like steps or lattice defects. The mobility also depends highly on the surface temperature because low temperatures inhibit diffusion and therefore mobility. Further, the incident energy of the atoms has a major impact as higher energies enable the atoms to move longer distances. It is also important which crystallographic plane an atom lands on because the different surface free

Die approbierte gedruckte Originalversion dieser Diplomarbeit ist an der TU Wien Bibliothek verfügbar
The approved original version of this thesis is available in print at TU Wien Bibliothek.
TU WIEN Bibliothek Your knowledge hub

energies on different orientations affect the surface diffusion. In turn, all these parameters result in different growth rates, and certain orientations can overgrow others. [1], [13]

In this context it is also important to talk about the different cases in which nucleation can occur: If adatoms are attached to defects and other irregularities, one speaks of a heterogeneous nucleation, whereas the homogeneous nucleation forms clusters with other atoms due to thermal fluctuations. The nuclei can only stably grow if they reach a certain size, depending on the energies involved in the process; for example, the energy gained if chemical bonds are formed, or the energy consumed in the formation of new surfaces, more precisely the surfaces of the nuclei. Since in heterogeneous nucleation a part of the surface is provided by the object to which the atoms bind, much less energy is required than in homogeneous nucleation. [13]

4.2 Growth

The growth of the nuclei can be described with either one of three general growth modes (also see Figure 4.1): [13]

- Island growth (Volmer-Weber): condensed atoms have a stronger bond to other atoms than to the substrate and/or only slow diffusion is possible
- Layer-by-layer growth (Frank-van der Merwe): condensed atoms have a stronger bond to the substrate than to other atoms and/or fast diffusion is possible
- Mixed growth (Stranski-Krastanov): the atoms start with a layer-by-layer growth but at a certain point it is more beneficial to form islands

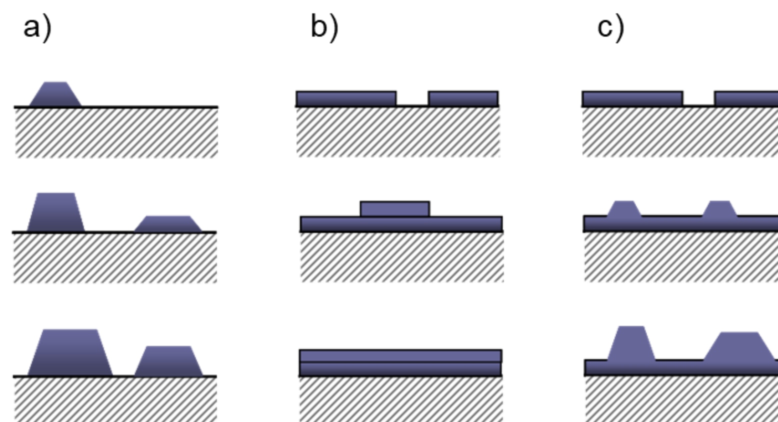

Figure 4.1. Schematic depiction of the three different growth modes. **a)** island growth (Volmer-Weber), **b)** layer-by-layer growth (Frank-van der Merwe), **c)** mixed growth (Stranski-Krastanov) – adapted from [14].

TU Bibliothek Your knowledge hub WIEN
Die approbierte gedruckte Originalversion dieser Diplomarbeit ist an der TU Wien Bibliothek verfügbar
The approved original version of this thesis is available in print at TU Wien Bibliothek.

While the material covers the substrate, an interface is forming. Depending on the substrate surface condition, chemical reactions between adatoms and substrate or interdiffusion mechanisms (atoms diffuse into a different material), different types of interfaces are chemically produced (see also Figure 4.2): [1]

- Abrupt: poor surface condition, no interdiffusion, nearly no chemical reaction or no solubility; rough surfaces can lead to mechanical interlocking
- Diffusion: interdiffusion leads to a compositionally graded interface without compound formation; needs sufficient solubility and time
- Compound: interdiffusion which results in the formation of a new compound (chemical reactions); often followed by volumetric changes and stresses
- Pseudodiffusion: graded composition due to “graded” deposition, where one material is deposited first, and the other material is gradually implemented
- Combinations of the above

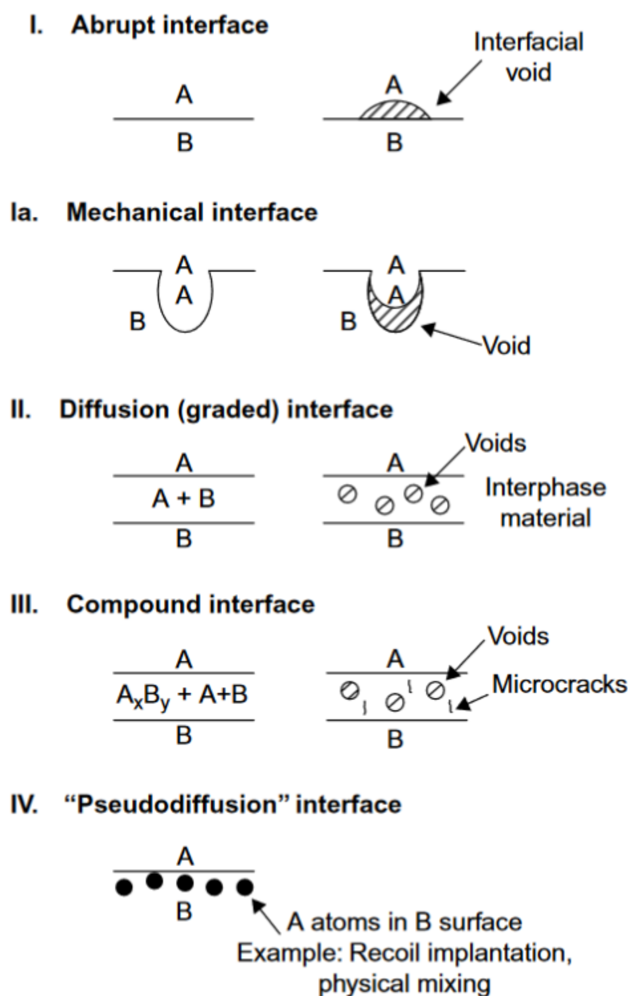

Figure 4.2. Illustration of the different interface types (adapted from [1]).

Die approbierte gedruckte Originalversion dieser Diplomarbeit ist an der TU Wien Bibliothek verfügbar
The approved original version of this thesis is available in print at TU Wien Bibliothek.
TU WIEN Bibliothek Your knowledge hub

One special type of growth is epitaxy, where atoms of the thin film sit on the natural lattice sites of the substrate crystal lattice, meaning that both have the same crystal lattice. If film and substrate are made of the same material, it is referred to as homoepitaxy, while it is called heteroepitaxy if the materials are different. For the second case it is important that both materials are within the same crystal class so that discrepancies between the two natural lattices are as small as possible (small lattice mismatch). [13] This is also important as the distortion in the thin film accumulates with increasing film thickness, resulting in lattice strains and the formation of so-called misfit dislocations to compensate the strain. [1]

4.3 Structure Zone Models – SZM

Structure Zone Models are a useful tool to describe the relation between parameters of a PVD process and to illustrate their influence on the thin film morphology. From the 1960s on, scientists stated different models, always adding a new parameter to address new developments of deposition processes. One of the most recent ones is depicted in Figure 4.3. [15]

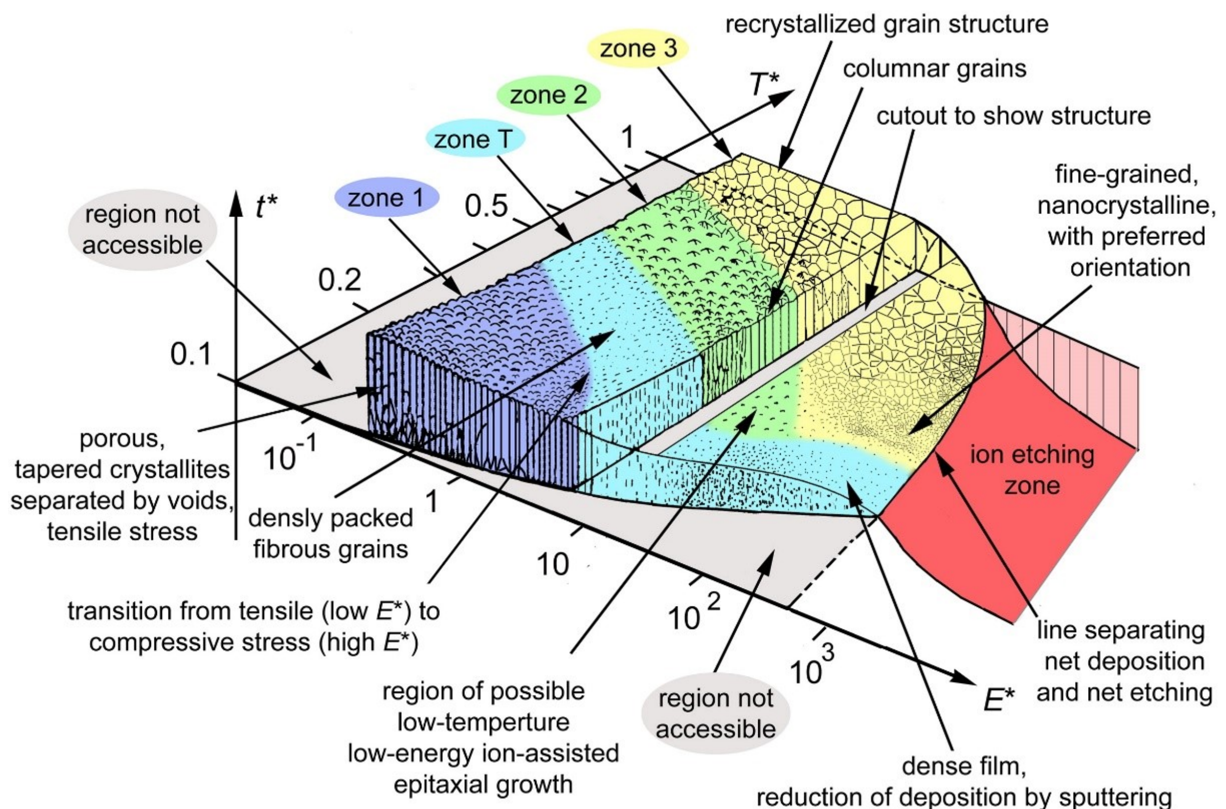

Figure 4.3. SZM after Anders. It shows the influence of the generalized temperature T*, the normalized energy flux E* and the net film thickness t* on the growth morphology. [15]

Die approbierte gedruckte Originalversion dieser Diplomarbeit ist an der TU Wien Bibliothek verfügbar
The approved original version of this thesis is available in print at TU Wien Bibliothek.
TU WIEN Bibliothek Your knowledge hub

On the one hand it shows the traditional classification of the different zones, but on the other hand it uses much more complex parameters than previous models: Instead of simply calculating the homologous temperature (film growth temperature divided by melting temperature of the film, in Kelvin), the generalized temperature T* was introduced. It adds a temperature shift to the homologous temperature which is caused by the potential energy of atoms, ions and other particles impacting on the substrate (for example ionization energy or cohesive energy). It results in an additional heating of the impact region and can affect the film growth. The second axis shows the normalized energy E* which replaces the traditional pressure axis and refers to the kinetic energy of impacting ions. It considers the natural energy of ions in a plasma and an acceleration due to the electrical field and it can be easily increased by applying a negative bias to the substrate. Due to different displacement and heating processes on the substrate, it can have a major influence on the film morphology. In this new SZM, a third axis is added which shows the net film thickness t* reached for a specific combination of T* and E*. It considers not only the increase of the thickness during the deposition, but also the decrease due to densification or re-sputtering of film atoms. At a certain combination, ion etching of the substrate begins, during which more atoms are re-sputtered than deposited. This can be mainly reached by applying an even higher bias to the substrate, which is done for plasma etching (see Chapter 3.2). Some combinations of T* and E* are physically not possible, for example the region of low T* and high E*. First, high energy transfer leads to heating of the substrate or coating, and temperatures below a certain point cannot be reached anymore. Furthermore, particles of a plasma are accelerated to a certain minimum velocity and a lower threshold of the energy exists; therefore, there is a second inaccessible region for low E*. [15]

As mentioned above, the different zones of the SZM were already described in previous models. Zone 1 is characterized by a porous, columnar morphology which results from poor adatom diffusion due to low surface temperatures and low incident energies. Both rough surfaces and off-normal deposition lead to geometrical shadowing and the formation of valleys which cannot be filled due to the low diffusion rate. If either E* or T* is increased, there is a gradual move to zone T (transition zone) where the morphology is mainly determined by the bombardment of the target with high-energy atoms. These atoms are able to displace film atoms at peaks and transfer them to the valleys, resulting in a more fibrous and dense morphology. A further increase of E* or T* leads to a rise of the deposition rate (zone 2). The diffusion rate also rises and the thin film experiences densification and grain growth, but still shows the columnar structure from the beginning. In zone 3, diffusion through the bulk is possible and

Die approbierte gedruckte Originalversion dieser Diplomarbeit ist an der TU Wien Bibliothek verfügbar
The approved original version of this thesis is available in print at TU Wien Bibliothek.
TU WIEN Bibliothek Your knowledge hub

recrystallization occurs in addition to densification and grain growth. Often, the individual columns evolve from polycrystalline to monocrystalline. [1]

Die approbierte gedruckte Originalversion dieser Diplomarbeit ist an der TU Wien Bibliothek verfügbar
The approved original version of this thesis is available in print at TU Wien Bibliothek.
TU WIEN Bibliothek Your knowledge hub

5 Characterization – Methods and Parameters

5.1 Hardness and Elastic Modulus

Nanoindentation is an important method to determine mechanical properties like hardness, elastic modulus, or stiffness of thin films. It can be performed in three different modes, either depth-, location- or phase-controlled. The first produces a high precision depth profile of the stiffness – even for multilayered thin films. The second is applied if someone is interested in the mechanics of different structural elements of the material, like grain boundaries or pores. The last is used for multiphase materials where the properties of a specific phase can be determined. [16]

In general, nanoindentation is performed like a conventional hardness test: A body of known geometry is indented into a material and the remaining indentation is related to the applied force. For nanoindentation, a so-called Berkovich tip is used, a three-sided diamond pyramid with a precise tip shape and a tip radius of 50 to 150 nm. In contrast to the conventional tests, the result is a load-displacement curve (see Figure 5.1) recorded during the loading and unloading process from which the hardness and the elastic modulus can be derived. [17]

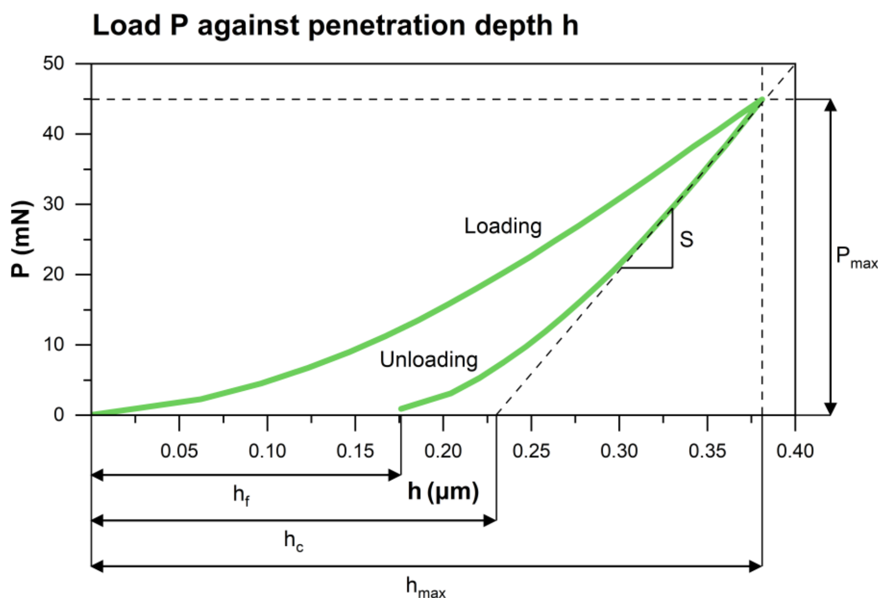

Figure 5.1. Example of a load-displacement curve obtained during a nanoindentation test. The indicated parameters are necessary for the calculation of the hardness and elastic modulus of the specimen: P_{max} – maximum applied load, S – contact stiffness, h_f – final depth, h_c – contact depth, h_{max} – maximum depth. For further explanation see text.

Die approbierte gedruckte Originalversion dieser Diplomarbeit ist an der TU Wien Bibliothek verfügbar
The approved original version of this thesis is available in print at TU Wien Bibliothek.
TU Bibliothek WIEN Your knowledge hub

During loading, the material experiences a transition from purely elastic to plastic behavior, whereby the maximum applied load is selected in such a way that the plastic zone can be fully developed within the observed material (for example only within the thin film and not in the substrate below). Furthermore, it is assumed that the material behaves only elastically during unloading, although plastic deformation can also occur. [17] Especially for brittle solids, this provides a good approximation. The system of indenter and sample is represented by two serially combined springs, for which the reduced elastic modulus E_r is derived with the following equation (E – elastic modulus, ν – Poisson's ratio, s – sample, i – indenter): [16]

$$\frac{1}{E_r} = \left(\frac{1-\nu_s^2}{E_s}\right) + \left(\frac{1-\nu_i^2}{E_i}\right) \tag{2}$$

By calculating E_r with Equation (4) and inserting it into Equation (2), the wanted elastic modulus of the sample is obtained. To be able to calculate the hardness H (see Equation (3); P_{max} – maximum loading, A – contact area) and the reduced elastic modulus E_r (see Equation (4); β – correction factor, S – contact stiffness (see next paragraphs), A – contact area), some other computations (often after the Oliver-Pharr model) must be performed to obtain the area of the indentation. This is necessary as the indentations have a size of a few hundred nanometers to a few micrometers and it is difficult to determine the area visually. [16]

$$H = \frac{P_{max}}{A} \tag{3}$$

$$E_r = \frac{1}{\beta} S \frac{1}{2} \frac{\sqrt{\pi}}{\sqrt{A}} \tag{4}$$

The computation starts with the mathematical description of the unloading part of the load-displacement curve. This is often done with a power law fit (see Equation (5)), where P is the applied load, h the resulting penetration depth, h_f the final penetration depth after unloading and B and m are fitting parameters: [17]

$$P = B(h - h_f)^m \tag{5}$$

The derivative of this function evaluated at the maximum penetration depth h_{max} is the so-called contact stiffness S and used for calculating the contact depth h_c (see Equation (6)) and the reduced elastic modulus (see Equation (4)): [17]

$$h_c = h_{max} - \epsilon \frac{P_{max}}{S} \tag{6}$$

Die approbierte gedruckte Originalversion dieser Diplomarbeit ist an der TU Wien Bibliothek verfügbar
The approved original version of this thesis is available in print at TU Wien Bibliothek.
TU WIEN Bibliothek Your knowledge hub

The contact depth is defined as the penetration depth at maximum contact between indenter and material during unloading (at this point, the tip is still in contact with the material). [16] The parameter ϵ can be calculated with $\epsilon = \frac{2(\pi-2)}{\pi} = 0.72$, but is often replaced with 0.75 to consider that the material's behavior can deviate from the ideal one. With h_c the contact area A can be calculated, using a polynomial function like $A = C_1 h_c^2 + C_2 h_c + C_3 h_c^{\frac{1}{2}} + C_4 h_c^{\frac{1}{4}} + \cdots$, often referred to as *area function*. As the tip gets rounded during usage, the fitting constants C_i must be frequently adjusted to describe the contact area correctly. This is commonly done by testing a material with known hardness or modulus values. By inserting A into Equation (3), the hardness can be calculated. [17]

Both hardness and elastic modulus are computed for every indent performed during the experiment, resulting in curves showing the hardness or elastic modulus depending on the penetration depth. Regarding the hardness, the arithmetic mean is calculated, but only for the values at the plateau of the curve as they represent the peak hardness of the examined thin film (see Figure 5.2). Descending values after the plateau appear if the zone of plastic deformation reaches the softer substrate and the hardness decreases. To ensure that the zone is limited to the coating and to minimize substrate influence, only indents with indentation depths lower than 10 % of the coating thickness were used for the evaluation (according to Bückle's Rule [18]).

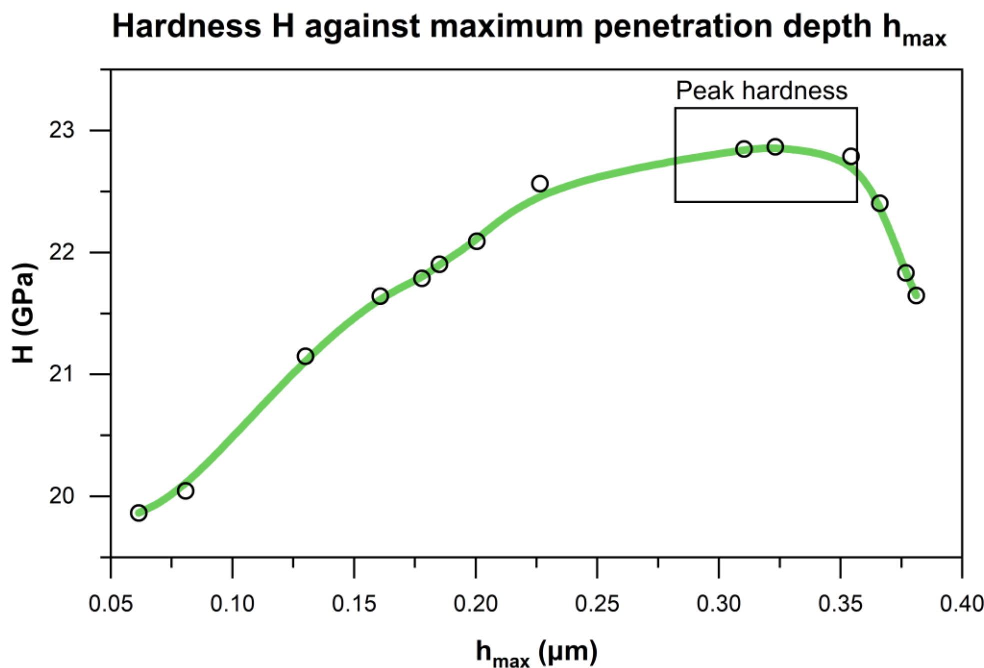

Figure 5.2. Example of a curve showing hardness against maximum penetration depth and the plateau from which the hardness values were obtained for the evaluation.

Die approbierte gedruckte Originalversion dieser Diplomarbeit ist an der TU Wien Bibliothek verfügbar
The approved original version of this thesis is available in print at TU Wien Bibliothek.
TU WIEN Bibliothek Your knowledge hub

The elastic zone is greater than the plastic one and thus extending far into the substrate. Therefore, E_s from Equation (2) is always a combination of the elastic moduli of both the thin film and the substrate. To properly estimate the elastic modulus of the thin film, a function is fitted to the curve (see Figure 5.3) and evaluated for $h_{max} = 0$, assuming that here the substrate has the least influence and only elastic behavior of the coating is observed. For this thesis, a power law fit was used because it best describes the data; the function is:

$$E(h_{max}) = E_0(1 + h_{max})^b \tag{7}$$

With E_0 being the wanted value and b a fitting parameter.

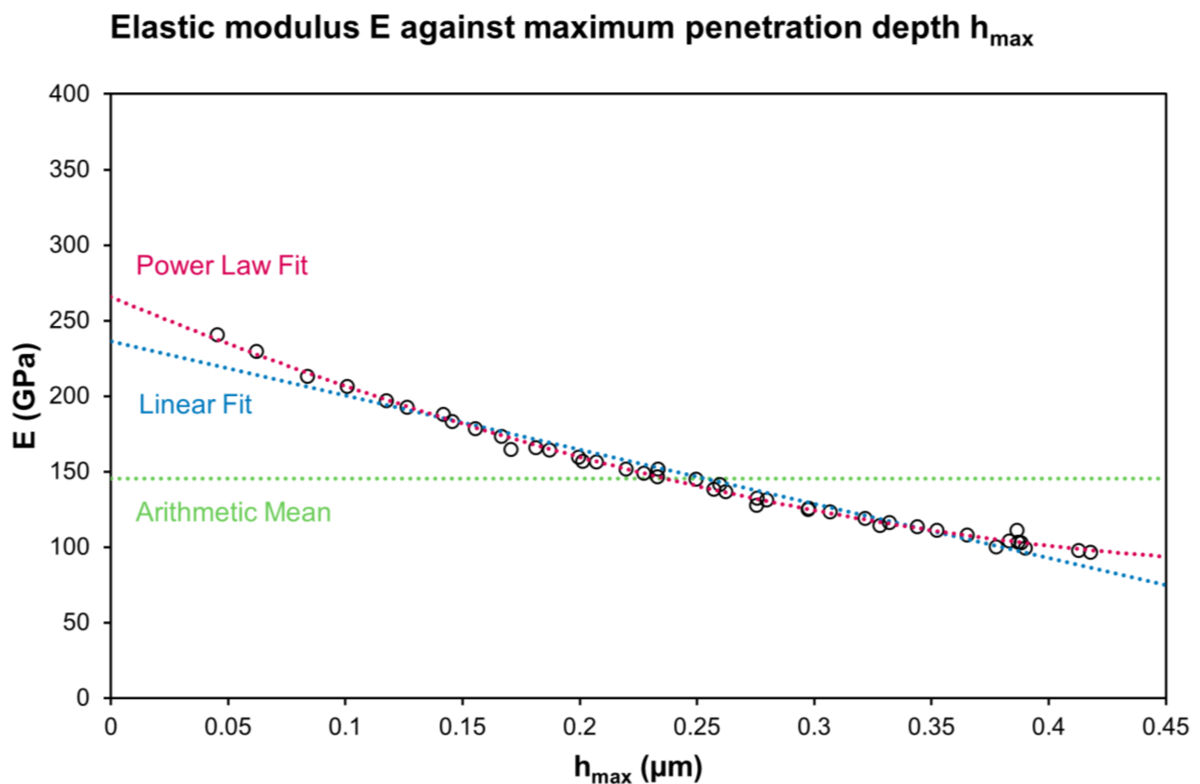

Figure 5.3. Example of a curve showing elastic modulus against the maximum penetration depth. As one can see, the power law fit (red) is more suitable to describe the data than the linear fit (blue) or the arithmetic mean (green).

For preparation, the austenitic steel samples were hot glued onto a round blank of hardened steel with a rigid polymer. The hardness was measured with a *CSIRO UMIS Nanoindentation System* with a standard Berkovich tip with a face angle of 65.3° and loads ranging from 2 to 50 mN. The analysis was done using the Oliver-Pharr model (for Poisson's ratios and elastic moduli see Table 5.1). Around forty measurement points, 20 µm apart from each other, were taken per sample so that the plastic zones of the individual indents did not interact.

Die approbierte gedruckte Originalversion dieser Diplomarbeit ist an der TU Wien Bibliothek verfügbar
The approved original version of this thesis is available in print at TU Wien Bibliothek.
TU WIEN Bibliothek Your knowledge hub

Table 5.1. Poisson's ratios of indenter and the targets

Material	Poisson’s ratio	Elastic Modulus (GPa)
Indenter	0.07	1141
Target	0.214 [19]	504 (maximum value of test series)

5.2 X-Ray Diffraction – XRD

When it comes to the investigation of crystallographic properties of a material, X-ray diffraction is a well-established and widely used method in the material sciences. Besides crystal structure, lattice symmetry, lattice parameters and atom positions within the lattice, crystallite size and layer thickness can also be determined. Further, the analysis of phases and their chemical composition, of the orientation of crystallites and of stresses within the material is feasible. [20]

To be able to obtain this information, the X-rays must be diffracted at the lattice planes of the crystal, which can also be described as the deflection of X-ray waves at the atoms. X-rays are used because their wavelength and the lattice spacing (the distance between specific lattice planes, which is unique for a material) are of similar size so that the diffracted waves show the greatest disturbance possible and provide the most information. The crystal lattice acts as a diffraction grating where the X-rays are scattered at the electron shells, following Bragg’s Law: [20]

$$2 * d_{hkl} * \sin \theta_{hkl} = n * \lambda \tag{8}$$

Bragg’s Law defines the parameters for constructive interference, where d_{hkl} is the lattice spacing, θ_{hkl} the incident angle of the beam, n the diffraction order and λ the wavelength. If an X-ray beam hits a material, it is diffracted at the surface, but also at the lattice planes inside the crystal, following Snell’s Law (angle of incidence and reflection are equal; see Figure 5.4). If the path difference between the reflected beams is a whole multiple of the wavelength, constructive interference (increasing amplitude of at least two overlapping waves) occurs. Also, if the wavelength and the incident angle are known, the lattice spacing can be calculated and the material can be identified. [20]

TU Bibliothek WIEN Your knowledge hub
Die approbierte gedruckte Originalversion dieser Diplomarbeit ist an der TU Wien Bibliothek verfügbar
The approved original version of this thesis is available in print at TU Wien Bibliothek.

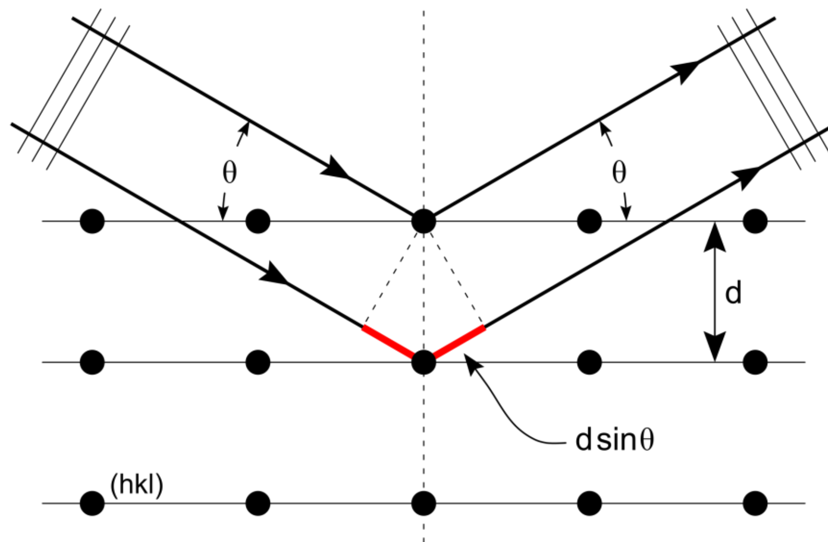

Figure 5.4. Graphical interpretation of Bragg's Law (adapted from [21]).

The wavelength is only defined if characteristic X-rays are used. Together with the so-called bremsstrahlung, they are part of the X-ray spectrum generated in a hot-cathode tube. A hot tungsten filament (cathode) emits electrons which are accelerated toward the anode (often made of copper), where they impact. 98 to 99 % of the electrons' energy is converted to heat and only 1 to 2 % leave the anode as X-rays. If the electrons are decelerated within the electrical field of the anode's atoms, the energy loss is emitted as bremsstrahlung. As this energy loss is produced randomly, the leaving X-rays have continuously distributed wavelengths. Contrary to the characteristic X-rays, which are generated because the electrons ionize the anode atoms at their inner shells. Electrons from outer shells fill these vacancies and the energy difference is emitted as X-rays, characteristic for the atom species and with a specific wavelength. For X-ray diffraction, the so-called $K_{\alpha 1}$, $K_{\alpha 2}$ and K_{β} X-rays are most important (see Table 5.2). [20]

Table 5.2. Wavelength of characteristic X-rays of copper (Cu) and tungsten (W) and corresponding *2θ* angles of α-Al_2O_3 for d = 0.174 nm [20], [22]

Element	Characteristic X-ray	Wavelength (nm)	*2θ* Angle (°)
	$K_{\alpha 1}$	0.154 059	52.55
Cu	$K_{\alpha 2}$	0.154 443	52.69
	K_{β}	0.139 223	47.16
W	$L_{\alpha 1}$	0.147 58	50.18

Die approbierte gedruckte Originalversion dieser Diplomarbeit ist an der TU Wien Bibliothek verfügbar
The approved original version of this thesis is available in print at TU Wien Bibliothek.
TU WIEN Bibliothek Your knowledge hub

These X-rays are emitted if an outer-shell electron fills a vacancy of the K shell. In case of the α X-rays, the electrons come from different energy levels of the L shell, whereas for β X-rays they originate from the M shell. They all have different energies and therefore different wavelengths and for the same lattice spacings, Bragg's Law is fulfilled for different incident angles (see Table 5.2). In a diffractogram (see Figure 5.5 and Figure 5.6) this is displayed as spectral lines, which all refer to the same crystal orientation. Also, diffractograms obtained with old X-ray tubes (more than 4000 operating hours) show tungsten $L_{\alpha 1}$ peaks (see Table 5.2) as tungsten gets deposited on the anode. This can lead to wrong identifications and therefore monochromators are used which create monochromatic $K_{\alpha 1}$ radiation. [20]

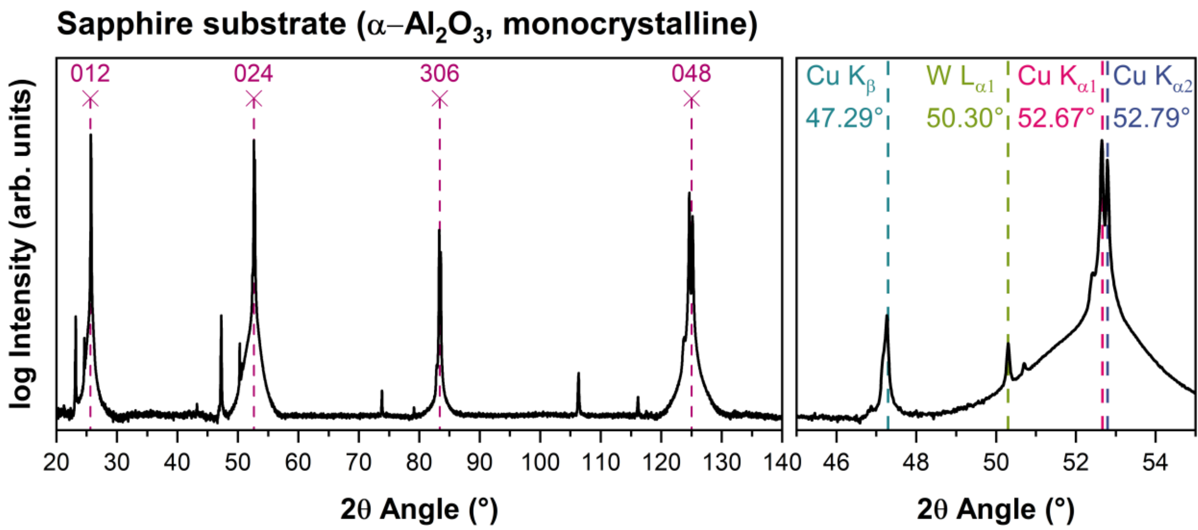

Figure 5.5. Diffractogram of a monocrystalline sapphire substrate, cut along the $(1\bar{1}02)$ plane. The spectral lines of copper $K_{\alpha 1}$, $K_{\alpha 2}$ and K_{β} radiation and the peak produced by tungsten L radiation are indicated.

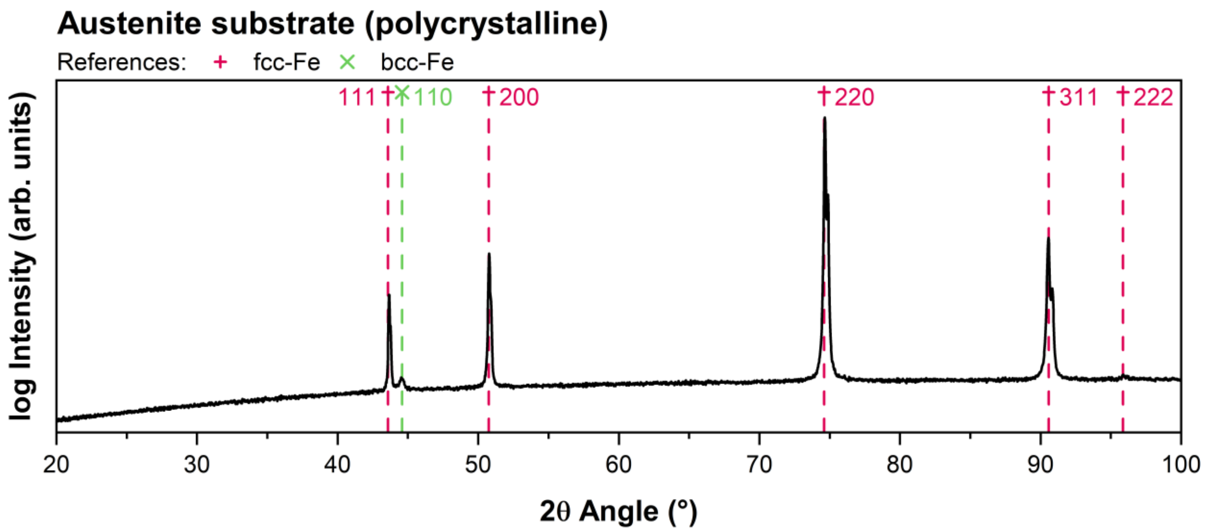

Figure 5.6. Diffractogram of a polycrystalline austenitic substrate.

Die approbierte gedruckte Originalversion dieser Diplomarbeit ist an der TU Wien Bibliothek verfügbar
The approved original version of this thesis is available in print at TU Wien Bibliothek.
TU Bibliothek WIEN Your knowledge hub

During the experiment, the X-ray source, the sample, and the detector are rotated against each other so that a predefined range of incident angles is examined. For this thesis, the Bragg-Brentano geometry with a θ-θ goniometer was used: The sample stays stationary while the source and the detector rotate around it. A diffractogram is obtained during the experiment and shows the X-ray intensity for every 2θ angle (angle between X-ray source, specimen, and detector). It shows peaks at 2θ angles where Bragg's Law is fulfilled. [20]

Important for the identification and characterization of a material and its phases, is the number, position, intensity, and shape of these peaks: [23]

- The diffractograms of well-crystallized, single-phase samples show sharp, distinct peaks which are easily assignable.
- With decreasing grain size, the peaks broaden and show lower intensities. This can lead to X-ray amorphous patterns with sustained and indistinct peaks. It is not possible to determine if the material is actually amorphous or it consists of nanocrystallites which cannot be seen with X-rays – at least not with XRD.
- An additional problem occurs with multiphase materials: The patterns of the individual phases can overlap which complicates the identification.
- Preferred orientations can be determined as the intensity of the corresponding peaks is significantly increased compared to the other orientations.
- It may also occur that the peaks are shifted compared to a perfect sample due to many reasons like bad sample preparation or stresses within the material. Different thermal coefficients of expansion lead to compressive or tensile stresses which in turn lead to either smaller or greater lattice spacings and therefore to shifted peak positions. Also, substitutional or interstitial atoms result in stresses.

For a qualitative phase analysis like in this thesis, the obtained diffractogram is compared to known XRD patterns with the same chemistry from global databases to identify the crystalline phases of the thin films. Only the sapphire and austenite samples were used for XRD measurements. Both substrates have well known peaks (see Figure 5.5 and Figure 5.6) and can be easily identified and distinguished from the thin film peaks in the diffractogram. The samples were cleaned with isopropanol and scanned over a 2θ angle between 5 to 120 ° with a *PanAlytical Empyrean Material Diffractometer*. The experiments were performed with a copper anode and a *GaliPIX* 2D hybrid pixel detector in one dimensional line scanning mode while the sample was rotated around the axis perpendicular to the sample's surface. The beam

TU WIEN Bibliothek Your knowledge hub
Die approbierte gedruckte Originalversion dieser Diplomarbeit ist an der TU Wien Bibliothek verfügbar
The approved original version of this thesis is available in print at TU Wien Bibliothek.

was formed in such a way that it hit the samples on an area of 3 mm times 3 mm to ensure that the measured area did not extend beyond the sample. The diffractograms were used to determine the crystal structure of the thin films and whether a solid solution or multiphase coating was formed.

Some samples, which showed a solid solution pattern, were also measured with a *X'Pert MPDIII Diffractometer* in non-ambient mode (copper anode, θ-θ goniometer, Bragg-Brentano geometry, X' Celerator semiconductor detector). It allows heating and measuring of the specimens in different atmospheres or in vacuum, as in this thesis (10^{-5} mbar). The temperature was raised from 600 °C to 1100 °C and a diffractogram was obtained every 15 °C. This experiment was performed to investigate the thermal stability of samples, which show a solid solution, as well as to observe phase changes at elevated temperatures.

5.3 Electron Microscopy

Due to the wavelength of visible light, the resolution of classic light microscopes is limited to at most 0.2 µm and thus to a magnification of approximately 1000 times. [24] To achieve higher magnification, Ernst Ruska and Max Knoll built the first electron microscope in the early 20th century [25], because electrons have far smaller wavelengths and currently can reach a resolution of 0.1 nm. Subsequently, they enabled new possibilities of material examination as electron microscopy also allows easy determination of chemical compositions, crystallographic properties, shapes and sizes of the samples or other chemical and physical properties up to magnifications of 500 000 times. [26]

5.3.1 Scanning Electron Microscopy – SEM

The first step in obtaining an image is to generate a focused electron beam. In regular SEMs, a filament of tungsten or lanthanum hexaboride (LaB_6) is heated up until it emits electrons, which are then accelerated by an anode (acceleration voltage of about 10 to 30 kV). A newer source variant is the field emission gun SEM (FEG-SEM), which provides a higher brightness and thus better image resolution. The general principle of this gun is an emitter such as a tungsten single-crystal with a sharpened tip to which a high negative potential (several kilovolts) is applied. The high potential gradient between the crystal and the anode leads to the emission of electrons

TU Bibliothek Die approbierte gedruckte Originalversion dieser Diplomarbeit ist an der TU Wien Bibliothek verfügbar
WIEN Your knowledge hub The approved original version of this thesis is available in print at TU Wien Bibliothek.

at the emitter surface. This electron beam has a far smaller diameter than that produced by a thermionic source, which is the reason for the higher brightness. [27] Independent of the gun, the electrons pass, after acceleration, through a system of electromagnetic coils, electrostatic and/or magnetic lenses and apertures (electron columns). This not only focuses the beam and reduces its diameter, but also moves it across the sample in a raster. In that way, the diameter of a tungsten-filament electron gun can be decreased from initially 50 µm to 2 nm. In general, this electron column as well as the specimen chamber are under high vacuum so that primary electrons and electrons leaving the sample after interaction experience almost no impact events and therefore have the highest possible energy. This is important because higher electron beam energy leads to a larger interaction volume in the sample, resulting in signals coming from a greater sample depth (see Figure 5.7). [26]

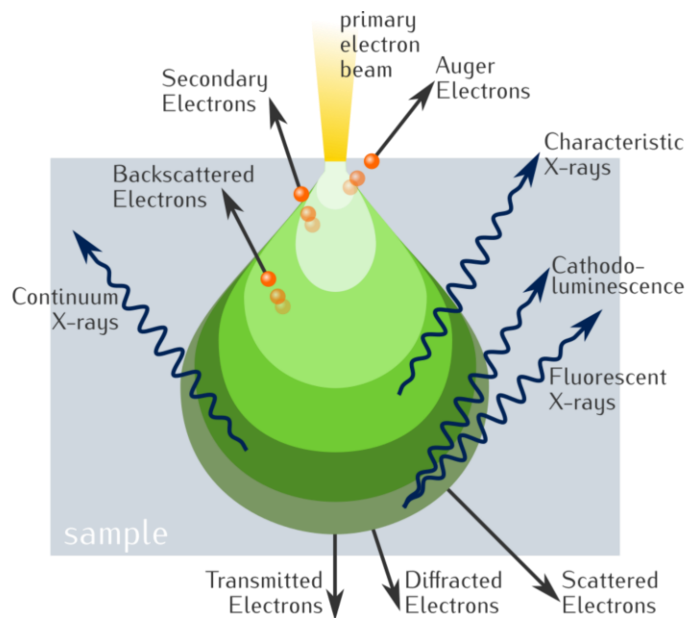

Figure 5.7. Interaction volume of different signals created after primary electrons hit the sample. [28] SEs can only escape maximum depths of 10 nm due to their low energy. [27]

These signals are produced by the interaction of primary electrons and the specimen and are detected for each point of the raster. For some of the applications, it is necessary that the sample is electrically conductive or sputtered with gold or graphite to provide a high-resolution image. [26] Like in optical microscopes, the lenses of electron microscopes can also have defects, resulting in unfocused images. There are two major lens errors and the first is the spherical aberration. The beam cannot be focused on a single point (see Figure 5.8a) as electrons which pass the magnetic lenses in outer regions are more refracted than the ones passing the middle. This happens because the magnetic field increases with increasing distance from the axis, but the effect can be reduced if the aperture is limited. [27] The second error is the so-

Die approbierte gedruckte Originalversion dieser Diplomarbeit ist an der TU Wien Bibliothek verfügbar
The approved original version of this thesis is available in print at TU Wien Bibliothek.
TU WIEN Bibliothek Your knowledge hub

called astigmatism, which arises due to imperfect lenses or contaminated apertures. Both produce a magnetic field, which is stronger in one direction than in the perpendicular one, which leads to the distortion of the beam so that its cross section is no longer spherical but elliptical. Changing the focus from overfocused to underfocused, distorts the image in perpendicular directions (see Figure 5.8b). [26] It can be corrected with coils ("stigmator") which create an astigmatism themselves that compensates the original one. [27]

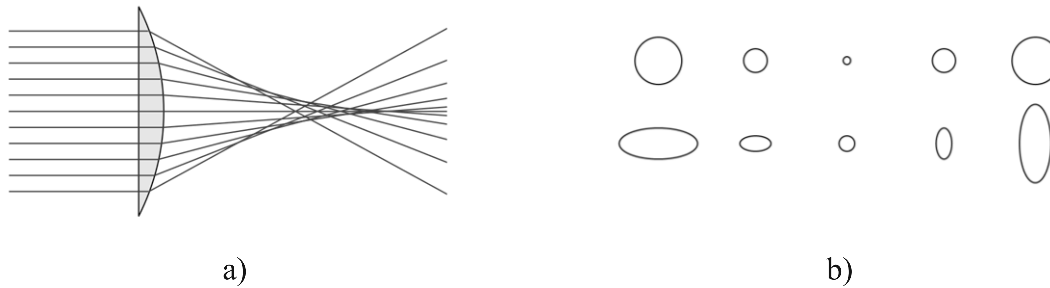

Figure 5.8. Schematic illustration of **a)** spherical aberration (adapted from [29]) and **b)** astigmatism while changing the focus from overfocused to underfocused.

The interactions mentioned above are scattering processes in which the primary electrons are inelastically or elastically scattered at the atoms of the sample. In the first case, the electron experiences an energy loss because, for example, it hits an outer-shell atomic electron, which is then extracted as a secondary electron (SE). Other reasons are the ejection of inner-shell atomic electrons by the primary ones which results in the emission of characteristic X-rays. Also, the electron can be decelerated because of the electrical field of the sample atoms and bremsstrahlung is produced (for more information see Chapter 5.2). The electron can also be deflected by the atomic electrical field of the sample without energy loss (elastic scattering). This changes the trajectory so that the electron can leave the material again. It is then called backscattered electron (BSE). [26]

To create a SEM image, the SE or BSE signal must be detected. For SEs, the so-called Everhart-Thornley detector is commonly used. It consists of a scintillator crystal which converts the impact of electrons into light, which is then transformed into an electrical signal by a photomultiplier. [27] As SEs have generally low energies (mostly below 5 eV [26]), a positive potential is applied to a grid in front of the crystal and the crystal itself to attract and accelerate the electrons. [27] Some BSEs with energies slightly above 5 eV are also detected, but their amount is negligible. The majority of the BSEs is collected by a Robinson detector, for example. It is positioned directly above the sample in a ring shape around the exit of the electron column. It is also operated by means of a scintillator crystal, but there are also other detector variants

Die approbierte gedruckte Originalversion dieser Diplomarbeit ist an der TU Wien Bibliothek verfügbar
The approved original version of this thesis is available in print at TU Wien Bibliothek.
TU WIEN Bibliothek Your knowledge hub

based on semiconductors. Due to the relatively long distance between the BSE detectors and the sample, only BSEs can reach it due to their higher energies. [27]

SE images show a topography contrast, where edges or areas facing the detector appear much brighter than cavities or averted surfaces. This is possible because more electrons can escape from edges and are more often collected by the detector from facing surfaces. This creates the illusion of a three-dimensional object (see Figure 5.9). The topography contrast can be also seen in BSE images as the detector position creates a natural shadowing effect. [27] Their most important application, however, is compositional contrast: Regions with a high mean atomic number (Z) appear brighter in the image than those with lower atomic numbers. On the one hand, this occurs because elements with high atomic numbers can deflect more primary electrons than ones with lower numbers. On the other hand, detectors are sensitive to the electron energy and favor high energies. As heavier elements can backscatter primary electrons with higher energies, regions with higher Z appear brighter. [26] Since only the mean atomic number can be shown, the significance of this analysis decreases with an increasing number of elements within the sample.

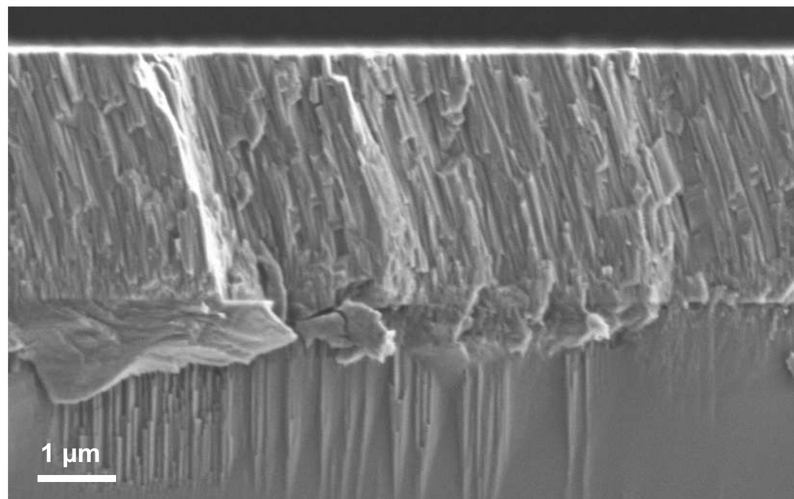

Figure 5.9. Topography contrast in a SE image (10 000 X). The edges are brighter than flat areas or averted surfaces.

Furthermore, SEM can be used to perform chemical analyses, as characteristic X-rays leaving the sample can be detected by Energy Dispersive X-Ray spectrometers (EDX; see Chapter 5.3.3).

In this thesis, SE images were used to determine the thickness and the overall appearance and the microstructure of the thin films produced. For this purpose, the sapphire or silicon platelets were broken in areas without cracks and the thickness of the cross section was determined using

Die approbierte gedruckte Originalversion dieser Diplomarbeit ist an der TU Wien Bibliothek verfügbar
The approved original version of this thesis is available in print at TU Wien Bibliothek.
TU Bibliothek WIEN Your knowledge hub

an in-built software program. The images were taken with a *Zeiss Sigma 500 VP FEG-SEM* with an electron acceleration voltage of 3.00 kV and at a ten-thousand-fold magnification.

5.3.2 (Scanning) Transmission Electron Microscopy – (S)TEM

The construction of a (S)TEM (see Figure 5.10) is in principle similar to the one of a SEM: An electron gun, also either a tungsten or LaB_6 filament or a field emission gun, produces an electron beam, which is first accelerated (100 to 300 kV) and then focused onto the sample by a system of electromagnetic lenses. [30] The whole column is under high vacuum so that the electrons can travel a length of one to two meters. [31] In contrast to the SEM, the (S)TEM method requires specimens which are thin enough so that electrons can pass them without too much energy loss or scattering. Therefore, and for acceleration voltages as mentioned above, thicknesses of less than 10 to 100 nm are necessary. One possibility to prepare samples for (S)TEM analyses is the focused ion beam technique (FIB). A beam of heavy ions like gallium (Ga^+) with energies of around 30 keV hits the specimen surface and cuts two parallel trenches. The thin piece of sample between these trenches is then cut out and extracted. [30]

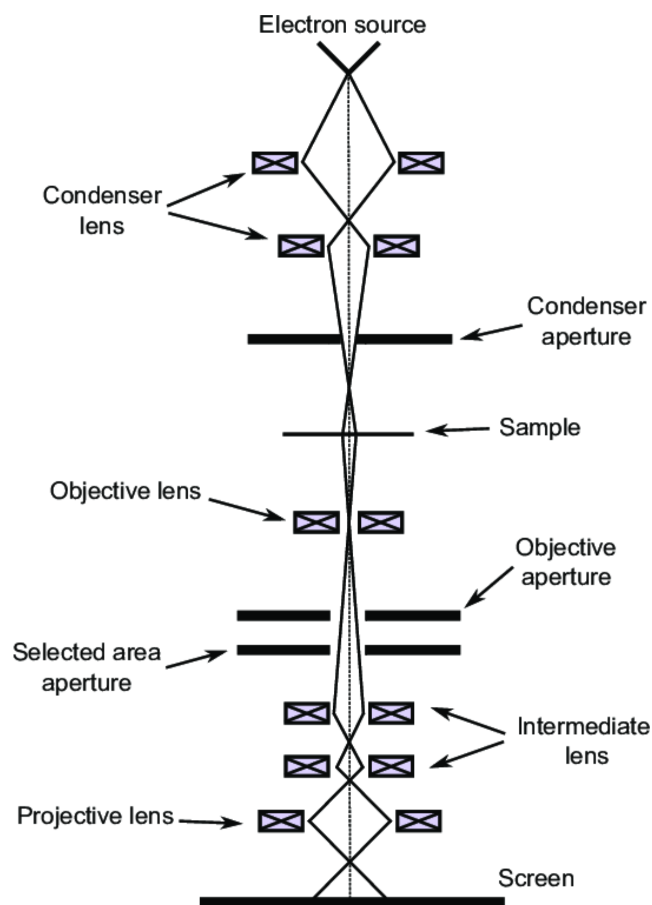

Figure 5.10. Schematic setup of a TEM. [32]

Die approbierte gedruckte Originalversion dieser Diplomarbeit ist an der TU Wien Bibliothek verfügbar
The approved original version of this thesis is available in print at TU Wien Bibliothek.
TU Bibliothek WIEN Your knowledge hub

The traditional TEM has a fixed beam, whereas the STEM uses scanning coils to move the beam in a raster over the sample. It is possible to generate images with a (S)TEM, but also to analyze the crystal structure of the specimen with electron diffraction patterns or to determine the chemical composition of the whole material or specific phases. Due to the different operational modes, TEM and STEM are more suitable for different applications, which are explained in the next paragraphs. [30]

To generate images or diffraction patterns with TEM, the parallel-beam mode is applied most often: Two condenser lenses (including apertures) adjust the beam in such a way that it becomes parallel with a diameter of a few micrometers. It shines through the sample where it is converted into an image or a diffraction pattern by the objective lens, which also magnifies both. They are further magnified by additional lenses and finally displayed on a fluorescent screen or on a monitor by the means of a camera. Whether the result is an image or a diffraction pattern, is determined by the intermediate lenses, which are positioned before the screen. To obtain a diffraction pattern with the parallel beam, the selected area aperture must limit the examined area, which is why this method is called Selected Area Electron Diffraction (SAED). The patterns produced show periodic arrays of spots (monocrystals) or rings (amorphous or polycrystalline materials) which can be indexed to determine the crystal structure and to identify defects. [30]

The TEM can also be operated with a convergent beam, but this mode is more common in STEM. Next to imaging (with electron detectors underneath the projective lens), it also enables microanalyses of phases or microdiffraction. The scanning beam is formed by the condenser lenses, but in contrast to the traditional TEM, where only the second condenser lens is adjustable, both lenses can be modified to produce a beam with a small diameter (0.1 nm) and a higher current. Further, a third condenser lens is needed to form the beam. Compared to SEM, the lens aberrations can be better controlled in a STEM, resulting in minimum beam diameters of 0.5 Å and thus in nanoscale imaging and analyses. The diffraction pattern obtained with a convergent beam (Convergent Beam Electron Diffraction, CBED) provides more information than with a parallel beam: Due to the smaller diameter, the spatial resolution is better, but it also reveals the crystal symmetry like point or space groups. Unlike SAED, CBED patterns show intensity discs rather than spots. [30]

STEM images can be taken in two major modes (see Figure 5.11): Bright field (BF) images show a contrast of sample thickness or atomic number Z and are created by not scattered or low-angle scattered (< 0.5°) electrons. The thicker the material or the higher the Z, the darker

TU Bibliothek Die approbierte gedruckte Originalversion dieser Diplomarbeit ist an der TU Wien Bibliothek verfügbar
WIEN Your knowledge hub The approved original version of this thesis is available in print at TU Wien Bibliothek.

is the corresponding area in the image since less electrons can pass through the sample without scattering and thus hit the BF detector (see Figure 5.11). The second mode produces dark field (DF) images and uses electrons scattered at an angle between 0.5 to 3° (low-angle annular dark field, LAADF or ADF) and 3 to 10° (high-angle annular dark field, HAADF), each collected by the corresponding detector (see Figure 5.11). DF images are inverted compared to BF images and the darker regions represent thinner sample areas or lighter elements. In addition, HAADF images have a similar informational content about the composition as BSE images from SEM. In TEM, electrons are collected by the objective aperture for both BF and DF images, although for the latter the incident beam must be additionally tilted until the diffracted beam can be detected. [30]

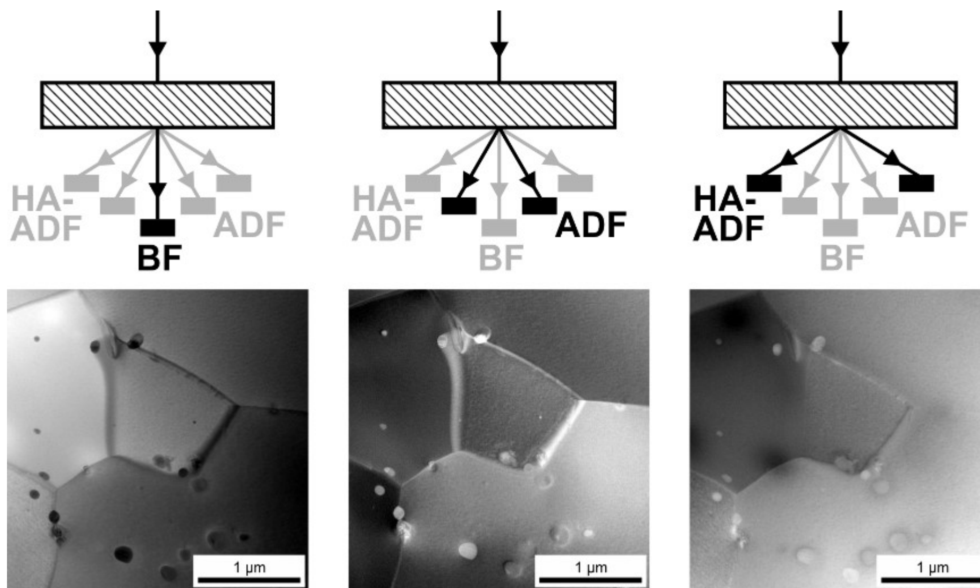

Figure 5.11. Different imaging modes in STEM and the positions of their detectors after the beam passed the sample: bright field, low-angle annular dark field and high-angle annular dark field. [33]

It is also possible to determine the chemical composition of a sample with (S)TEM, for example with the methods Energy Dispersive X-Ray Spectroscopy (EDX) and Electron Energy Loss Spectroscopy (EELS), which will be explained in Chapter 5.3.3 and Chapter 5.3.4.

For this thesis, a *TECNAI F20* (S)TEM at USTEM (University Service Centre for Transmission Electron Microscopy; TU Wien, Austria) was used to determine the ratio of Ti, Al, and N (with EELS, see Chapter 5.3.4) and the crystal structure of chosen samples. It has an extreme field emission gun, which combines the high brightness of a FEG with the high current of thermal emission and was performed with 200 kV. For the EELS analysis a *Gatan GIF Tridiem* image

Die approbierte gedruckte Originalversion dieser Diplomarbeit ist an der TU Wien Bibliothek verfügbar
The approved original version of this thesis is available in print at TU Wien Bibliothek.
TU WIEN Bibliothek Your knowledge hub

filter system was used. The TEM was operated by Dipl.-Ing. Tomasz Wojcik and the analysis of the SAED images was performed with CrysTBox. [34]

5.3.3 Energy Dispersive X-Ray Spectroscopy – EDX

The EDX method uses characteristic X-rays produced by primary electrons in a SEM or TEM to first identify and then quantify the elements in the sample. To do so, the detector must be able to distinguish between the different energies of the X-ray photons ranging from 50 eV to 30 keV. Eligible detectors are made of semiconductors (high-purity germanium (Ge), Si(Li) (silicon doped with lithium) or Silicon Drift Detectors (SDD)). In case of the Si(Li) detector, the semiconductor is coated with a layer of gold (first electrode) where a bias voltage is applied to the detector. It is also connected with a pre-amplifying field effect transistor, and both are attached to a copper bar (second electrode), whose other side is cooled with liquid nitrogen. The detector is shielded from the sample chamber with a glass, mostly made of beryllium, so that it can be constantly evacuated. With beryllium glass only X-rays with energies above 1 keV can be detected as the subjacent ones are absorbed. [27] Nowadays, SDDs are more common. Their design is similar to Si(Li) detectors, but with the great difference that the second electrode is more complex: A central anode is placed within several electrode rings to which a potential pattern is applied. In that way, all free electrons in the semiconductor are collected and detected by the anode. [26]

If the semiconductor photoelectrically absorbs one of the X-rays, an inner-shell electron of the semiconductor's atoms is ejected. It is then inelastically scattered at other atoms, losing its energy to their outer-shell electrons. These are raised from the valence band to the conduction band and create electron-hole pairs and thus free electrons in the semiconductor. This results in a measurable current from the first to the second electrode. The number of raised electrons can be calculated by dividing the photon energy by the mean energy that is necessary to create the pair (Si: 3.8 eV, Ge: 2.9 eV [27]). [26]

To be able to analyze the signal according to its height, it must be amplified again after the preamplifier, and it is then averaged over the so-called process time (a few tens of microseconds). Multichannel pulse-height analyzers take these amplified signals, allot them to a channel and measure their height, resulting in a histogram. Each channel covers a certain range of energy, and the height represents the number of photons whose energies fit the channel range. During the processing of each signal, the detector cannot respond to other arriving

Die approbierte gedruckte Originalversion dieser Diplomarbeit ist an der TU Wien Bibliothek verfügbar
The approved original version of this thesis is available in print at TU Wien Bibliothek.
TU Bibliothek WIEN Your knowledge hub

electrons which is called “dead time”. [27] The collected spectrum is then displayed on the monitor, where further analyses can be carried out. A perfect spectrum would show the peaks as lines but the number of electron-hole pairs created by an incoming characteristic X-ray follows a Gaussian distribution. Therefore, the peaks are also laterally extended, which results in peak overlapping, making the identification more difficult. [26] Another problem occurs if the energy difference of two peaks is smaller than the energy resolution of the device. For example, if the resolution is 130 eV, the titanium (Ti) $L_{\alpha 1}$ peak (452.2 eV) is too close to the nitrogen (N) $K_{\alpha 1}$ peak (392.4 eV) to distinguish both. [35] Now, the Ti as well as the N X-rays end up in the same channel which results in a wrong quantification of N with increasing Ti concentration. To illustrate this, the results of the EDX quantification of this thesis were compared, for which the concentrations of N and Ti of the respective targets were averaged and plotted against each other (see Figure 5.12).

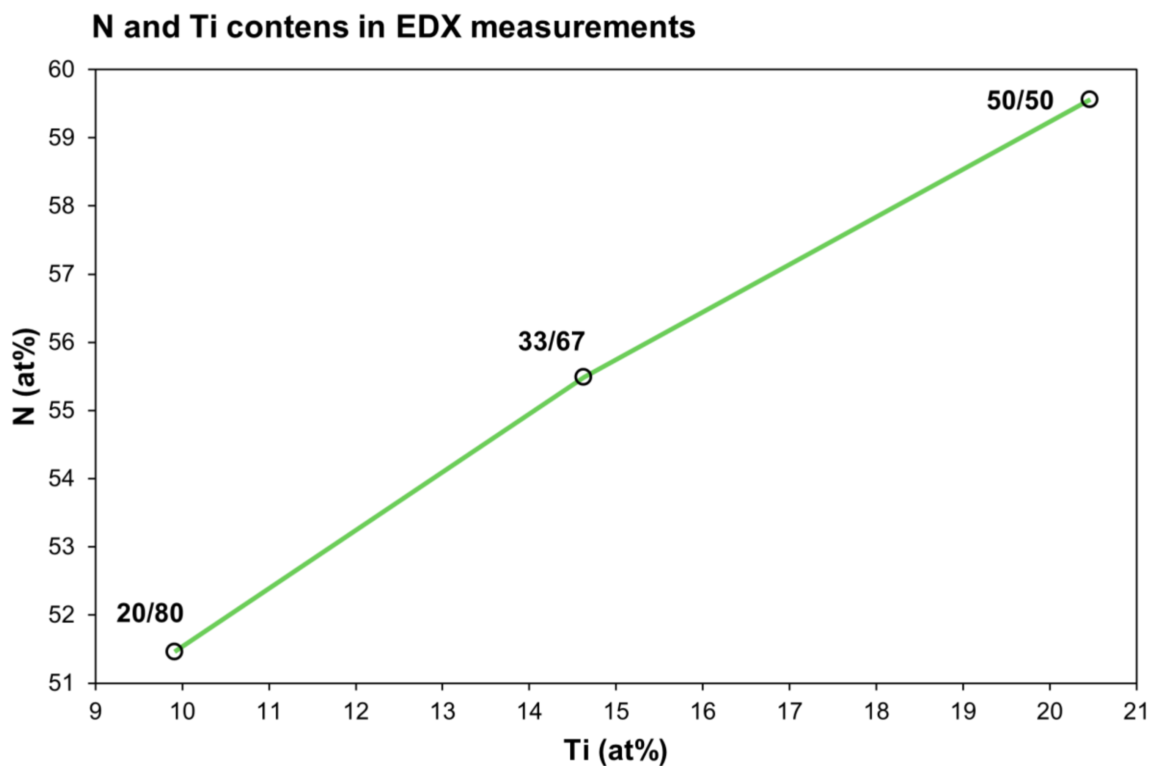

Figure 5.12. Relation between N and Ti contents in EDX measurements. It is clearly shown that the N concentration increases with increasing Ti content and is thus falsified. The data point labels refer to the Ti/Al ratio of the targets.

The obtained spectra can also show artefacts such as sum peaks, which appear if the signal processor receives signals so close together that it interprets them as one. This happens especially with high count rates and creates a second peak at the double energy of the parent peak or any other combination of element energies in the sample. [27] For aluminum (Al), for

Die approbierte gedruckte Originalversion dieser Diplomarbeit ist an der TU Wien Bibliothek verfügbar
The approved original version of this thesis is available in print at TU Wien Bibliothek.
TU Bibliothek WIEN Your knowledge hub

example, the second peak appears at approximately 3 keV (see Figure 5.13). Another artifact is the Si escape peak, which is created if an excited Si atom falls back to its ground state and releases the excess energy in the form of an Auger electron. This is inelastically scattered and either directly contributing to the signal generation or indirectly by exiting further atoms. However, some of the Auger electrons can also leave the Si crystal which reduces the energy of the parent peak by the energy they are carrying. This creates an additional peak at the new energy position. [26]

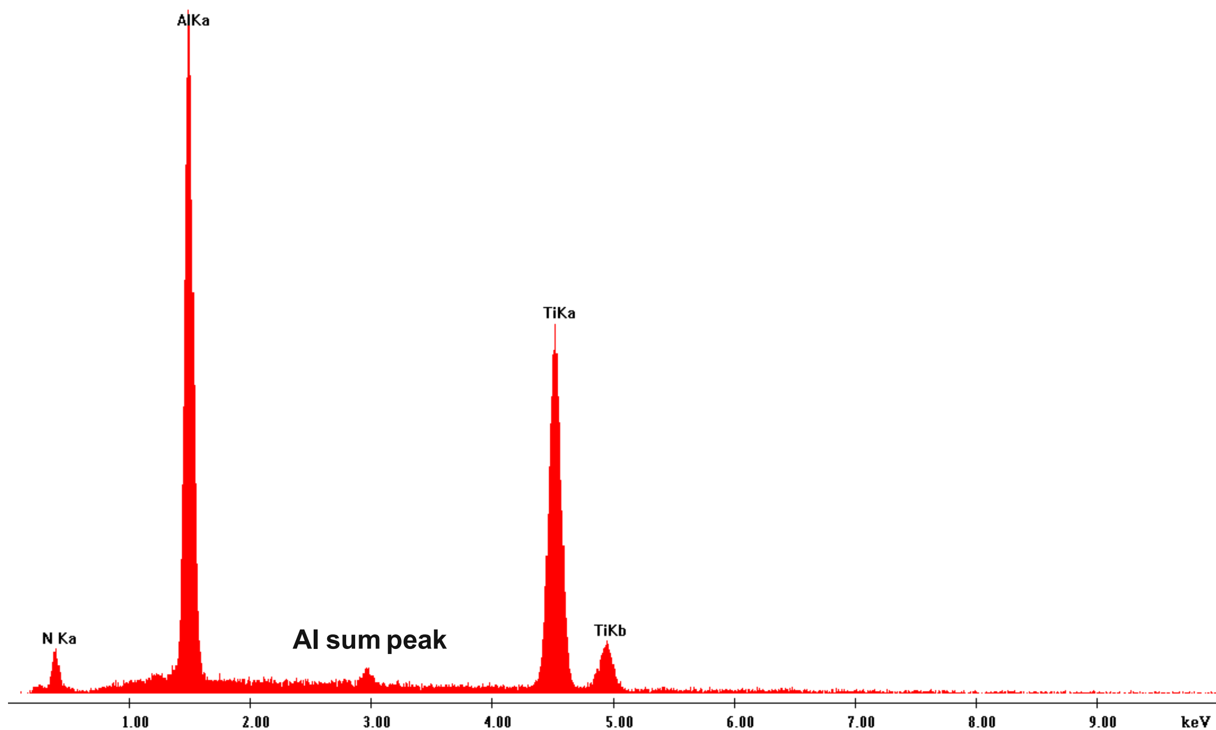

Figure 5.13. EDX spectrum of Ti-Al-N, showing K_{α} peaks of Ti, Al, and N and also the Ti K_{β} peak. At approximately 3 keV, the Al sum peak is indicated.

To assign the peaks of the obtained spectrum to individual elements, certain software is used. Subsequently, a quantitative analysis can be performed, for which the software determines the intensity of each peak in a fitting process. The intensity is proportional to the concentration of the element in the sample, but it is also influenced by any other element through the ZAFc matrix effects: [26]

- Z – atomic number matrix effect: the electron scattering is influenced by other atoms
- A – absorption matrix effect: the X-ray photons are absorbed by the sample
- F – secondary fluorescence matrix effect: the sample absorbs characteristic X-rays and emits them again
- c – secondary fluorescence matrix effect: like the F effect, but with bremsstrahlung

Die approbierte gedruckte Originalversion dieser Diplomarbeit ist an der TU Wien Bibliothek verfügbar
The approved original version of this thesis is available in print at TU Wien Bibliothek.
TU Bibliothek WIEN Your knowledge hub

Each of these effects is algorithmically corrected during the quantification process. The measured intensities are then related to a standard with known concentrations, which contains the same elements and was measured at the same device, maybe also during the same session. Besides this so-called k-ratio protocol, it is also possible to compare the spectrum to spectra from libraries measured with different parameters. Through interpolation or extrapolation, the comparison spectrum can be adjusted to the parameters used during the experiment so that it can be used as a standard (but the method is still called standardless quantification). [26]

It is also possible to visualize the concentrations of individual elements in the form of line scans or mappings. For this purpose, an EDX spectrum is collected for every pixel and the intensity is converted into a gray scale. The brighter the pixel, the higher is the concentration of the element. [26]

The samples of this thesis were examined with an EDAX system (SUTW-Sapphire detector) attached to the SEM *FEI Philips XL 30* with the following parameters in Table 5.3:

Table 5.3. Parameters for EDX analysis

Parameter	Value
Electron high tension	15 kV
Resolution	130 eV
Count rate	~ 3000 counts per second
Measuring time	20 s
Amplifier time	35 µs
Death time	< 35 %
Take off angle	34.94°

Since the quantification of N is problematic in samples with N and Ti, only Ti and Al were standardless quantified first. For comparison, also with other analysis methods, they were then quantified again with N. Furthermore, to not falsify the Al content with Al from the substrate, only thin films on austenitic substrates were examined.

Die approbierte gedruckte Originalversion dieser Diplomarbeit ist an der TU Wien Bibliothek verfügbar
The approved original version of this thesis is available in print at TU Wien Bibliothek.
TU Bibliothek WIEN Your knowledge hub

5.3.4 Electron Energy Loss Spectroscopy – EELS

Compared with EDX, EELS is more sensitive and can also distinguish elements with atomic numbers below 10. It is a method for chemical analysis, which can be only used in a (S)TEM where the detector is positioned underneath the sample. This detector collects low-angle scattered (< 1°) or not scattered electrons, which are then sorted by a magnetic prism according to their kinetic energy. To assure that no sample drift occurred during the analysis, it is recommended to take images before and after the analysis. It is possible to examine spots or to do mapping (only for STEM). The obtained spectrum is similar to the EDX spectrum, but the electrons per channel are plotted against the energy loss in electron volt. The energy loss occurs during the inelastic interaction between incident electrons and the sample. It is the difference between the energy of the electrons before the interaction and the kinetic energy of the electrons after the interaction, the latter being measured by the detector. The obtained EELS spectrum can be divided into three different zones: [30]

1. Zero loss peak: It is built up by electrons which do not experience any scattering or are elastically scattered. It occurs at 0 eV with a width of a few electron volts.
2. Low loss region: Peaks in the region below 100 eV have undergone inelastic scattering at outer-shell electrons of the specimen, leading to their ionization. From the shape of these ionization edges, the element can be identified, but also bonding and valence states of the excited atom can be determined. The region also shows at lower electron volt values a plasmon resonance peak.
3. High loss region: If the sample atoms are excited at inner shells, the resulting peaks appear at higher energies. Like the low-loss peaks, these peaks can be used to identify elements in the sample and to determine bonding and valence states.

It is also possible to use EELS for quantification. Before that, the background must be corrected or removed during a fitting process. [30]

For this thesis, a *TECNAI F20* (S)TEM was used to determine the ratio of Ti, Al and N with EELS of chosen samples which showed good mechanical properties or interesting diffractograms. The device has an extreme field emission gun and was performed with 200 kV and a *Gatan GIF Tridiem* image filter system.

Die approbierte gedruckte Originalversion dieser Diplomarbeit ist an der TU Wien Bibliothek verfügbar
The approved original version of this thesis is available in print at TU Wien Bibliothek.
TU Bibliothek Your knowledge hub WIEN

5.4 Elastic Recoil Detection Analysis – ERDA

Another method to determine the chemical composition of thin films is ERDA. In comparison to the previously mentioned techniques, it allows for depth-resolved analysis, but its implementation is much more complex and expensive. In principle, a sample is bombarded with high energy ions (MeV range) which eject sample atoms in the forward direction (they are recoiled) and are also scattered in the process. Both scattered ions and recoiled atoms have overlapping energy spectra and are simultaneously detected, which emerges the great difficulty of ERDA: The evaluation is intricate as only energies of recoiled atoms are of interest and additional information about the sample as well as a good software program are needed to obtain useful data. However, the energy of the individual species must be determined first and for this purpose, there are two general methods: First, the (ΔE – E) technique which differentiates particles with the same energy E by means of their energy loss (ΔE) while they pass through a thin layer of solid or gas in front of the detector. This reveals their atomic numbers. Secondly, the particles with the same energy can be distinguished by the time they need to travel a certain distance (time-of-flight method). In most cases, there are two foils which are 0.5 to 1 m apart and the particles generate a signal at each foil if they pass through it. With this method the mass of the particles is obtained. [36]

The energy of either the scattered ions or the recoiled atoms mainly depend on the mass ratio of ions and atoms (M_{Ion} – mass of scattered ion; M_{Atom} – mass of recoiled atom). If $M_{Ion} = M_{Atom}$, the atoms reach the highest possible energy, whereas the largest energy for ions is found if $M_{Ion} < M_{Atom}$. The most information can be obtained, if all atoms of the sample have a mass less than the ions ($M_{Ion} > M_{Atom}$), since this means that atoms with the highest mass of the sample will show the highest recoil energy. [36]

As stated previously, ERDA is capable of producing depth profiles of the element concentrations. For a certain energy of recoiled atoms, the concentration is related to the intensity of recoiled atoms and the depth can be obtained directly from the energy as atoms from greater depths have lower energies. [36]

The samples examined with ERDA were part of a different study and the measurements were conducted by Daniel Primetzhofer and Eleni Ntemou from the Ion Physics Group/Department of Physics and Astronomy (Uppsala University, Sweden). This study is not part of the present thesis and thus will not be elaborated on further, but the ERDA results are discussed in Chapter 6.3.3.

Die approbierte gedruckte Originalversion dieser Diplomarbeit ist an der TU Wien Bibliothek verfügbar
The approved original version of this thesis is available in print at TU Wien Bibliothek.
TU Bibliothek WIEN Your knowledge hub

6 Results and Discussion

6.1 Deposition Rate

The deposition rate in micrometer per hour (*µm/h*) was calculated from the thickness of the thin film (which was obtained with the SEM) and the duration of the deposition process (see Figure 6.1). In general, the deposition rate is highest for the 50/50 target (maximum value: 6.53 µm/h) and the rate continuously decreases for the 50/50 target from DC mode processes to BPDC-50 to BPDC-250 mode processes (minimum value: 3.43 µm/h for BPDC-250). Both observations can be explained with the good electrical conductivity of the target as this allows more power to be applied. This leads to a high sputter rate and thus a high deposition rate. While the temperature shows similar influences on the deposition rate for the sputter modes BPDC-50 and BPDC-250 (declining rate with increasing temperature), the DC process shows an increasing rate with increasing temperature. This cannot be seen by any other combination of target and sputter mode. The former may be explained with increasing re-sputtering effects with increasing substrate temperature as the atoms have more energy, but for the latter, further investigations are necessary.

The deposition rate from the 33/67 target follows a similar trend with temperature as from the 50/50 target, except for the DC mode: Now the deposition rate decreases with increasing temperature for all sputter modes. Also, the deposition rate is lower in general and the differences between the individual sputter modes nearly disappear, which is due to the lower electrical conductivity of the 33/67 target. Still, the DC mode leads to the highest deposition rate (maximum value: 5.30 µm/h), but the lower conductivity results in a positive charge build-up on the target which reduces the sputter rate of the DC mode and the BPDC-50 mode. Only the BPDC-250 mode shows similar values to the 50/50 target (minimum value: 3.36 µm/h) due to its better neutralization of the charge build-up.

This effect can be seen even more pronounced for the 20/80 target, as its electrical conductivity is so low that DC mode results in the lowest deposition rate of the whole test series (minimum value: 1.27 µm/h) and the values of the BPDC-50 and BPDC-250 mode significantly exceed it (mean value: 2.81 µm/h).

Die approbierte gedruckte Originalversion dieser Diplomarbeit ist an der TU Wien Bibliothek verfügbar
The approved original version of this thesis is available in print at TU Wien Bibliothek.
TU WIEN Bibliothek Your knowledge hub

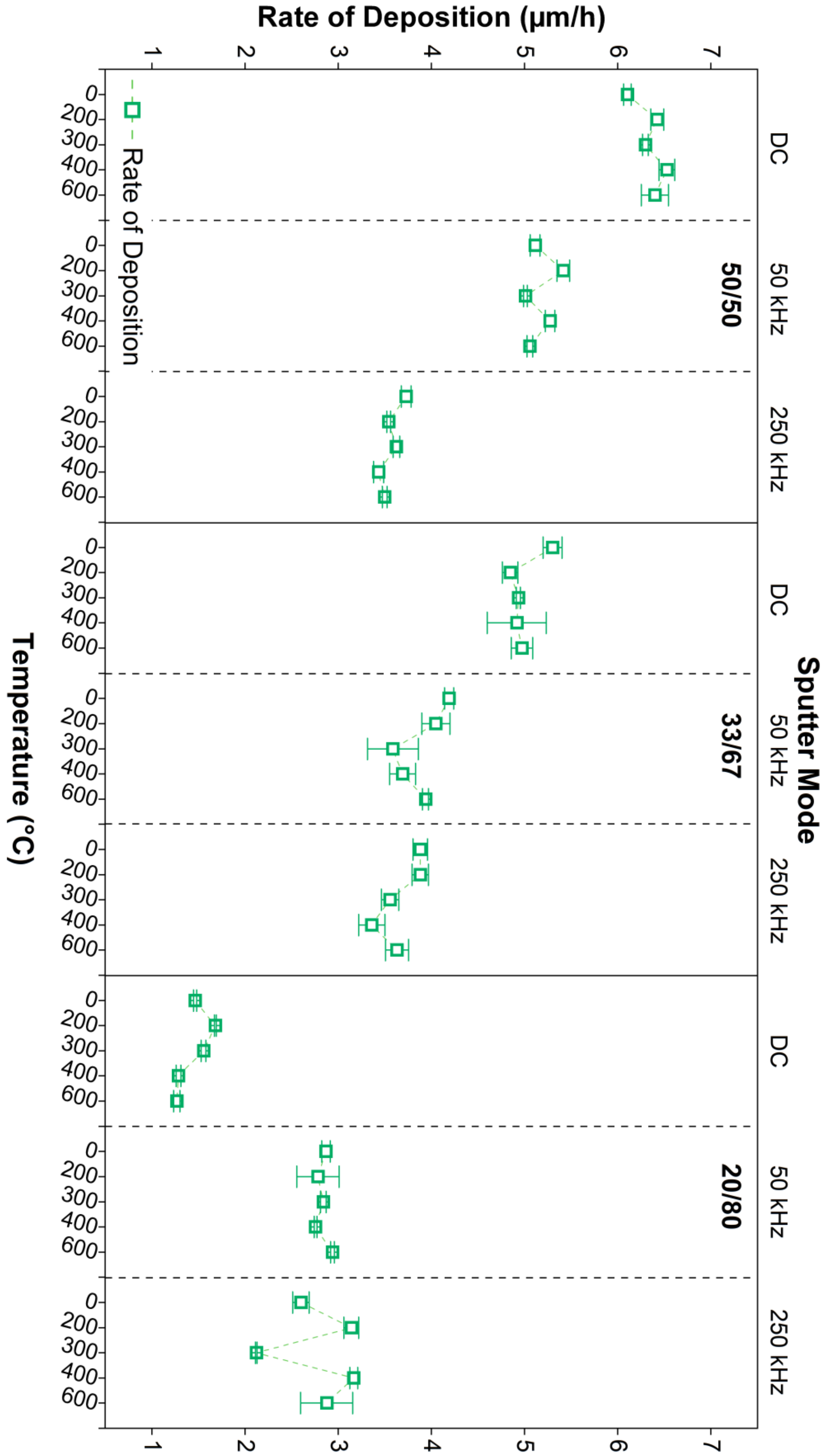

Figure 6.1. Rate of deposition in $\mu m/h$ of the three different targets varying with temperatures and sputter modes. 0 °C refers to no additional heating.

Die approbierte gedruckte Originalversion dieser Diplomarbeit ist an der TU Wien Bibliothek verfügbar
The approved original version of this thesis is available in print at TU Wien Bibliothek.
TU WIEN Bibliothek Your knowledge hub

6.2 Analysis of the Cross Section

The samples made from the 50/50 target (see Figure 6.2, Figure 6.3 and Figure 6.4) show a more or less pronounced formation of a columnar structure, which can already be seen in coatings without additional heating. At a substrate temperature of 600 °C and with DC and BPDC-50 modes (see Figure 6.2b and Figure 6.3b), the structure produced is still columnar, but finer and more compact. One explanation for this can be the occurrence of the hexagonal (Al,Ti)N phase in the cubic (Ti,Al)N phase (see diffractograms in Figure 6.21 and Figure 6.22). The individual phases interfere with the growth of the other phases which in turn inhibits the growth of straight, long columns. The effect appears not before 600 °C as the higher temperatures promote the formation of the hexagonal phase. No hexagonal phase can be seen in the diffractogram of thin films produced with the BPDC-250 mode (see Figure 6.23). In addition, more pronounced columns were formed at 600 °C (see Figure 6.4b). However, both the cross sections and the diffractograms of all samples from the 50/50 target show that the thin films are already crystalline in coatings with no or low temperature heating. This is the case since the good electrical conductivity of the target leads indirectly to a high mobility of the adatoms on the substrates. It should be also mentioned that the smaller thickness of the samples seen in Figure 6.2b and Figure 6.4b is because of a reduction of the deposition time from 60 to 30 minutes as the so produced thickness is already sufficient for the subsequent experiments.

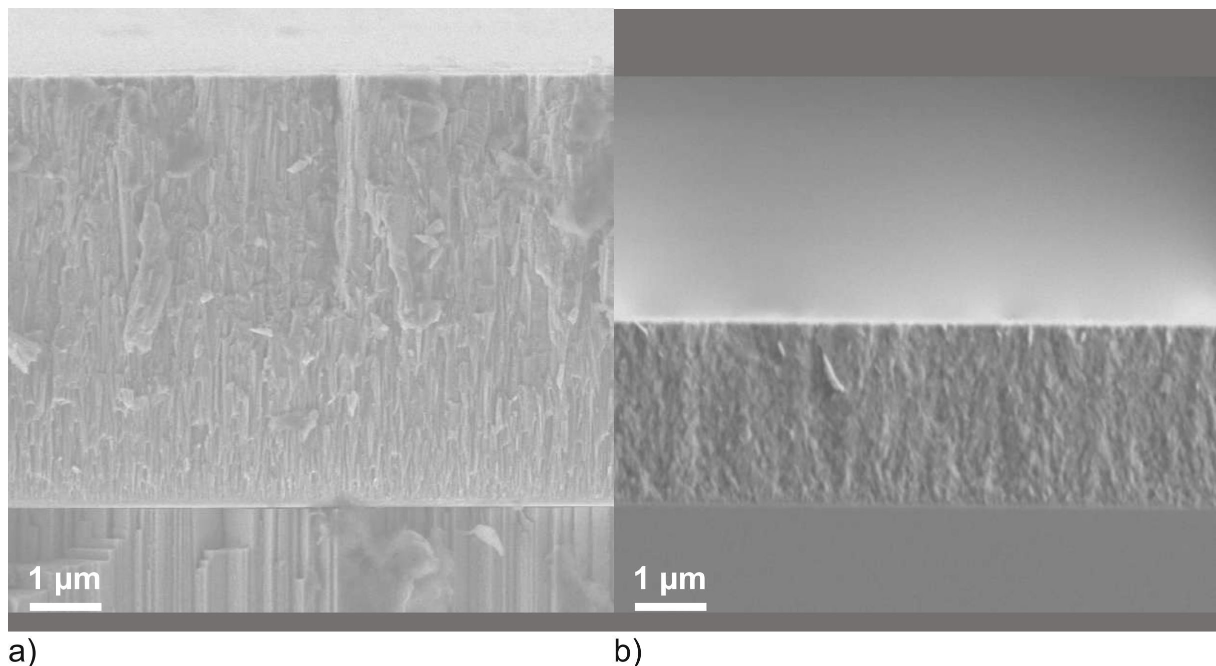

Figure 6.2. Cross section of the samples made from the 50/50 target with DC mode and **a)** no additional heating and **b)** at 600 °C substrate temperature.

Die approbierte gedruckte Originalversion dieser Diplomarbeit ist an der TU Wien Bibliothek verfügbar
The approved original version of this thesis is available in print at TU Wien Bibliothek.
TU Bibliothek WIEN Your knowledge hub

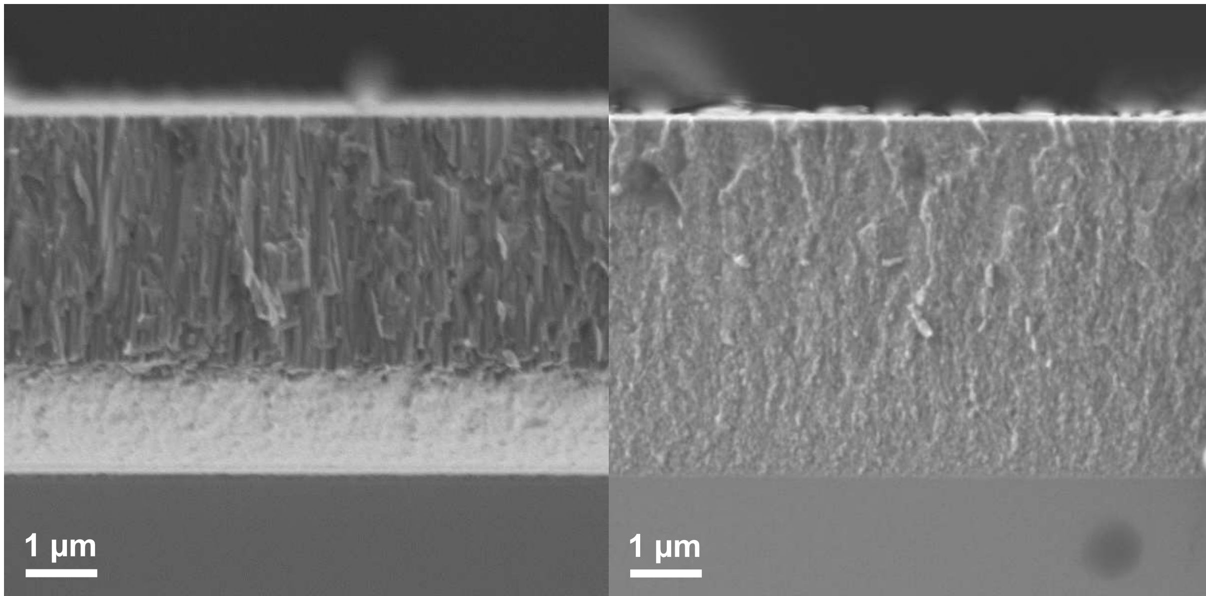

Figure 6.3. Cross section of the samples made from the 50/50 target with BPDC-50 mode and **a)** no additional heating and **b)** at 600 °C substrate temperature.

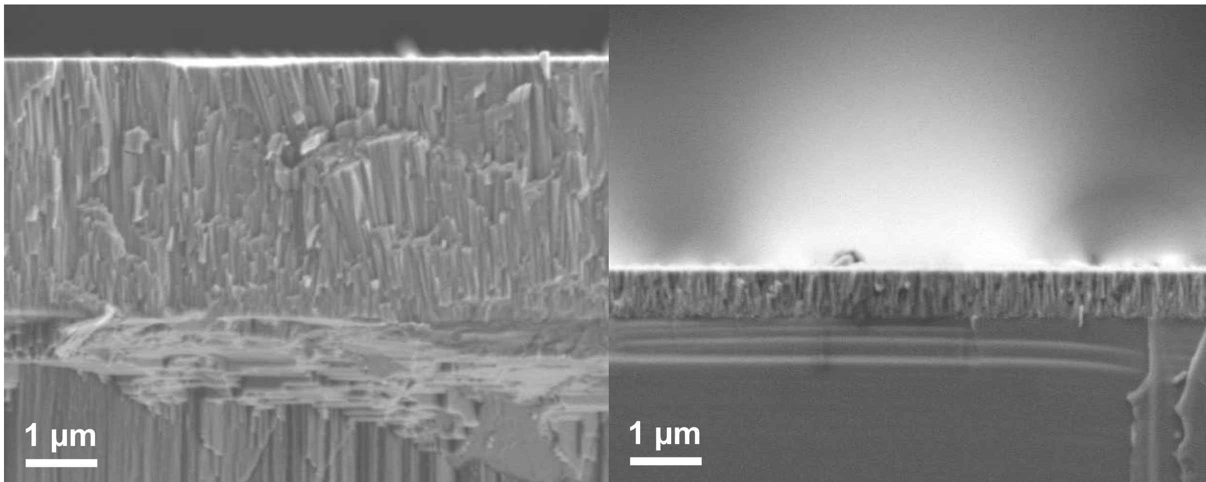

Figure 6.4. Cross section of the samples made from the 50/50 target with BPDC-250 mode and **a)** no additional heating and **b)** at 600 °C substrate temperature.

Die approbierte gedruckte Originalversion dieser Diplomarbeit ist an der TU Wien Bibliothek verfügbar
The approved original version of this thesis is available in print at TU Wien Bibliothek.
TU WIEN Bibliothek Your knowledge hub

In contrast to the 50/50 samples, the specimens made from the 33/67 target with DC and BPDC-50 modes and without additional heating show no pronounced structure in the cross section at a ten-thousand-fold magnification (see Figure 6.5a and Figure 6.6a). This may be because only very small or even nanocrystalline grains formed due to the lower electrical conductivity of the 33/67 target. This results in a scenario where the adatoms do not have enough energy from the sputtering process alone and the adatom mobility is too low to form large grains. If the temperature is increased, the energy is sufficient to promote the growth of larger grains, which can be seen for 600 °C in Figure 6.5b and Figure 6.6b. Especially the latter one shows columns, although both sputter modes led to coatings with a more compact and globular structure, similar to samples of the 50/50 target. Again, this speaks for the presence of a second phase. However, the cross section of samples produced with the BPDC-250 mode already shows a crystalline and columnar structure without additional heating (see Figure 6.7a). As before, the columns in coatings produced at 600 °C are smaller and the structure is more compact than in those produced at lower temperatures, indicating that a second phase is present (see Figure 6.7b).

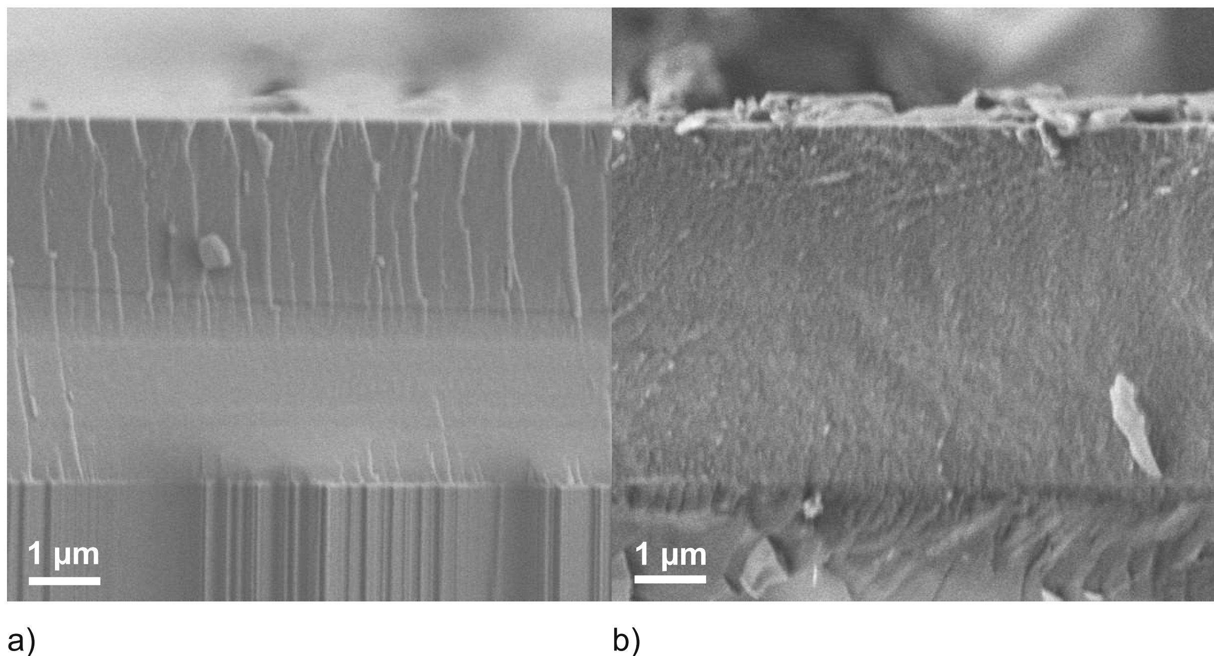

a) b)

Figure 6.5. Cross section of the samples made from the 33/67 target with DC mode and **a)** no additional heating and **b)** at 600 °C substrate temperature.

Die approbierte gedruckte Originalversion dieser Diplomarbeit ist an der TU Wien Bibliothek verfügbar
The approved original version of this thesis is available in print at TU Wien Bibliothek.
TU WIEN Bibliothek Your knowledge hub

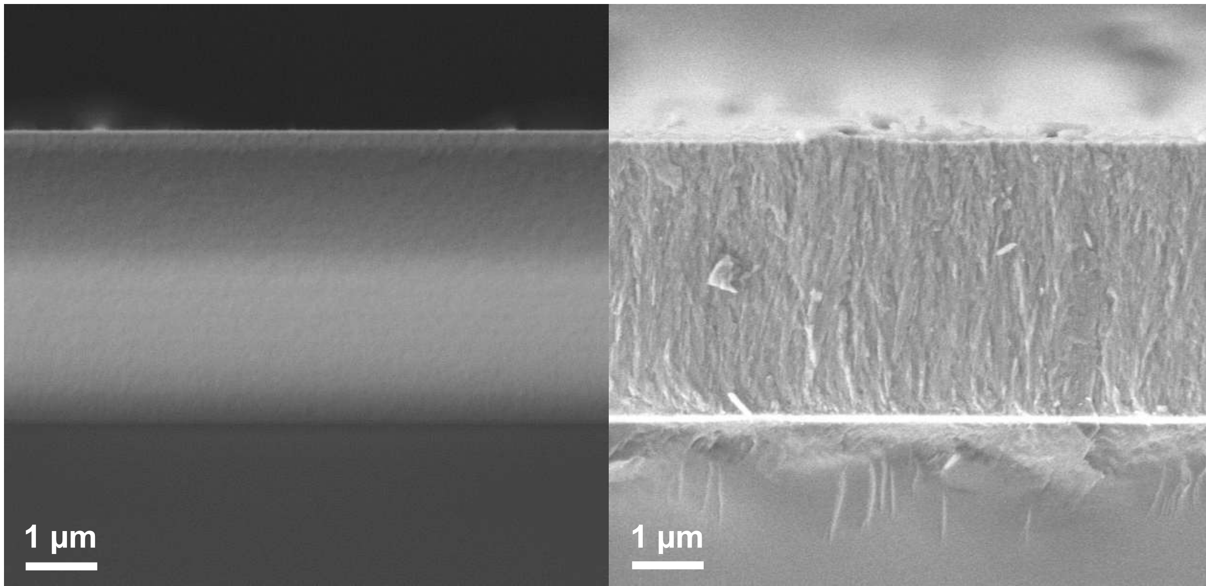

Figure 6.6. Cross section of the samples made from the 33/67 target with BPDC-50 mode and **a)** no additional heating and **b)** at 600 °C substrate temperature.

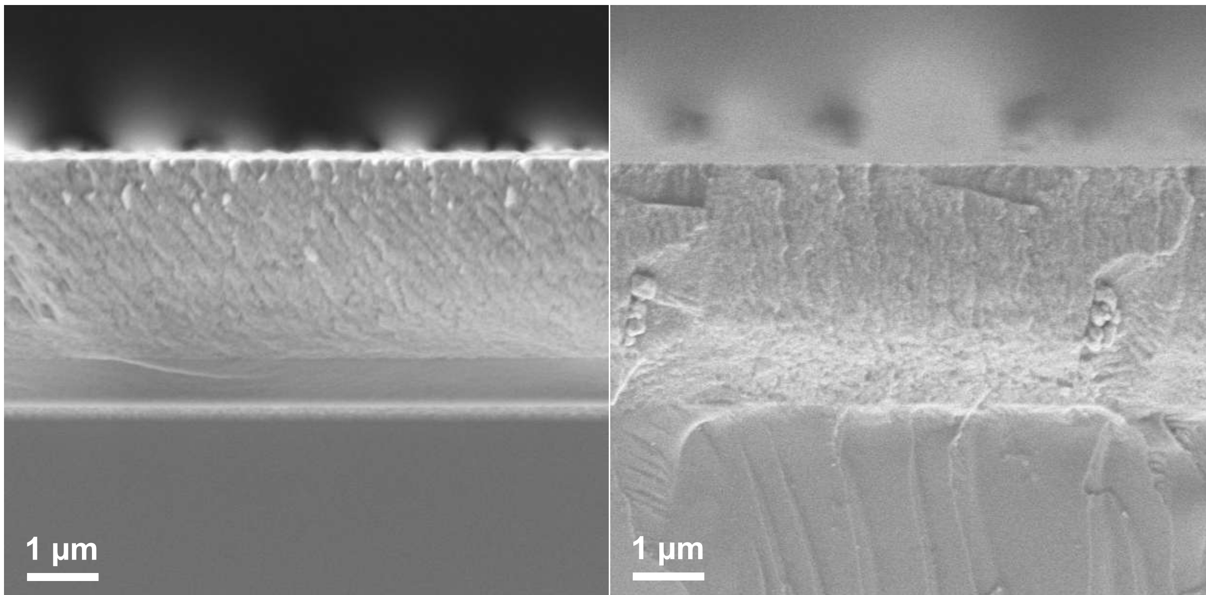

Figure 6.7. Cross section of the samples made from the 33/67 target with BPDC-250 mode and **a)** no additional heating and **b)** at 600 °C substrate temperature.

Die approbierte gedruckte Originalversion dieser Diplomarbeit ist an der TU Wien Bibliothek verfügbar
The approved original version of this thesis is available in print at TU Wien Bibliothek.
TU WIEN Bibliothek Your knowledge hub

The thin films produced with the 20/80 target generally show a more finely grained structure (see Figure 6.8, Figure 6.9 and Figure 6.10). Once again, the structure is not pronounced for DC and BPDC-50 modes without additional heating, but at 600 °C compact columns have formed (see Figure 6.8 and Figure 6.9). The BPDC-250 samples differ again from this trend as they already show a more crystalline morphology without additional heating and a less columnar structure for 600 °C (see Figure 6.10). This may be due to the formation of a second phase.

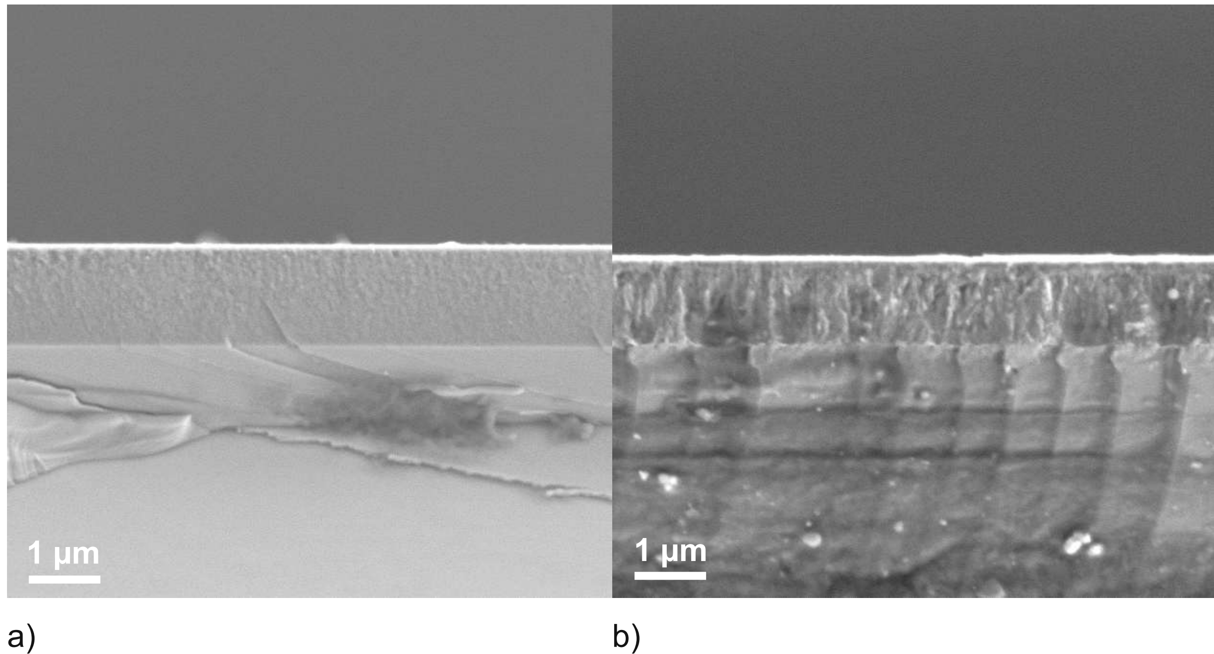

Figure 6.8. Cross section of the samples made from the 20/80 target with DC mode and **a)** no additional heating and **b)** at 600 °C substrate temperature.

Die approbierte gedruckte Originalversion dieser Diplomarbeit ist an der TU Wien Bibliothek verfügbar
The approved original version of this thesis is available in print at TU Wien Bibliothek.
TU WIEN Bibliothek Your knowledge hub

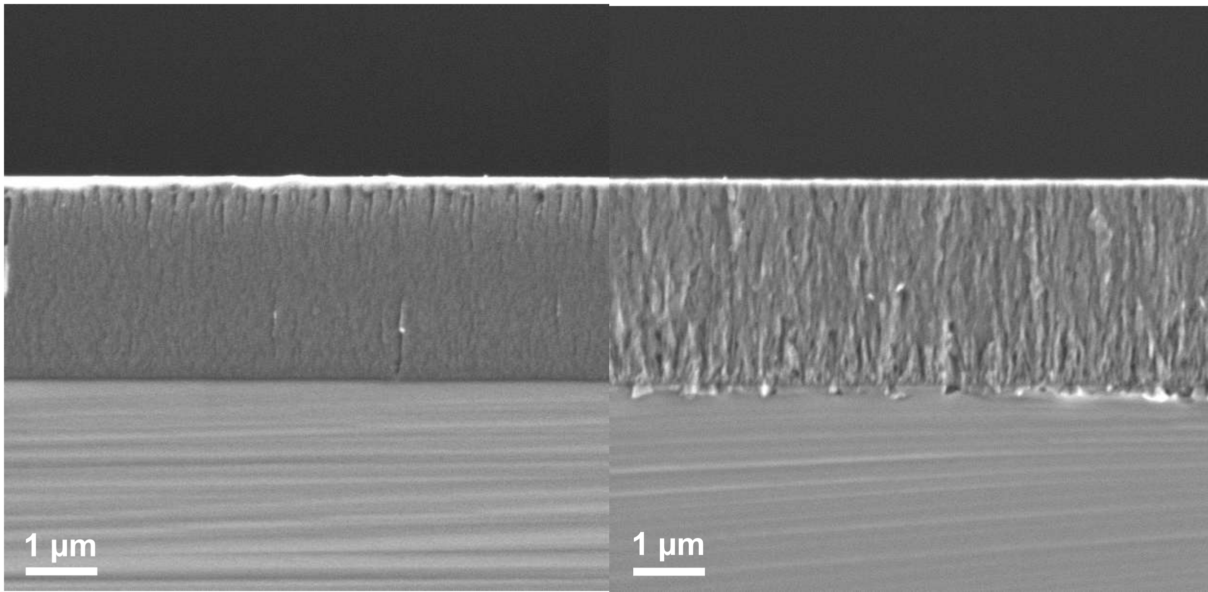

Figure 6.9. Cross section of the samples made from the 20/80 target with BPDC-50 mode and **a)** no additional heating and **b)** at 600 °C substrate temperature.

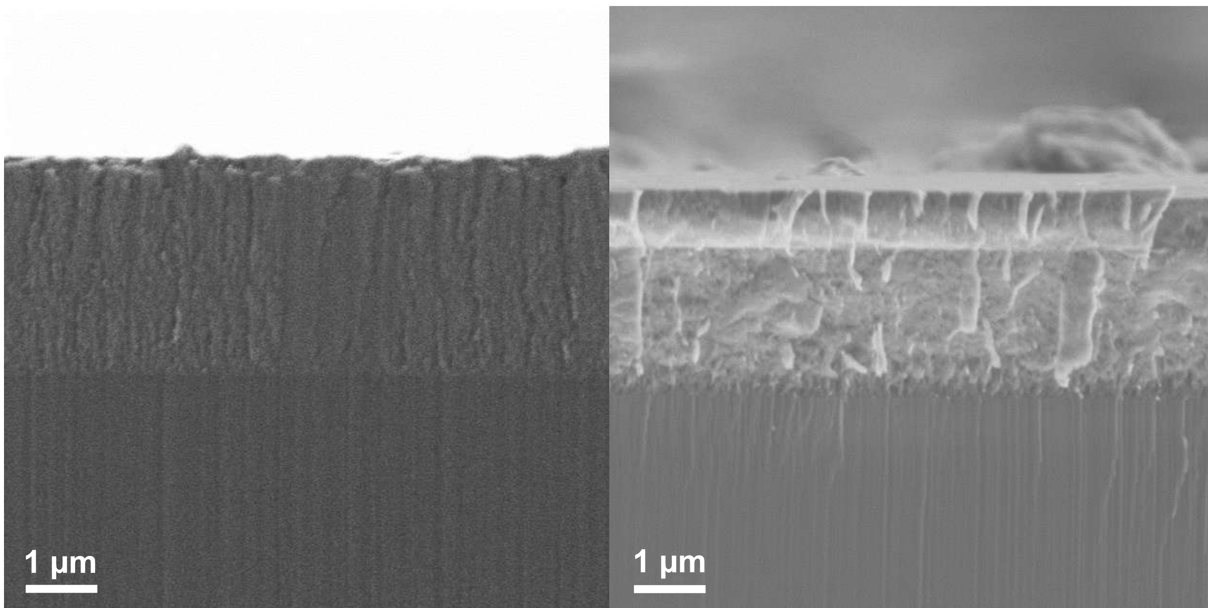

Figure 6.10. Cross section of the samples made from the 20/80 target with BPDC-250 mode and **a)** no additional heating and **b)** at 600 °C substrate temperature.

Die approbierte gedruckte Originalversion dieser Diplomarbeit ist an der TU Wien Bibliothek verfügbar
The approved original version of this thesis is available in print at TU Wien Bibliothek.
TU Bibliothek WIEN Your knowledge hub

Figure 6.11, Figure 6.12 and Figure 6.13 compare the cross section of samples produced from the same target at 600 °C in each case, but with different sputter modes. The biggest difference can be seen between the thin films produced with the 50/50 target (see Figure 6.11) and the 20/80 target (see Figure 6.13): Whereas DC and BPDC-50 modes led to the formation of a globular structure for the 50/50 target, meaning that at least a second phase was formed, the equivalents of the 20/80 target show a columnar structure and thus the thin film is single-phase. The opposite holds true for the BPDC-250 samples. The 33/67 coatings are more globular for the DC and the BPDC-250 mode and more columnar for the BPDC-50 mode.

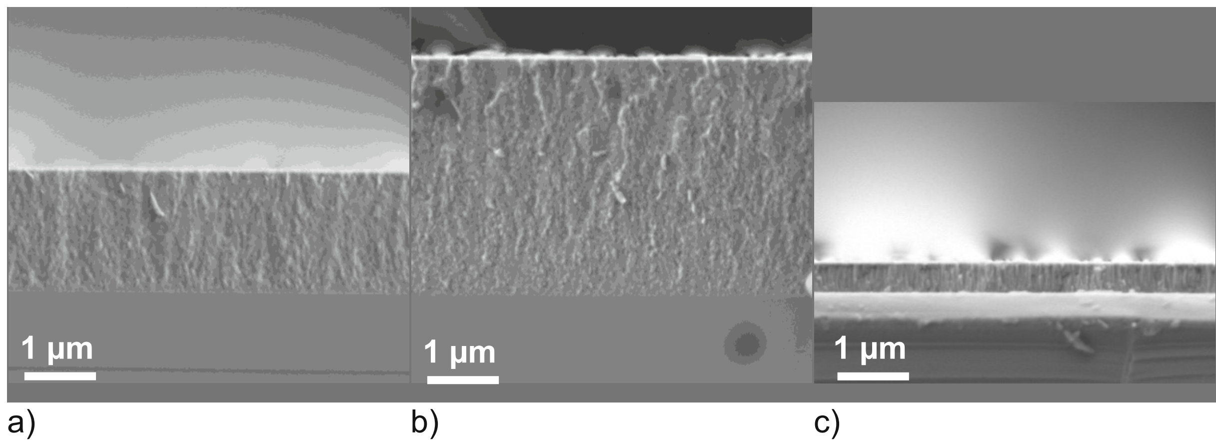

Figure 6.11. Cross section of the samples made from the 50/50 target at 600 °C with different sputter modes: **a)** DC, **b)** BPDC-50 and **c)** BPDC-250.

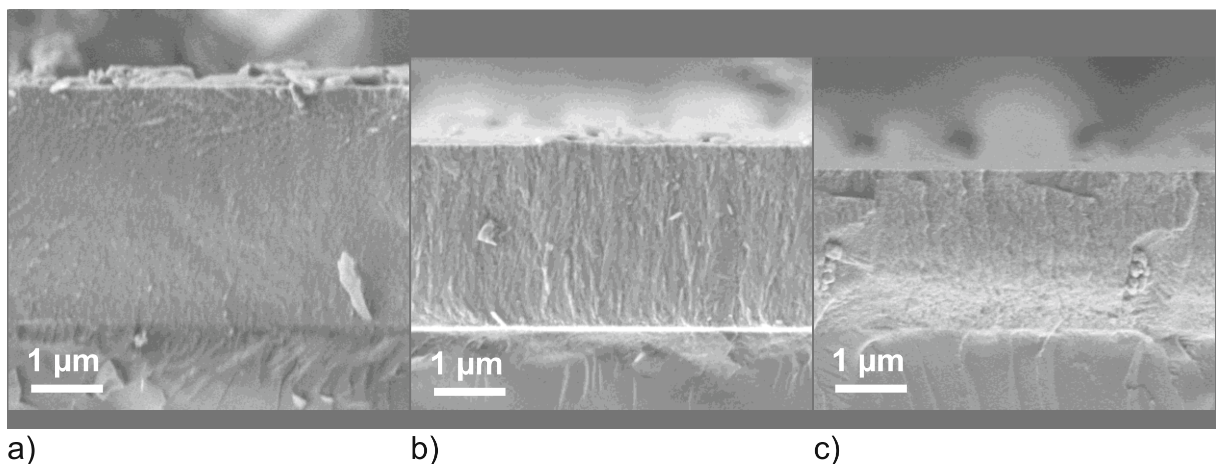

Figure 6.12. Cross section of the samples made from the 33/67 target at 600 °C with different sputter modes: **a)** DC, **b)** BPDC-50 and **c)** BPDC-250.

Die approbierte gedruckte Originalversion dieser Diplomarbeit ist an der TU Wien Bibliothek verfügbar
The approved original version of this thesis is available in print at TU Wien Bibliothek.
TU WIEN Bibliothek Your knowledge hub

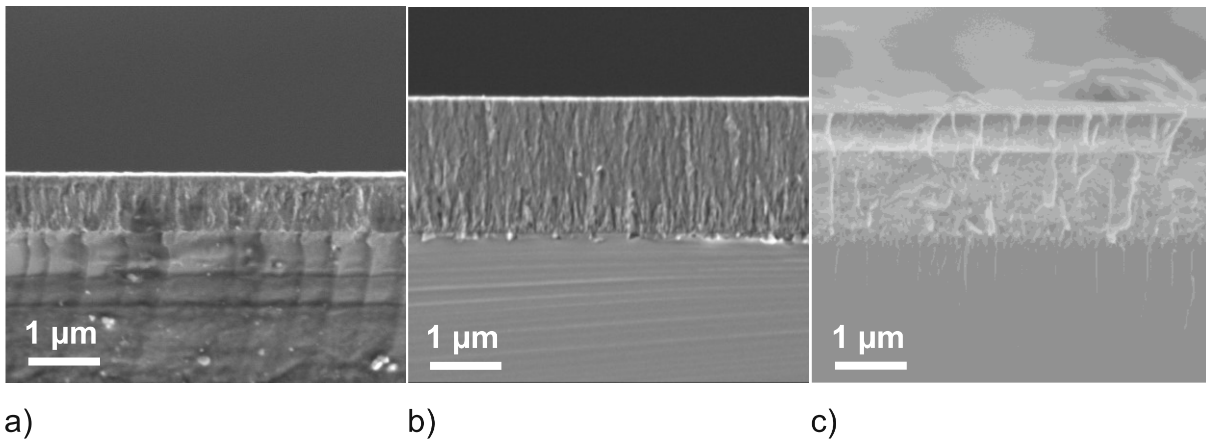

Figure 6.13. Cross section of the samples made from the 20/80 target at 600 °C with different sputter modes: **a)** DC, **b)** BPDC-50 and **c)** BPDC-250.

TU Bibliothek Your knowledge hub WIEN
Die approbierte gedruckte Originalversion dieser Diplomarbeit ist an der TU Wien Bibliothek verfügbar
The approved original version of this thesis is available in print at TU Wien Bibliothek.

6.3 Chemical Composition

6.3.1 EDX

As N and Ti cannot be accurately quantified together with EDX (as previously explained in Chapter 5.3.3), at first only the concentrations of Ti and Al were determined (see Figure 6.15). For every target, the sputter modes DC and BPDC-50 led to a thin film where Al is overstoichiometric (around 54 at%, 70 at% or 82 at%) and Ti understoichiometric (around 46 at%, 30 at% or 18 at%) compared to the concentrations of the targets. One reason for this could be the different angular distributions of the individual elements, which reflects in which directions the sputtered atoms are most likely to leave the target. For this, the angle is determined between the perpendicular of the substrate surface and the trajectory of the sputtered atom. It depends mainly on the atomic mass of the target atom, the binding energy of surface atoms and the kinetic energy that is transferred from the impinging argon ions. Taking these parameters into account, it is possible to determine in which direction most of the sputtered atoms are moving after they have left the target. For Al this is at an angle of 0° and for Ti at around 40° for pure Al or Ti targets respectively and for DC magnetron sputtering with argon ions (see Figure 6.14). [37] Although there might be differences when a Ti-Al-N target is sputtered, the trend is evident: More Al than Ti atoms can arrive on the substrates and thus the Al concentration is higher.

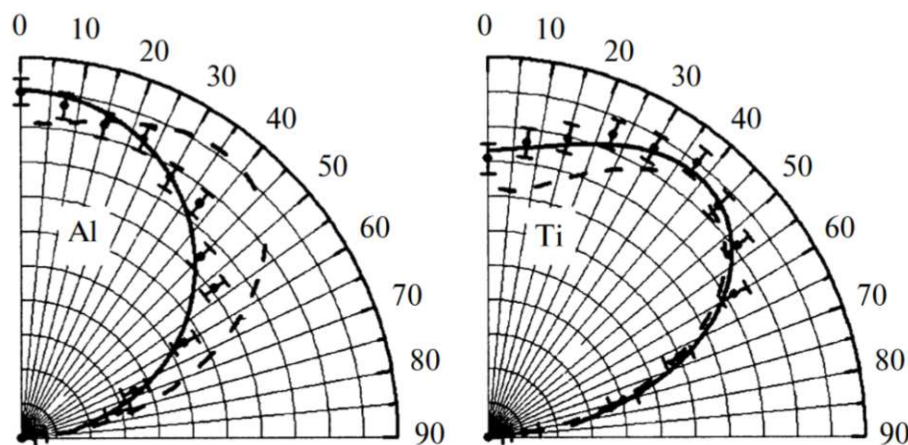

Figure 6.14. Angular distributions of sputtered atoms of the elements Al and Ti from pure Al and Ti targets respectively. The solid line represents the approximation of the experimental data (dots) and the dashed line is from a computer simulation (adapted from [37]).

Only with the BPDC-250 mode produced thin films are overstoichiometric in Ti (Ti: around 52 at%, 36 at% or 23 at%; Al: around 48 at%, 64 at% or 77 at%). There may be several reasons for this. One of them is the increased pressure of the process gas near the target because the

Die approbierte gedruckte Originalversion dieser Diplomarbeit ist an der TU Wien Bibliothek verfügbar
The approved original version of this thesis is available in print at TU Wien Bibliothek.
TU Bibliothek WIEN Your knowledge hub

pulse frequency is significantly elevated compared to the other modes. As Al is lighter than Ti, it might be deflected more easily by the process gas before it can reach the substrates. The high pulse frequency can also lead to higher ionization rates of the process gas, maybe even of the sputtered target atoms, due to accelerated electrons. Ions are attracted by the negative bias applied to the substrates, which can increase re-sputtering of atoms that already reached the substrates. Due to its lower mass, Al is also more easily re-sputtered, and the Al content decreases in the coating. Figure 6.15 also shows that the Ti concentration increases with rising substrate temperatures for the BPDC-250 mode. This can be explained with a combination of higher re-sputtering and evaporation rates of Al than of Ti since Al is lighter. Thin films generated with DC or BPDC-50 mode, on the contrary, show similar Ti and Al contents independently from the substrate temperature. This indicates that the evaporation and re-sputtering have a smaller influence on the concentration of samples produced using these two sputter modes.

For comparison, the quantification was again done for Ti, Al and N (see Figure 6.16). The concentration of N in the coatings is closest to the concentration of the respective target for the 20/80 target, where it varies around 50 at%. With increasing Ti content, the N concentration also increases and is significantly overstoichiometric, which is mainly due to the nature of the test method (see Chapter 5.3.3). The N content is hardly affected by variations of the Ti concentration within a sample set, but it varies with the amount of Al incorporated into the thin films. For example, this can be observed for the 33/67-BPDC-250 coating: While the Ti concentration stays almost the same, the N concentration increases by around 5 at%, whereas the Al concentration decreases by the same amount. With decreasing Ti content in the target, the Ti concentration of the samples approximates the target concentration and even exceeds it in some BPDC-250 coatings. The same is true for the Al content, except that Al of the BPDC-250 mode is always understoichiometric. While the Ti concentration shows no dependence on the temperature, the Al content decreases especially for thin films produced with the BPDC-250 mode with increasing temperature. Besides this, the Al concentration depends only slightly on the temperature. As N is not quantified right, both Ti and Al tend to be understoichiometric, except for the 20/80 target from which thin films were produced that are overstoichiometric in Al and understoichiometric in Ti for the DC and BPDC-50 modes. For BPDC-250 the opposite holds true.

Die approbierte gedruckte Originalversion dieser Diplomarbeit ist an der TU Wien Bibliothek verfügbar
The approved original version of this thesis is available in print at TU Wien Bibliothek.
TU WIEN Bibliothek Your knowledge hub

TU Bibliothek WIEN Your knowledge hub
Die approbierte gedruckte Originalversion dieser Diplomarbeit ist an der TU Wien Bibliothek verfügbar
The approved original version of this thesis is available in print at TU Wien Bibliothek.

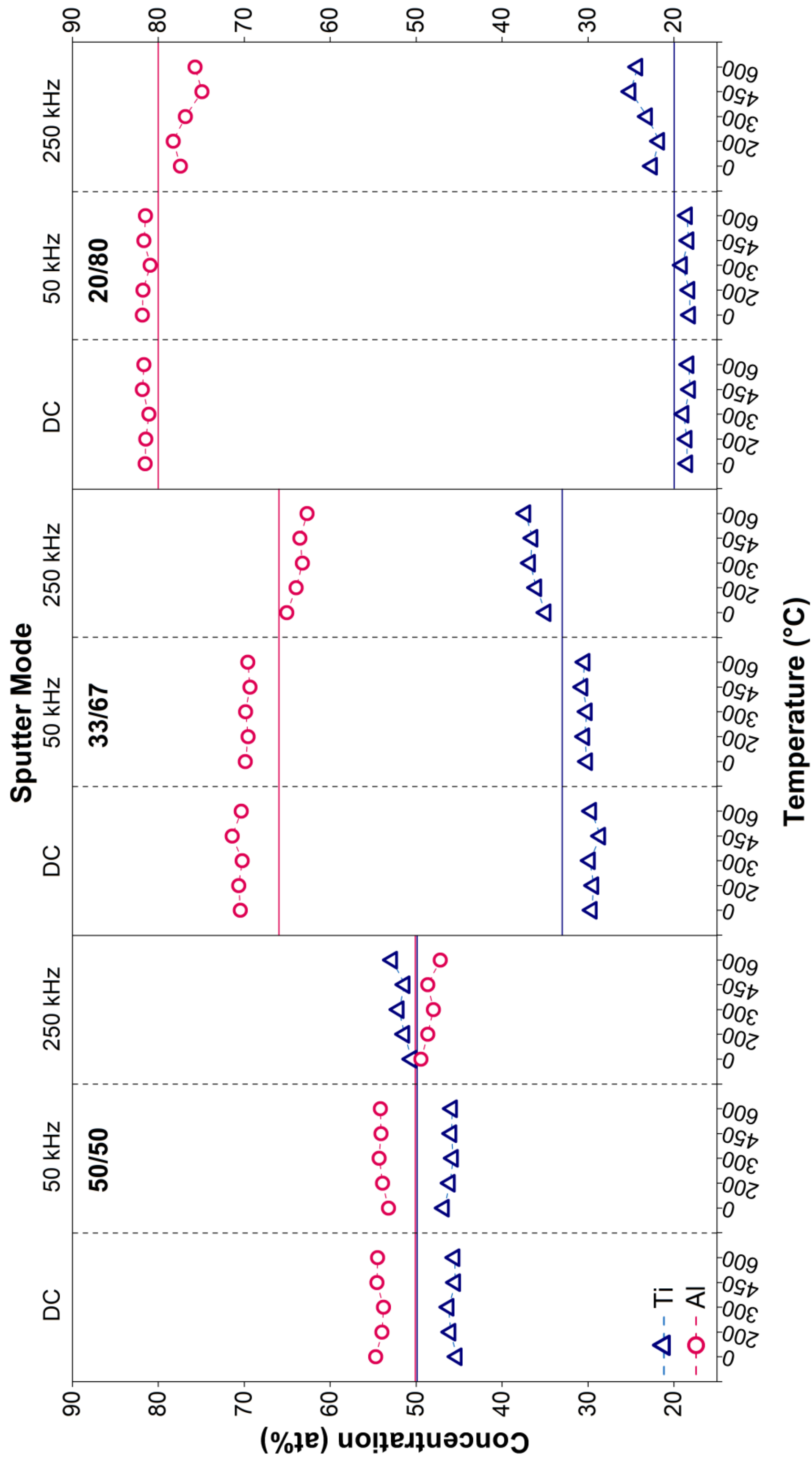

Figure 6.15. Concentration of Ti and Al in at% for the three different targets with varying temperatures and sputter modes, measured with EDX. The horizontal lines indicate the concentration levels of Ti and Al of the respective targets. 0 °C refers to no additional heating.

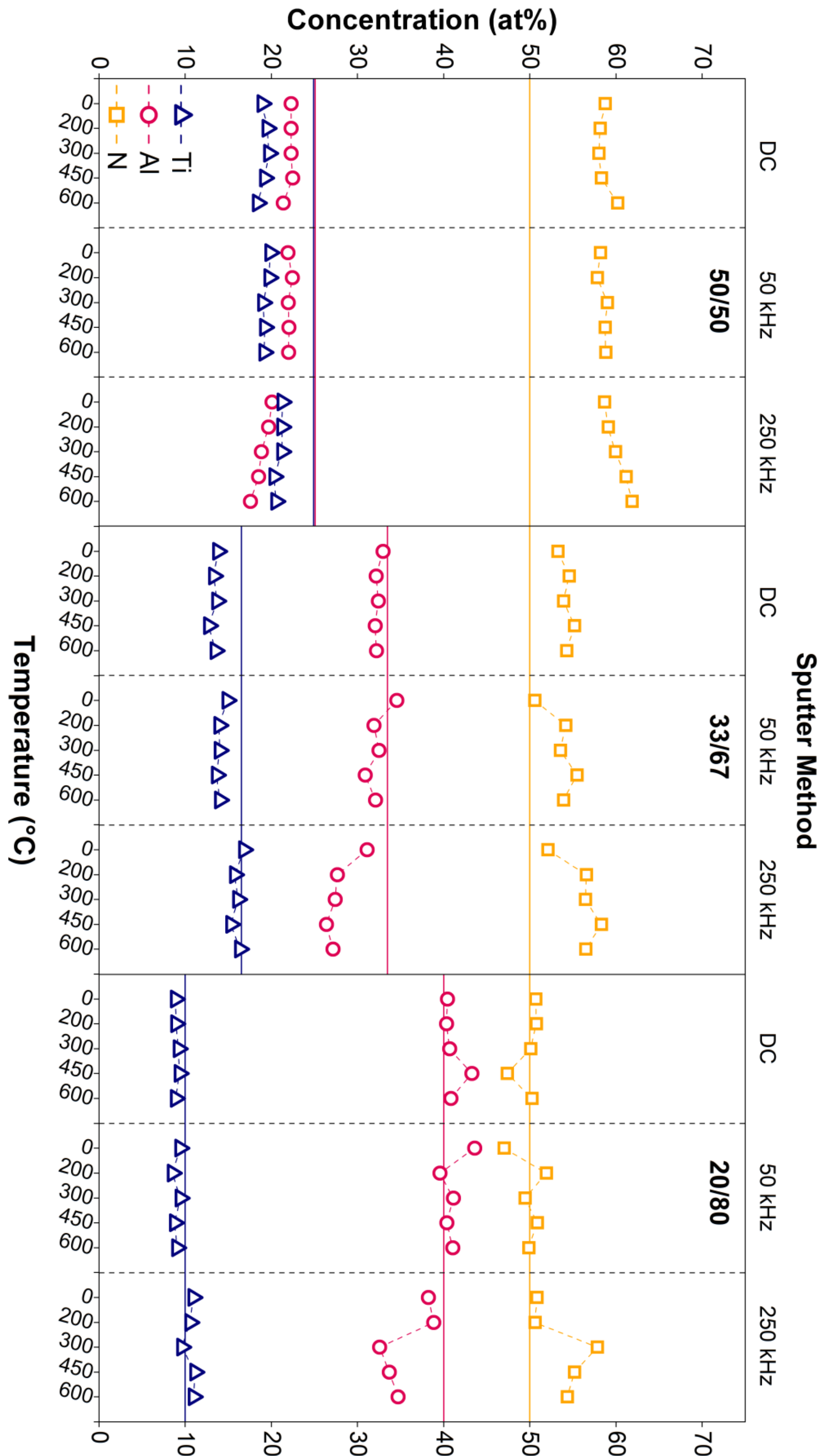

Figure 6.16. Concentration of Ti, Al and N in at% for the three different targets with varying temperatures and sputter modes, measured with EDX. The horizontal lines indicate the concentration levels of Ti, Al and N of the targets. 0 °C refers to no additional heating.

Die approbierte gedruckte Originalversion dieser Diplomarbeit ist an der TU Wien Bibliothek verfügbar
The approved original version of this thesis is available in print at TU Wien Bibliothek.
TU Bibliothek WIEN Your knowledge hub

6.3.2 EELS

Compared to the EDX measurements (see Chapter 6.3.1), the EELS experiments (see Figure 6.17) show different results: N is in all three samples understoichiometric with values of 38.80 at% (50/50 target), 39.61 at% (33/67 target) and 38.03 at% (20/80 target) instead of 50 at% as in the targets. Therefore, Ti (31.05 at%, 18.81 at%, 14.42 at%) as well as Al (30.15 at%, 41.58 at%, 47.55 at%) are overstoichiometric in all samples. The differences between the two test methods confirm the assumption, that EDX measurements strongly overestimate the N content. Moreover, the higher the Ti concentration in the coating, the higher the overestimation. The three EELS experiments, however, show that the N concentration hardly changes with changing target. It can also be seen that the lower proportion of N is mainly compensated by more Al atoms, while Ti remains closer to the target concentration. As mentioned in Chapter 6.3.1, Al atoms have a narrower angular distribution of the sputtered species compared to Ti atoms and thus reach the substrate more often. N may be understoichiometric because its atoms are the lightest ones in the present composition. Therefore, they are most easily deflected, and proportionally fewer N atoms can reach the substrates.

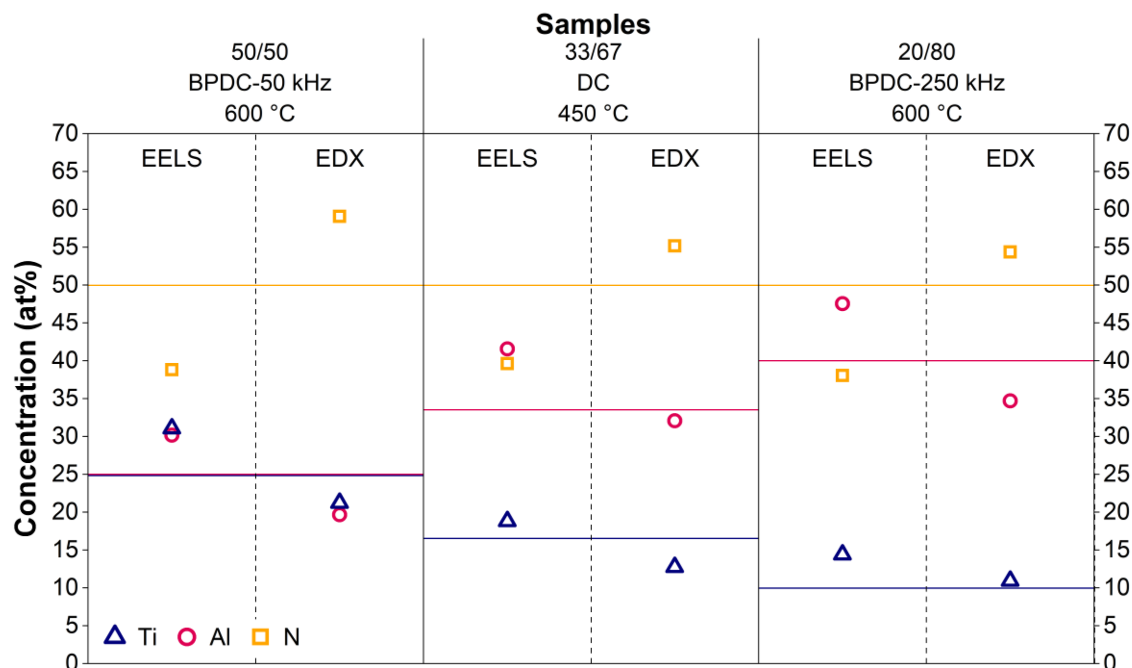

Figure 6.17. Concentration of Ti, Al and N in at% measured with EELS compared to the EDX results for specific samples. The horizontal lines indicate the concentration levels of Ti, Al and N of the respective targets.

Die approbierte gedruckte Originalversion dieser Diplomarbeit ist an der TU Wien Bibliothek verfügbar
The approved original version of this thesis is available in print at TU Wien Bibliothek.
TU WIEN Bibliothek Your knowledge hub

6.3.3 ERDA

Similarly to the EDX and different to the EELS results, ERDA measurements (Figure 6.18, Figure 6.19 and Figure 6.20) show that the highest N concentration can be found for the 50/50 target (45.39 at%) and the concentration decreases to 42.69 at% (33/67) and 39.74 at% (20/80). This may be because there is a stronger bond between Ti and N, allowing more N to be retained in the thin film if the Ti concentration is high in the coating. Despite all this, the N content is understoichiometric compared to the target concentration and is up to 13 at% lower than that of the EDX measurements. As mentioned in Chapter 6.3.2, this is probably because N atoms are most easily deflected by the Ar process gas and thus underrepresented in the coatings. In general, Al is overstoichiometric and Ti is either slightly understoichiometric or varies around the concentration of the target. Furthermore, only the Al content in the samples varies with the N content, relative to the target concentration, whereas Ti shows little to no variation. This could also be shown in the EDX and EELS experiments. Also noteworthy is the high oxygen (O) content of 1.91 at%, 1.68 at% and 1.63 at% on average, which is evident in all thin films measured. The oxygen concentration may already be high in the targets themselves, which is common for ceramic compound targets, and thus causes the high oxygen content in the coatings.

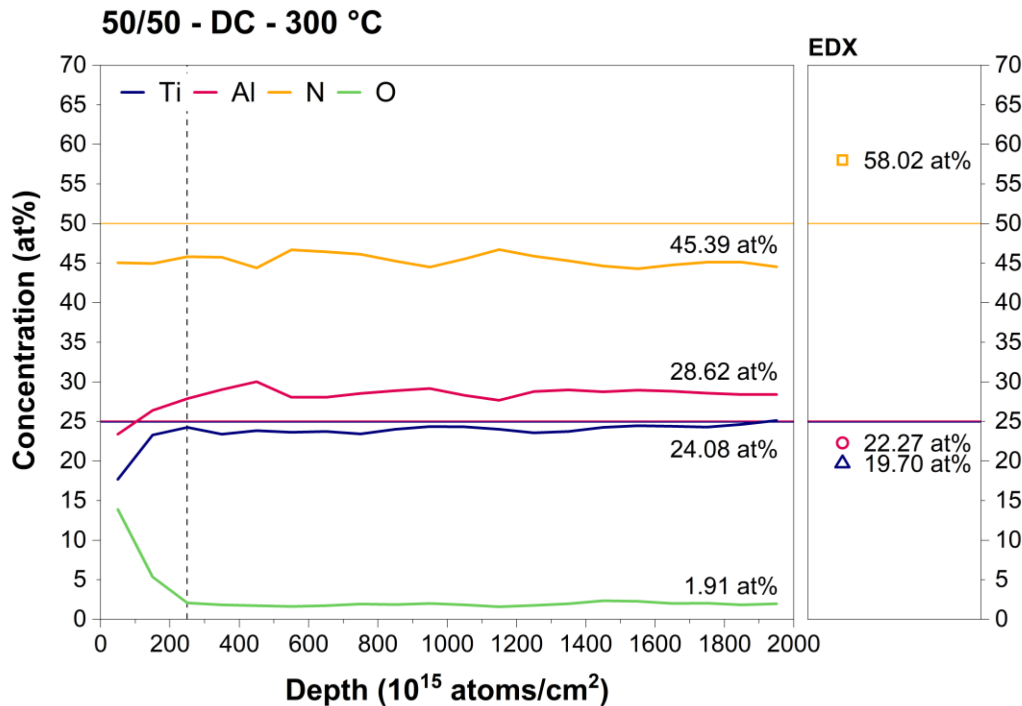

Figure 6.18. Concentration of Ti, Al, N and O in at% measured with ERDA and compared to EDX values (sample: 50/50 target, DC mode, 300 °C). The dashed line marks the transition from the oxidized region to the homogeneous coating material. The indicated values in at% are the mean concentration values of each element and the horizontal lines indicate the concentration levels of Ti, Al and N of the target.

Die approbierte gedruckte Originalversion dieser Diplomarbeit ist an der TU Wien Bibliothek verfügbar
The approved original version of this thesis is available in print at TU Wien Bibliothek.
TU WIEN Bibliothek Your knowledge hub

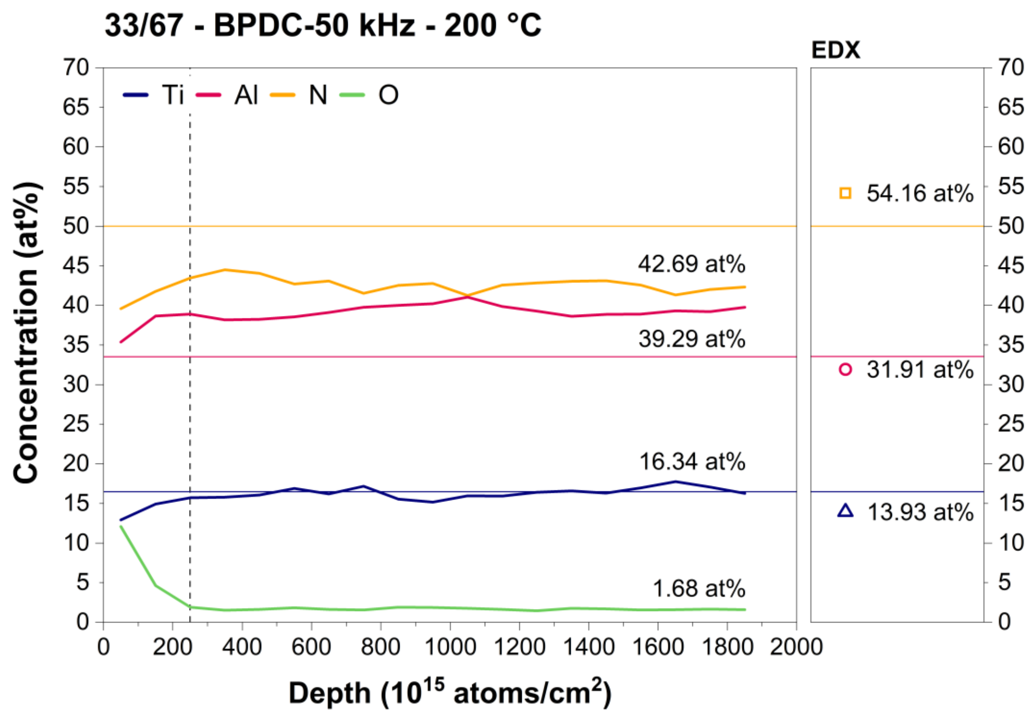

Figure 6.19. Concentration of Ti, Al, N and O in at% measured with ERDA and compared to EDX values (sample: 33/67 target, BPDC-50 mode, 200 °C). The dashed line marks the transition from the oxidized region to the homogeneous coating material. The indicated values in at% are the mean concentration values of each element and the horizontal lines indicate the concentration levels of Ti, Al and N of the target.

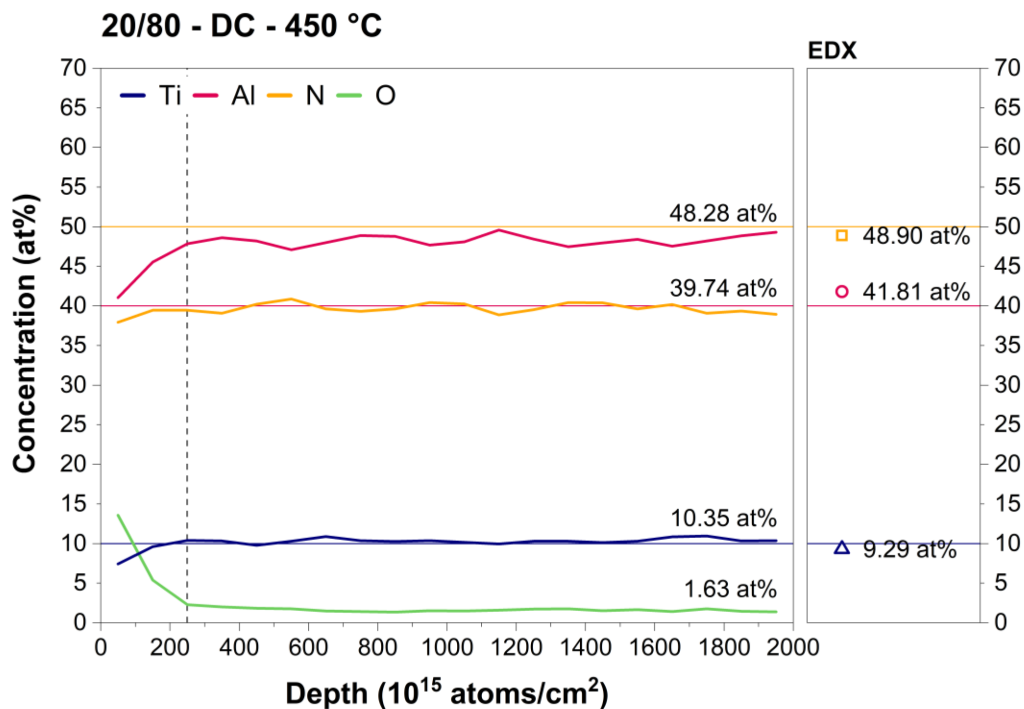

Figure 6.20. Concentration of Ti, Al, N and O in at% measured with ERDA and compared to EDX values (sample: 20/80 target, DC mode, 450 °C). The dashed line marks the transition from the oxidized region to the homogeneous coating material. The indicated values in at% are the mean concentration values of each element and the horizontal lines indicate the concentration levels of Ti, Al and N of the target.

Die approbierte gedruckte Originalversion dieser Diplomarbeit ist an der TU Wien Bibliothek verfügbar
The approved original version of this thesis is available in print at TU Wien Bibliothek.
TU Bibliothek WIEN Your knowledge hub

6.4 Crystallographic Properties

6.4.1 Crystal Structure – Diffractogram Analysis

The results of the XRD measurements show that coatings produced with the 50/50 target (see Figure 6.21, Figure 6.22 and Figure 6.23) have a primarily face-centered cubic (fcc) $Ti_{0.5}Al_{0.5}N$ crystal structure. This is not surprising as the concentration of AlN is still below the solubility limit of AlN in the TiN lattice, which allows the formation of the fcc structure. The coatings are already highly crystalline when produced without additional heating.

The DC sputter mode (see Figure 6.21) led to a preferred growth of (111) lattice planes in coatings without additional heating to ones deposited at 450 °C, and subsequently led to the appearance of the (222) peak. Which planes grow fastest and thus often appear as preferred planes in diffractograms, is determined by the surface energies and elastic moduli of the respective planes and by kinetic parameters. According to Riedl et al. [38], for Ti-Al-N coatings this plane would be (100) as it has the lowest surface energy compared to (110) and (111) and the smallest elastic modulus if the Al content is above a threshold value of 28 at%. Yet, if there is a sufficiently high oxygen content in the thin film, the (111) plane is preferred over the (100) one due to kinetic growth restrictions. The occurring oxygen concentration mentioned in the paper is 1.32 at%, which is clearly exceeded by the values measured with ERDA in this thesis (see Chapter 6.3.3). [38] It is therefore likely that this mechanism also occurs in the present coatings.

The deposition at 600 °C led to the occurrence of a hexagonal phase with (110) planes. However, it is assumed that the provided energy is not sufficient to actually precipitate pure AlN, but that the formation of a Al-rich (Al,Ti)N solid solution within the cubic one is possible. Through this process, the preferred lattice plane of the fcc-(Ti,Al)N matrix, now enriched in Ti, changes from (111) to (220) and thus the (222) peak also disappears. Since the appearance of a second phase in the coatings inevitably leads to the increase of the second-order stresses, the atoms arrange themselves in such a way that these stresses are minimized. The (220) and (110) orientations of the fcc-(Ti,Al)N and hexagonal (Al,Ti)N phases, respectively, appear to have the least difference in their lattice spacing and therefore, the (220) plane grows preferentially. However, the (Al,Ti)N content is only small compared to the amount of (Ti,Al)N and the precipitation resulted in a smaller grain size in comparison to the other thin films of this test series (recognizable by the larger peak width). Furthermore, as the (220) peak of (Ti,Al)N at 600 °C is not shifted with respect to its peak position in diffractograms of lower temperatures,

Die approbierte gedruckte Originalversion dieser Diplomarbeit ist an der TU Wien Bibliothek verfügbar
The approved original version of this thesis is available in print at TU Wien Bibliothek.
TU WIEN Bibliothek Your knowledge hub

one can conclude that the formation of the hexagonal phase does lead to only minor distortions of the crystal lattice.

Other observed growth planes of the cubic solid solution are (200) and (311). The intensity of both the (200) peak and the (311) peak initially becomes higher for samples produced at 200 °C, at the expense of the (220) plane, but decreases for higher temperatures. To mention it: The (200) peak of fcc-Ti-Al-N interferes with the (111) peak of fcc-iron and is sometimes hard to distinguish.

When compared to the substrate peaks and other diffractograms of this thesis, especially the (111) planes show a narrow peak width, indicating that the grain size is relatively large, and a highly crystalline material is present. This can be explained with the good transfer of energy to the adatoms due to the DC sputter mode and the high electrical conductivity of the target. The adatoms can move on the substrate until they find a preferable position on the crystal lattice and therefore can form large grains. The crystal lattice is slightly distorted (towards larger lattice spacings) compared to the reference due to various stresses in the coatings. The shift would have been also caused by a higher Ti content in the coatings, but the chemical analysis (see Chapter 6.3.1) contradicts this.

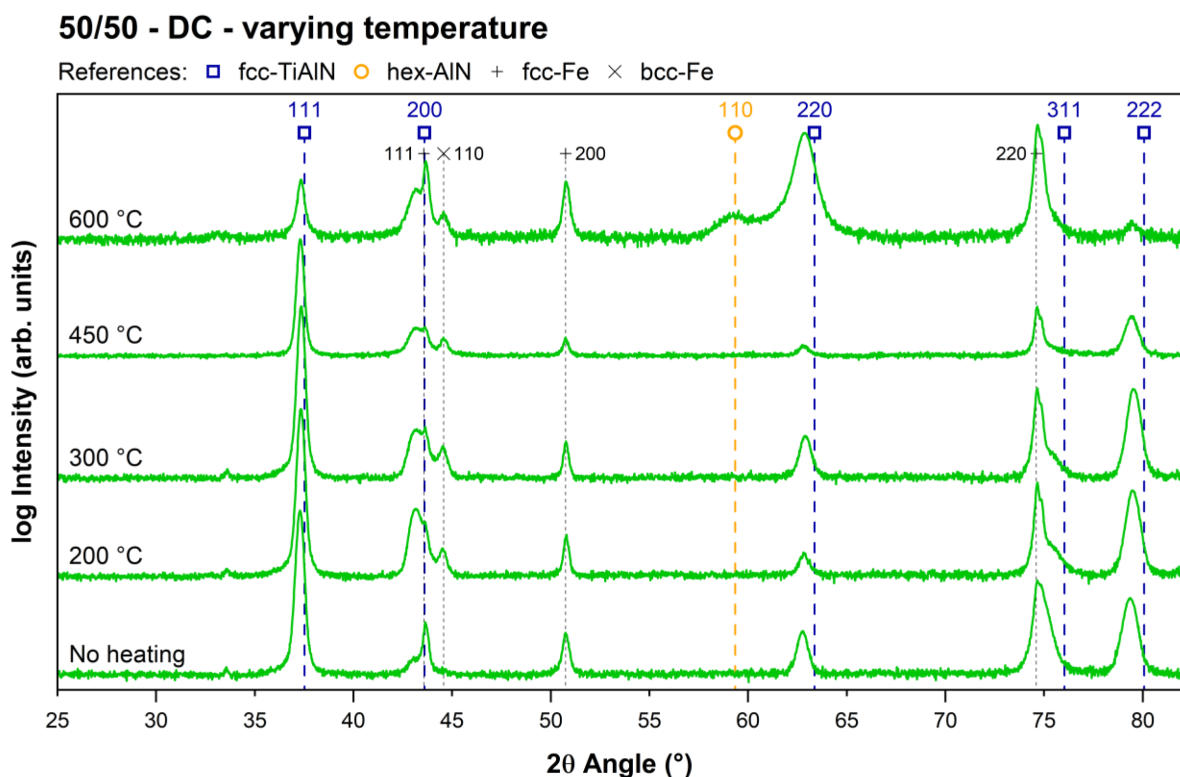

Figure 6.21. Diffractograms of samples made from the 50/50 target with the DC mode at varying substrate temperatures showing fcc-(Ti,Al)N and hexagonal (Al,Ti)N phases.

Die approbierte gedruckte Originalversion dieser Diplomarbeit ist an der TU Wien Bibliothek verfügbar
The approved original version of this thesis is available in print at TU Wien Bibliothek.
TU WIEN Bibliothek Your knowledge hub

Similar patterns can be seen for the BPDC-50 mode (see Figure 6.22). The only differences are that the (311) peak is missing and the (111) lattice plane is less preferred with rising temperatures in favor of the (220) plane. It can also be seen that the intensity of the (111) peaks is lower compared to the substrate peaks. However, the peak width is comparably narrow as in the DC mode samples and of the (220) planes even narrower, again indicating a highly crystalline material with large grains. Coatings deposited at 600 °C show an approximate uniform distribution of the (111) and (220) plane and a smaller amount of hexagonal (Al,Ti)N phase compared to the DC mode samples. The peak shifts and thus the distortion is similar to the DC mode specimens and again indicates stresses and not an increased proportion of Ti.

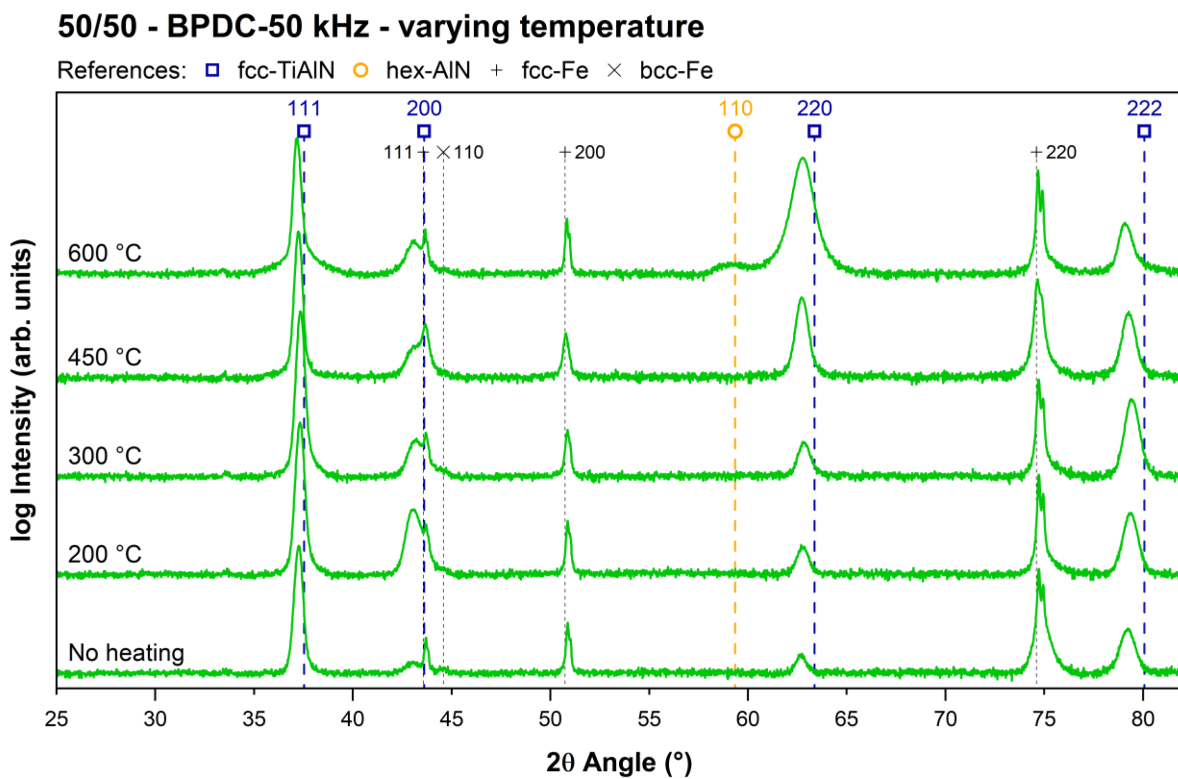

Figure 6.22. Diffractograms of samples made from the 50/50 target with the BPDC-50 mode at varying substrate temperatures showing fcc-(Ti,Al)N and hexagonal (Al,Ti)N phases.

Die approbierte gedruckte Originalversion dieser Diplomarbeit ist an der TU Wien Bibliothek verfügbar
The approved original version of this thesis is available in print at TU Wien Bibliothek.
TU WIEN Bibliothek Your knowledge hub

The peaks of the BPDC-250 mode diffractograms (see Figure 6.23) are broader than those of the other two sputter modes, leading to the conclusion that it produced finer grained coatings. The peak width increases with rising temperature, meaning that the thin films become more fine-grained, and the intensity of the coating peaks is lower regarding the substrate peaks and compared to the other sputter modes. As the temperature increases, the preferred plane changes from (111) to (220), only to change back to (111) in the 600 °C coatings (the (222) plane follows the (111) plane). The (200) plane is present, but with a comparatively lower amount, especially for low substrate temperatures. Although no separate hexagonal phase was formed, the (111) peaks of (Ti,Al)N show a small asymmetry that lies within the angular range of the (101) plane of AlN. On the one hand, asymmetric peaks can be explained with a high defect density, mainly stacking faults and twins, but on the other they could also be caused by an initiating spinodal decomposition of the fcc-Ti-Al-N phase. The lack of actual hexagonal Al-rich precipitates may be explained with the fact that Al is understoichiometric compared to the target concentration according to EDX measurements (see Chapter 6.3.1). In general, the microstresses in the coatings are high, recognizable by the strong deviation of the coating peaks from the reference, which lead to an increase in the lattice spacings. The high stresses and the finer-grained structure can be explained both with a high defect density. This is caused by the BPDC-250 mode itself by leading to a higher ionization rate of both the process gas and partially the target atoms. Due to the negative bias on the substrate, the ions are additionally accelerated towards the substrate and can transfer more energy to the adatoms. This in turn leads to a high defect density, which on the one hand causes strains in the lattice, but on the other hand also provides heterogeneous nucleation sites where grains can start to grow. Therefore, the general grain size is decreased.

Part of the left shift of the peaks might also have been caused by a higher Ti content in the coatings compared to the reference. According to the EDX measurements, Ti is overstoichiometric (see Chapter 6.3.1).

Die approbierte gedruckte Originalversion dieser Diplomarbeit ist an der TU Wien Bibliothek verfügbar
The approved original version of this thesis is available in print at TU Wien Bibliothek.
TU WIEN Bibliothek Your knowledge hub

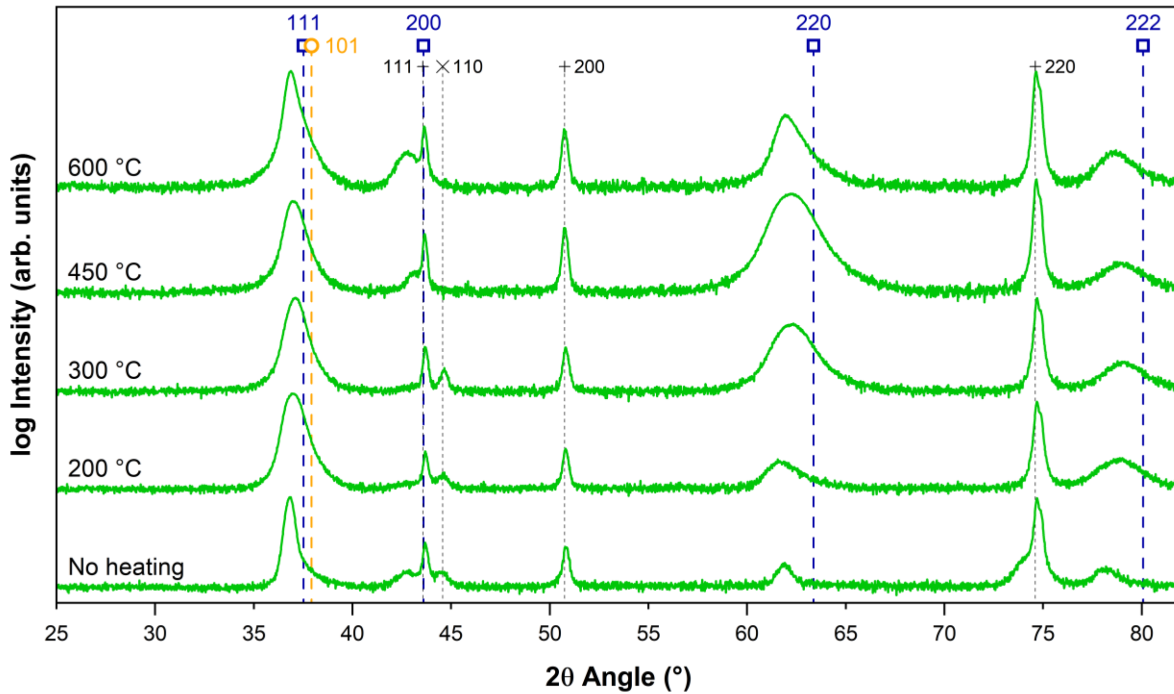

Figure 6.23. Diffractograms of samples made from the 50/50 target with the BPDC-250 mode at varying substrate temperatures showing fcc-(Ti,Al)N phases and perhaps initial precipitation of hexagonal (Al,Ti)N phases.

Die approbierte gedruckte Originalversion dieser Diplomarbeit ist an der TU Wien Bibliothek verfügbar
The approved original version of this thesis is available in print at TU Wien Bibliothek.
TU WIEN Bibliothek Your knowledge hub

In thin films produced from the 33/67 target (see Figure 6.24, Figure 6.25 and Figure 6.26), an Al-rich hexagonal form of Ti-Al-N is the main component, especially at low surface temperatures. Also here, the BPDC-250 mode is an exception. The concentration of AlN is now at the theoretical solubility limit of AlN in the cubic TiN lattice and the lattice tends to the hexagonal phase.

The DC mode (see Figure 6.24) resulted at the lower substrate temperatures (no heating and 200 °C) in coatings with a mixture of crystalline parts in (100) and (110) orientation and X-ray amorphous parts. The latter is probably a Ti-rich fcc-(Ti,Al)N phase, which leads to the conclusion that the main phase (hexagonal Al-rich (Al,Ti)N) hinders the growth of the minority phase, which then occurs only in nanometer-sized grains. Subsequently, the lattice of the hexagonal phase is hardly distorted compared to the reference. Again, it is assumed that the provided energy is not sufficient to actually precipitate pure TiN, but that the formation of a Ti-rich (Ti,Al)N solid solution within the cubic one is possible.

At or above 300 °C, the fcc-(Ti,Al)N phase was precipitated in mainly (220) orientation, but also some amount of (200) was detected. It formed larger grains which may be due to kinetic factors. As it can be seen for the 50/50 target, the growth of a second phase changes the preferred lattice planes of the main phase: from an approximately uniform distribution between (100) and (110) planes to almost only (110) planes. This might also be to reduce coherency strains and points out a general orientation relation between face-centered cubic and hexagonal Ti-Al-N phases. Contrary to the coatings of the 50/50 target, the distortion and stresses of the lattice increase significantly with rising temperature and increasing (Ti,Al)N content. The reason for this is on the one hand that the lattice spacing of (Ti,Al)N is smaller than that of the hexagonal phase. On the other hand, the strong right shift of the (110) peak can be also explained with the fact that pure hexagonal AlN has a smaller lattice spacing than (Al,Ti)N phases. The precipitation of a Ti-rich cubic phase leads to a hexagonal phase which is richer in Al and subsequently to the right shift of the peak. In the coatings produced at 600 °C, the (103) peak of hexagonal (Al,Ti)N may also appear.

Since the hexagonal (Al,Ti)N has narrower peaks and a higher peak intensity, it can be deduced that it has formed larger grains than the cubic phase. This may also be because the majority phase hinders the growth of the minority phase.

TU WIEN Bibliothek Your knowledge hub
Die approbierte gedruckte Originalversion dieser Diplomarbeit ist an der TU Wien Bibliothek verfügbar
The approved original version of this thesis is available in print at TU Wien Bibliothek.

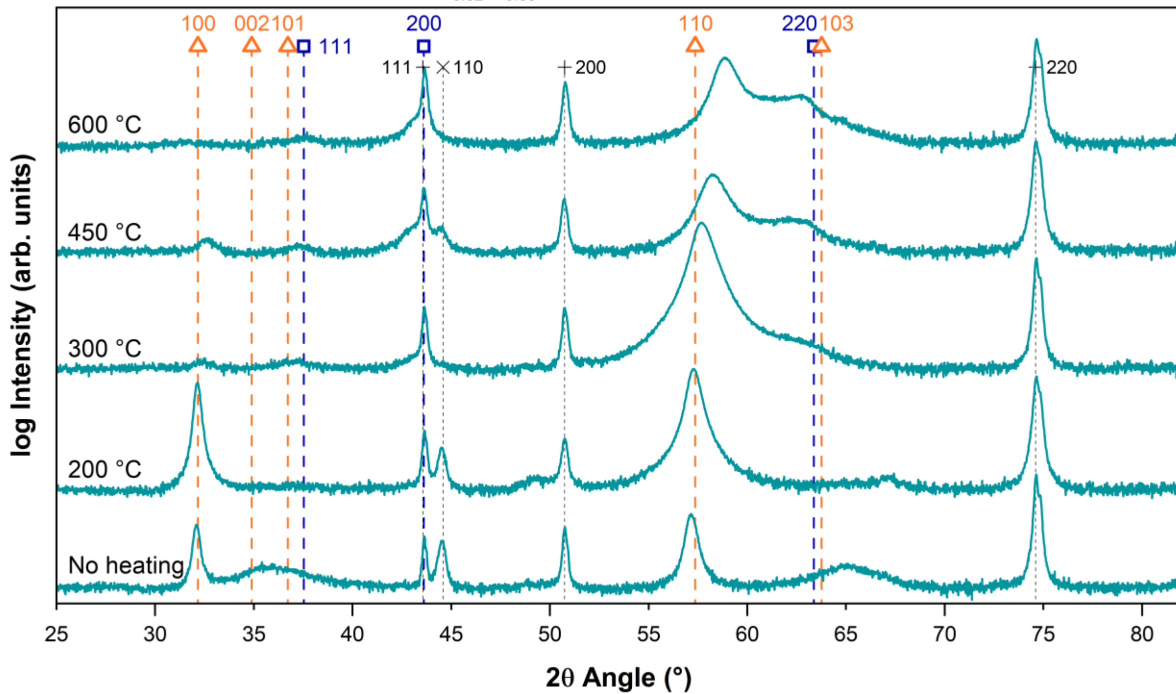

Figure 6.24. Diffractograms of samples made from the 33/67 target with the DC mode at varying substrate temperatures showing fcc-(Ti,Al)N and hexagonal (Al,Ti)N phases.

Die approbierte gedruckte Originalversion dieser Diplomarbeit ist an der TU Wien Bibliothek verfügbar
The approved original version of this thesis is available in print at TU Wien Bibliothek.
TU WIEN Bibliothek Your knowledge hub

The BPDC-50 coatings (see Figure 6.25) show a slightly different result: For example, the thin films deposited without additional heating are completely X-ray amorphous and only at and above 200 °C a higher crystallinity can be observed. The position of the broad X-ray amorphous "peak" leads to the conclusion that hexagonal (Al,Ti)N has already formed. Interestingly, the preferred lattice plane switched completely to (110), but the presence of fcc-(Ti,Al)N (at and above 300 °C) leads to a right shift of the (110) peak and therefore to a smaller lattice spacing in the (111) orientation, for the same reasons as for the DC coatings.

Other planes of hexagonal (Al,Ti)N are hardly present, but at a substrate temperature of 600 °C, the (200) plane of the cubic phase occurs.

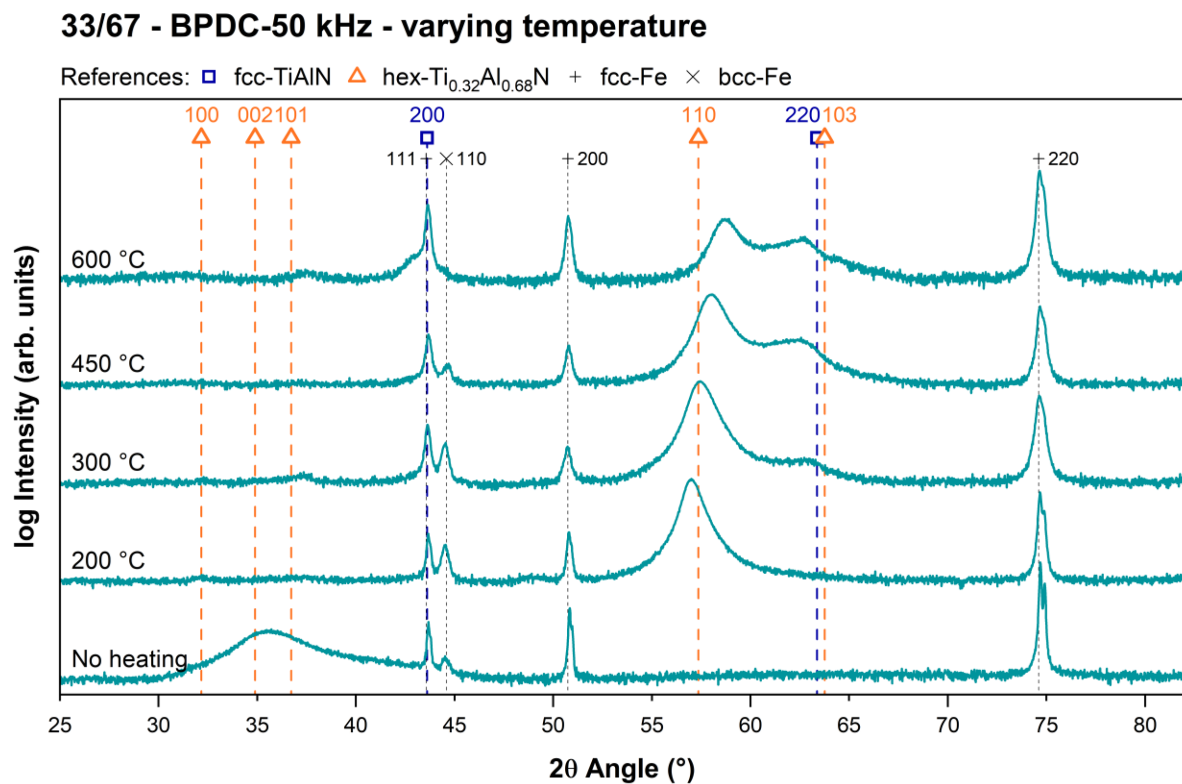

Figure 6.25. Diffractograms of samples made from the 33/67 target with the BPDC-50 mode at varying substrate temperatures showing fcc-(Ti,Al)N and hexagonal (Al,Ti)N phases.

Die approbierte gedruckte Originalversion dieser Diplomarbeit ist an der TU Wien Bibliothek verfügbar
The approved original version of this thesis is available in print at TU Wien Bibliothek.
TU WIEN Bibliothek Your knowledge hub

Once again, the thin films produced with the BPDC-250 mode (see Figure 6.26) do not follow the patterns of the other two sputter modes. The deposition without additional heating and at 200 °C led to coatings with small grains – partly even to X-ray amorphous grain sizes. As mentioned before, this can be explained with a high defect density and in addition, with unfavorable kinetic parameters due to the low substrate temperatures. Remarkably, these X-ray amorphous thin films consist of a fcc-(Ti,Al)N phase, observed through the (111), (200) and (220) planes. As seen in the results of the EDX measurements (see Chapter 6.3.1), Al is understoichiometric in this deposition series and in addition, the Al concentration decreases with increasing temperature. This could be the reason why a cubic phase can form. In thin films produced at and above 300 °C, a hexagonal (Al,Ti)N phase in (110) orientation and at 600 °C also in (103) orientation occurs. Contrary to the other samples of the 33/67 target, the main component is Ti-rich fcc-(Ti,Al)N with hexagonal Al-rich (Al,Ti)N precipitates. Once more, the orientation relation between cubic and hexagonal crystal structure is shown as (220) and (110) respectively. These are the preferred planes as soon as a second phase is forming. The occurring peak shifts can be explained with a combination of large stresses in the coatings and, in case of the cubic matrix, with a higher Ti content in the coatings compared to the reference.

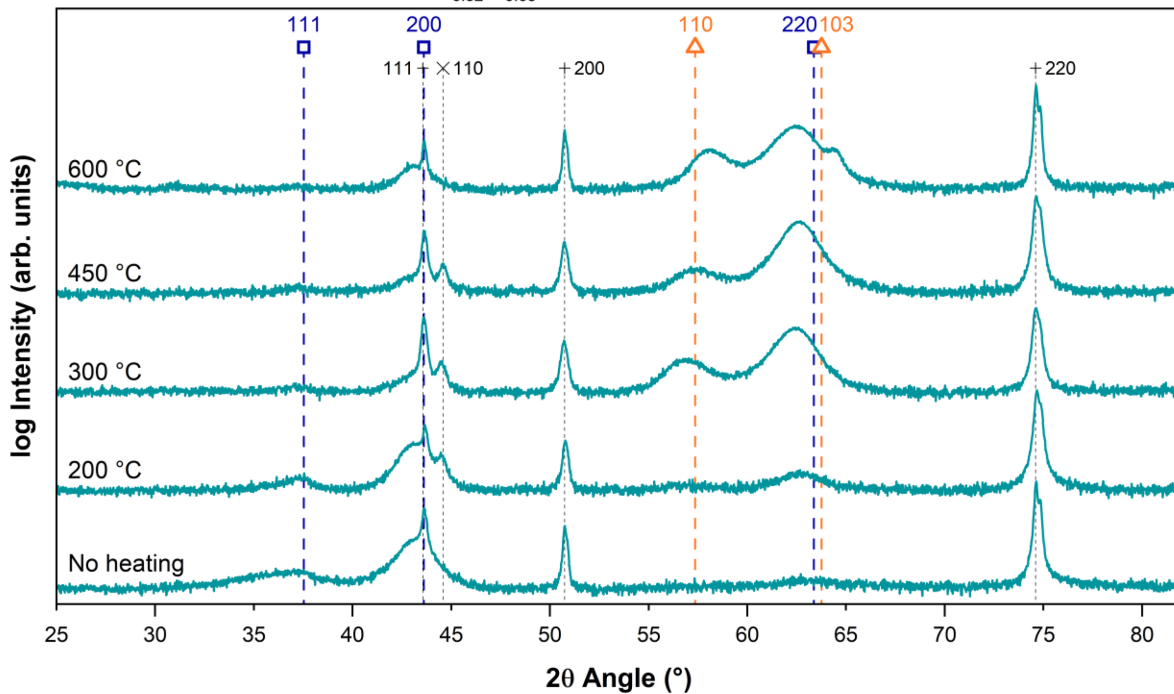

Figure 6.26. Diffractograms of samples made from the 33/67 target with the BPDC-250 mode at varying substrate temperatures showing fcc-(Ti,Al)N and hexagonal (Al,Ti)N phases.

Die approbierte gedruckte Originalversion dieser Diplomarbeit ist an der TU Wien Bibliothek verfügbar
The approved original version of this thesis is available in print at TU Wien Bibliothek.
TU Bibliothek WIEN Your knowledge hub

The 20/80 target coatings (see Figure 6.27, Figure 6.28 and Figure 6.29) follow a similar trend as the thin films produced with the 33/67 target: Deposition without additional heating leads to X-ray amorphous or nearly X-ray amorphous materials and at 200 °C and above the crystallinity is increasing, but still only small grains are formed. Also, the main phase is hexagonal (Al,Ti)N as the concentration of AlN has exceeded the solubility limit of AlN into the TiN lattice.

However, the biggest differences for coatings produced with the DC mode (see Figure 6.27) are the absence of a cubic phase and that mainly the (110) plane of hexagonal (Al,Ti)N occurs. Only the samples produced at 200 °C and 600°C formed (100) and (101) planes, respectively. Although the crystal lattices are certainly exposed to stresses, part of the large peak shifts can be explained by the fact that, while a 20/80 target is present, only a reference for a 33/67 target could be found. The higher Al content shifts the peaks toward pure AlN, which has the (110) peak at a *2θ* angle of approximately 59.35°. However, especially the coating produced at 600 °C shows stresses. The fact that Al is overstoichiometric in the coatings could be the reason why no precipitation of a Ti-rich fcc phase occurred: The Ti content is already very low, but additionally understoichiometric compared to the target concentration (see EDX results, Chapter 6.3.1). Therefore, no cubic precipitates seem to have formed.

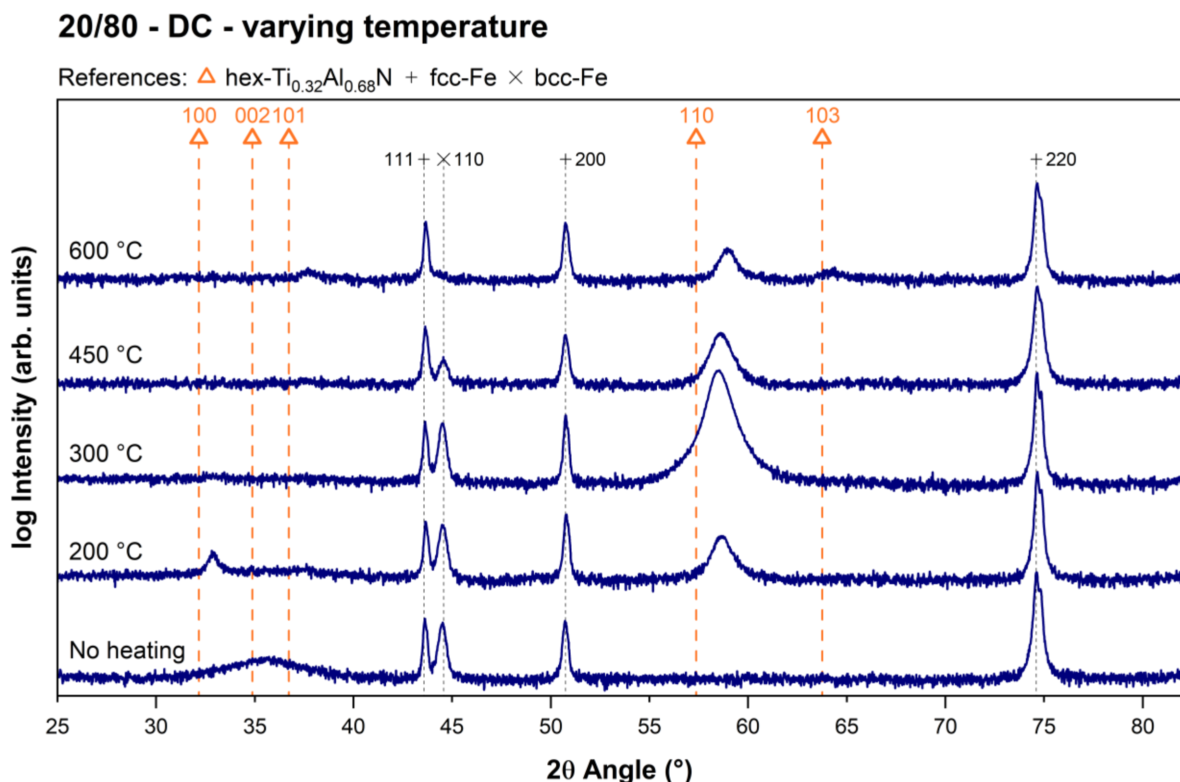

Figure 6.27. Diffractograms of samples made from the 20/80 target with the DC mode at varying substrate temperatures showing hexagonal (Al,Ti)N phases.

Die approbierte gedruckte Originalversion dieser Diplomarbeit ist an der TU Wien Bibliothek verfügbar
The approved original version of this thesis is available in print at TU Wien Bibliothek.
TU Bibliothek WIEN Your knowledge hub

The diffractograms generated for coatings produced with the BPDC-50 mode (see Figure 6.28) show a similar pattern to ones produced with the DC mode: Deposition without additional substrate heating leads to the formation of small to nanometer-sized grains of the hexagonal (Al,Ti)N phase. Furthermore, at 200 °C the crystallinity increases strongly, even stronger than for the DC mode, but only the (110) peak is present. Looking at the diffractograms from 450 °C and 600 °C, this peak has clearly lost intensity, in the case of 600 °C perhaps in favor of the (103) orientation. Once again, there is no fcc-(Ti,Al)N phase, but there seem to be less stresses in the coatings, especially in the ones produced at lower temperatures. The larger right shift of the (110) peak with rising temperature indicates an increase in stresses, since the chemical composition hardly changes (see EDX results, Chapter 6.3.1). As mentioned earlier, part of the shift is due to the use of a reference with lower Al content.

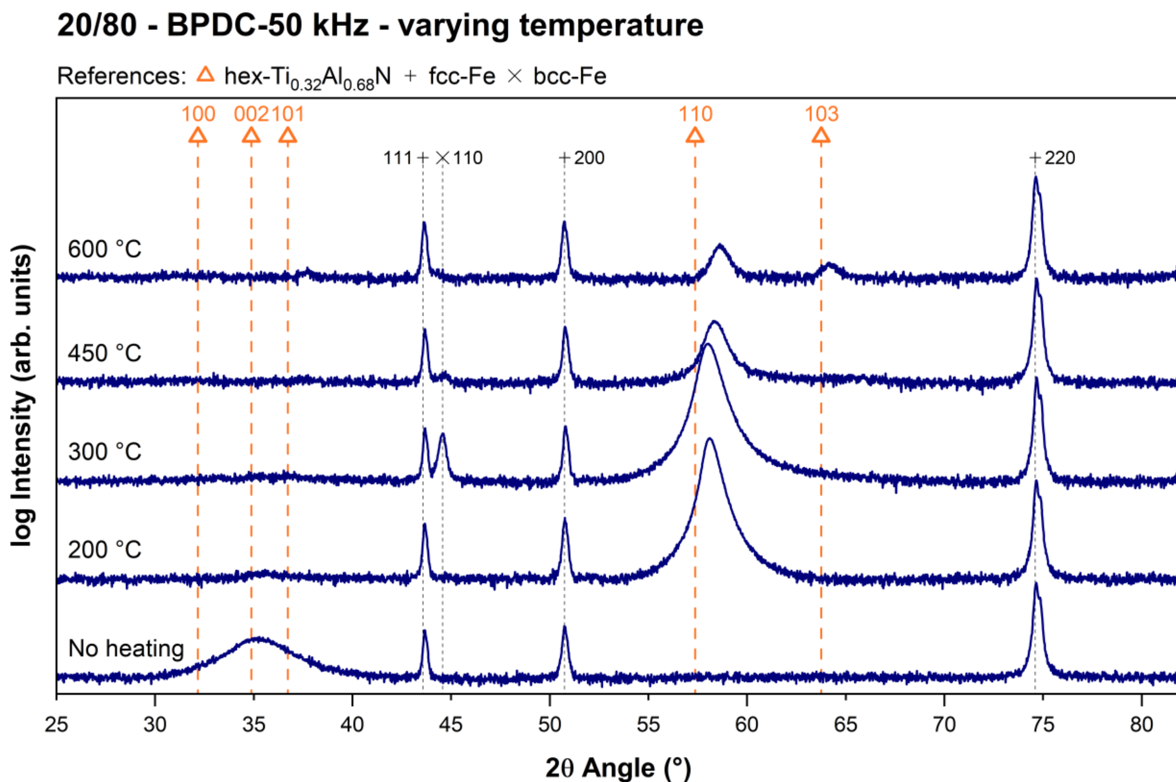

Figure 6.28. Diffractograms of samples made from the 20/80 target with the BPDC-50 mode at varying substrate temperatures showing hexagonal (Al,Ti)N phases.

Die approbierte gedruckte Originalversion dieser Diplomarbeit ist an der TU Wien Bibliothek verfügbar
The approved original version of this thesis is available in print at TU Wien Bibliothek.
TU WIEN Bibliothek Your knowledge hub

The BPDC-250 mode (see Figure 6.29) shows different results than the other two modes with respect to the XRD experiments: Samples deposited without additional heating show a mixture of X-ray amorphous parts and larger grains of the hexagonal (Al,Ti)N phase and already show the (220) peak of fcc-(Ti,Al)N. As with the coatings prepared from the 33/67 target using the BPDC-250 process, this can be explained by the fact that the Al content is understoichiometric compared to the target concentration: The slightly increased Ti content could be sufficient for a cubic phase precipitation to occur even at low temperatures. The position of the (110) peak also suggests this, as it is located to the left of the reference and has therefore been shifted away from pure AlN. However, larger stresses also occur in both phases. The intensity and the grain size are both reduced if the substrate temperature is risen to 200 °C or 300 °C and the (Ti,Al)N peak also disappears. The exact reason for this is currently unknown and will be investigated further in a follow-up project. At 450 °C and 600 °C, the (220) plane of fcc-(Ti,Al)N is present again, even with a quite large fraction compared to the (110) hexagonal (Al,Ti)N peak.

The (110) plane of hexagonal (Al,Ti)N is the preferred one, but the (100), (002) and (101) planes also occur in nanometer-sized grains. The right shift of the (110) peak with rising temperature may be explained with the increasing Al content in the (Al,Ti)N phase due to precipitation of a Ti-rich phase.

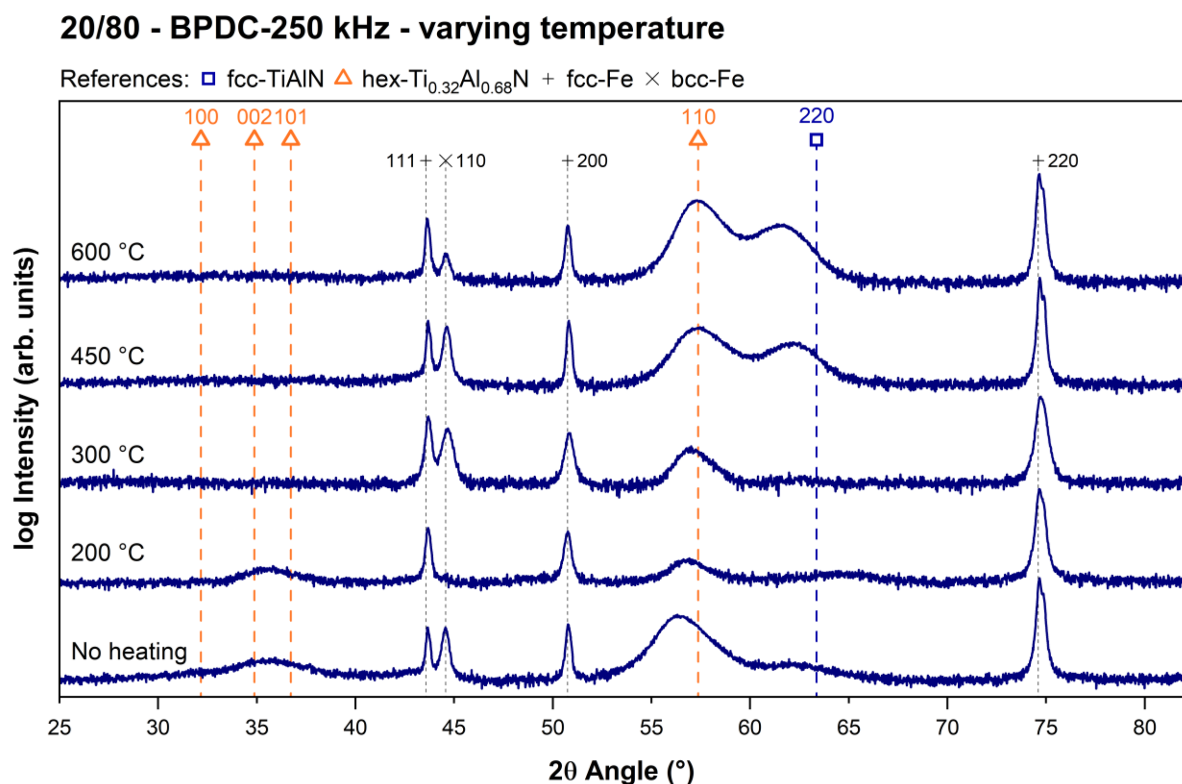

Figure 6.29. Diffractograms of samples made from the 20/80 target with the BPDC-250 mode at varying substrate temperatures showing fcc-(Ti,Al)N and hexagonal (Al,Ti)N phases.

Die approbierte gedruckte Originalversion dieser Diplomarbeit ist an der TU Wien Bibliothek verfügbar
The approved original version of this thesis is available in print at TU Wien Bibliothek.
TU Bibliothek WIEN Your knowledge hub

6.4.2 Crystal Structure – TEM Analysis

The samples examined with TEM confirm the findings of the diffractogram analysis (see Chapter 6.4.1) and of the investigation of the cross section (see Chapter 6.2).

For example, the HAADF image of the sample produced from the 50/50 target using the BPDC-50 mode at 600 °C (see Figure 6.30) shows a structure with only short columns, which is consistent with the corresponding SEM image (see Figure 6.3b). From the integrated line graphs (see Figure 6.31) and the SAED analysis (see Figure 6.32 and Figure 6.33) can be concluded that the coating consists of a mixture of hexagonal and fcc phases occurring in (010) or (111), (002) and (022) planes, respectively. Additionally, some smaller peaks can also be seen, which can be assigned to both phases. The corresponding diffractogram (see Figure 6.22) shows the (110) plane of the hexagonal phase and the (111) and (220) planes of the fcc phase and therefore also a mixture. The ring pattern of the SAED with its almost completely developed rings confirms the analysis of the HAADF and SEM images and suggests a little textured structure.

On the contrary, the second sample examined (33/67 target, DC mode, 450 °C) already shows a different structure with longer columns in the HAADF image and in the SEM image (see Figure 6.34). As before, a mixture of hexagonal and fcc phases can be seen in the integrated line graphs (see Figure 6.35) and the diffractogram (see Figure 6.24). In the latter, the hexagonal planes (100), (101), (110) and (103) occur as well as the fcc planes (200) and (220). The preferred orientations are (110) and (220). The SAED analysis reveals similar planes: (010), (012), (110) and (111) of the hexagonal phase and (111), (002) and (022) of the fcc phase. The obtained images (see Figure 6.36 and Figure 6.37) also show a ring pattern of elongated spots, indicating a strongly textured structure which is consistent with other findings.

The HAADF image of the last sample (20/80 target, BPDC-250 mode, 600 °C) also shows a columnar structure (see Figure 6.38) with a transition from equiaxed grains near the substrate to long columns. Furthermore, the coating consists of a mixture of hexagonal and fcc phase, proven by the integrated line graphs (see Figure 6.39). The diffractogram (see Figure 6.29) confirms this with the (110) hexagonal plane and the (220) fcc plane. The SAED analysis resulted in more planes as there are (010), (012), (013) and (020) of the hexagonal phase and (111), (002) and (222) of the fcc phase. Other planes can be assigned to both phases as in the first sample. The SAED reveal once again a highly textured coating as the ring pattern shows elongated spots and not full rings.

Die approbierte gedruckte Originalversion dieser Diplomarbeit ist an der TU Wien Bibliothek verfügbar
The approved original version of this thesis is available in print at TU Wien Bibliothek.
TU Bibliothek WIEN Your knowledge hub

50/50 target – BPDC-50 kHz mode – 600 °C

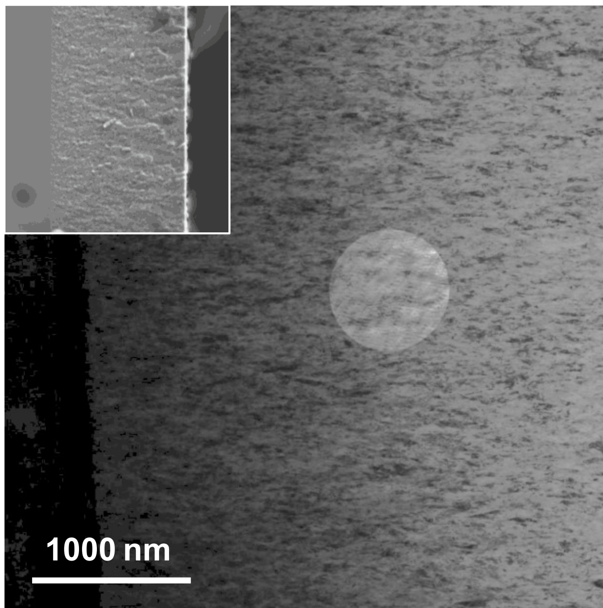

Figure 6.30. HAADF image with SAED area indicated – substrate on the left and SEM image in the left corner (50/50 target).

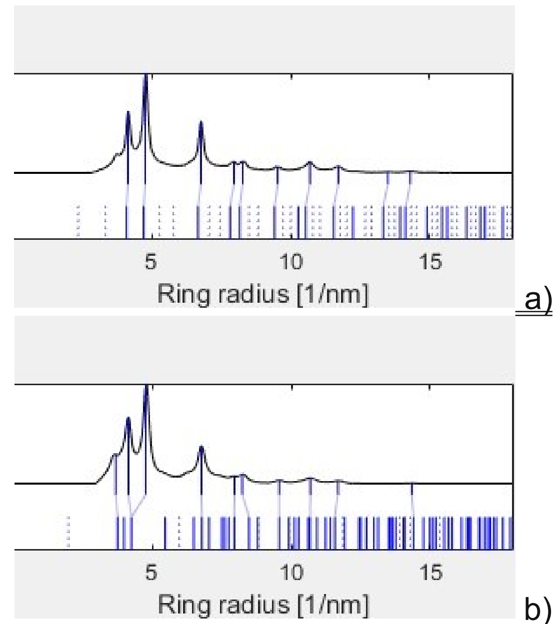

Figure 6.31. Integrated line graph with **a)** fcc-TiN and **b)** hexagonal AlN reference (50/50 target).

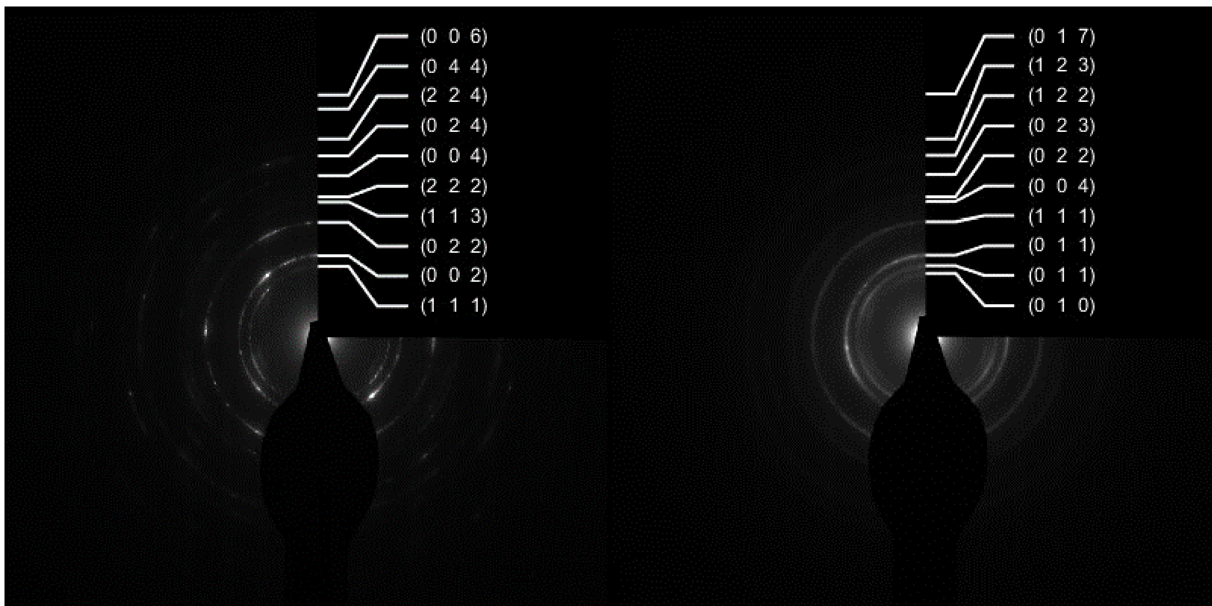

Figure 6.32. SAED ring pattern and assigned lattice planes of fcc-TiN (50/50 target).

Figure 6.33. SAED ring pattern and assigned lattice planes of hexagonal AlN (50/50 target).

Die approbierte gedruckte Originalversion dieser Diplomarbeit ist an der TU Wien Bibliothek verfügbar
The approved original version of this thesis is available in print at TU Wien Bibliothek.
TU WIEN Bibliothek Your knowledge hub

33/67 target – DC mode – 450 °C

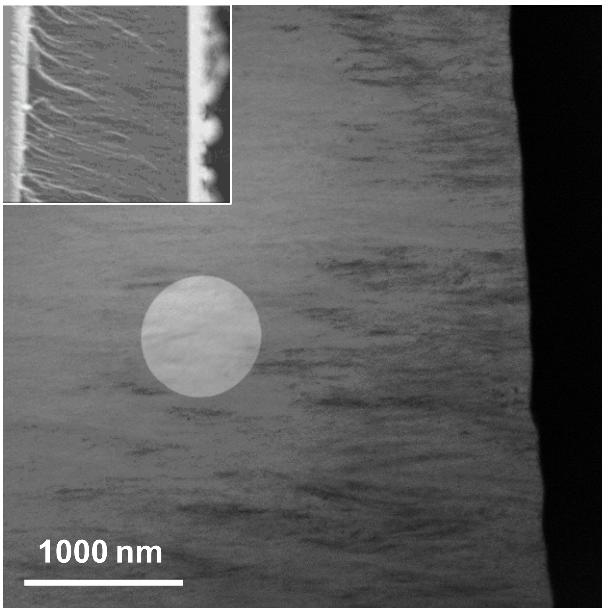

Figure 6.34. HAADF image with SAED area indicated – substrate on the left and SEM image in the left corner (33/67 target).

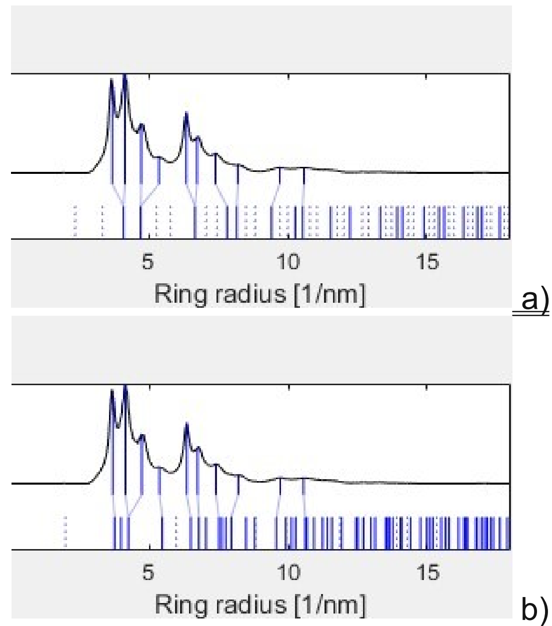

Figure 6.35. Integrated line graph with **a)** fcc-TiN and **b)** hexagonal AlN reference (33/67 target).

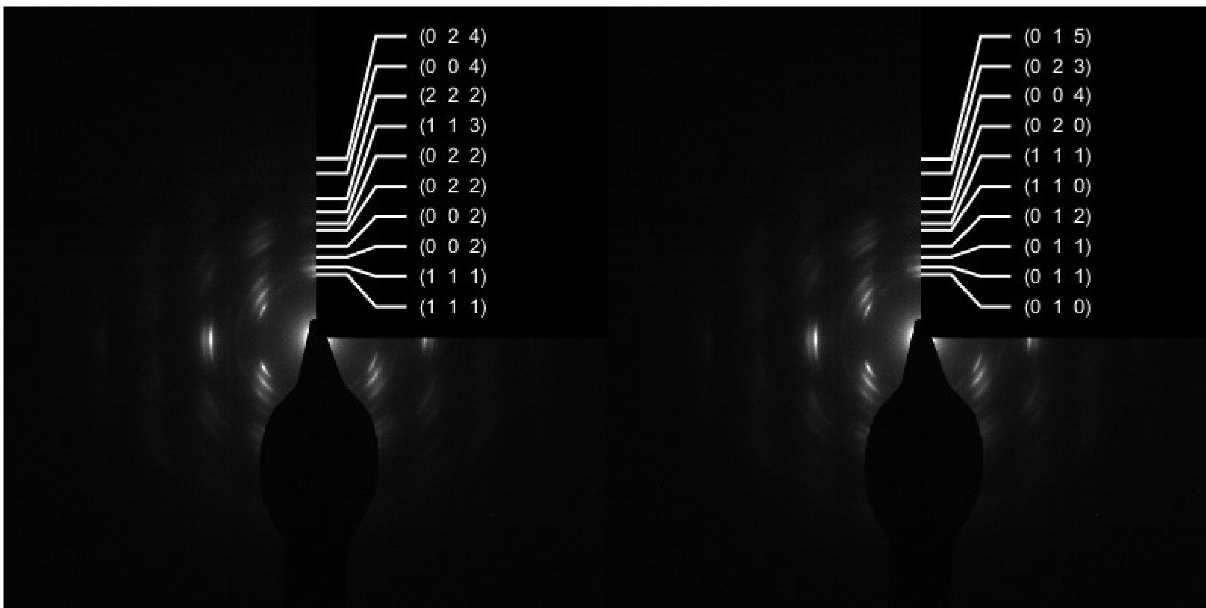

Figure 6.36. SAED ring pattern and assigned lattice planes of fcc-TiN (33/67 target).

Figure 6.37. SAED ring pattern and assigned lattice planes of hexagonal AlN (33/67 target).

Die approbierte gedruckte Originalversion dieser Diplomarbeit ist an der TU Wien Bibliothek verfügbar
The approved original version of this thesis is available in print at TU Wien Bibliothek.
TU WIEN Bibliothek Your knowledge hub

20/80 target – BPDC-250 kHz mode – 600 °C

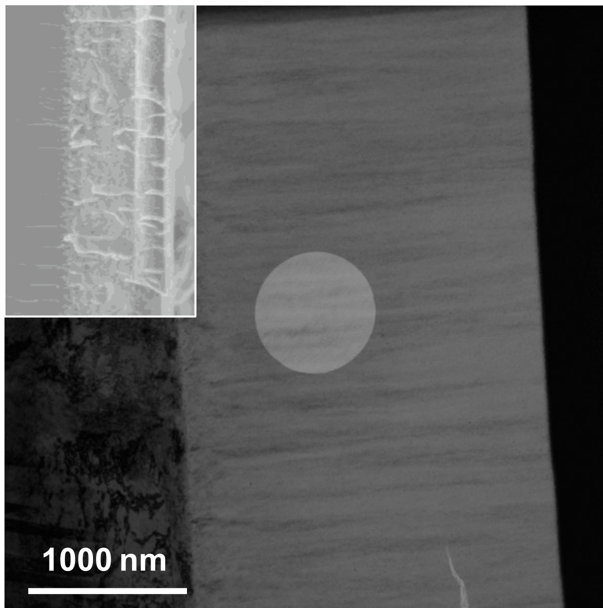

Figure 6.38. HAADF image with SAED area indicated – substrate on the left and SEM image in the left corner (20/80 target).

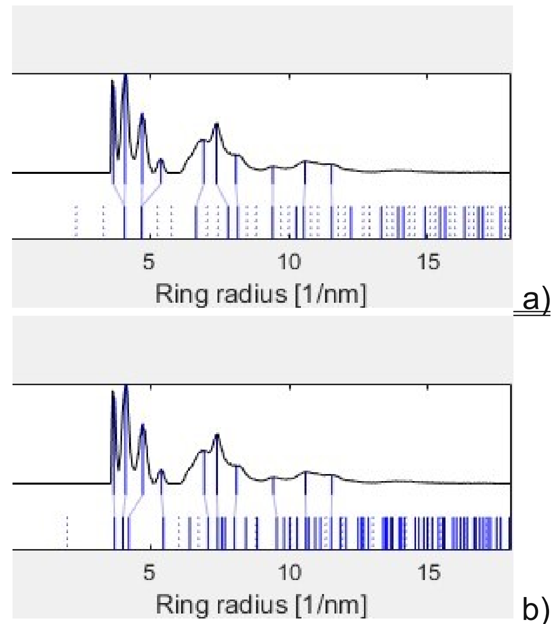

Figure 6.39. Integrated line graph with **a)** fcc-TiN and **b)** hexagonal AlN reference (20/80 target).

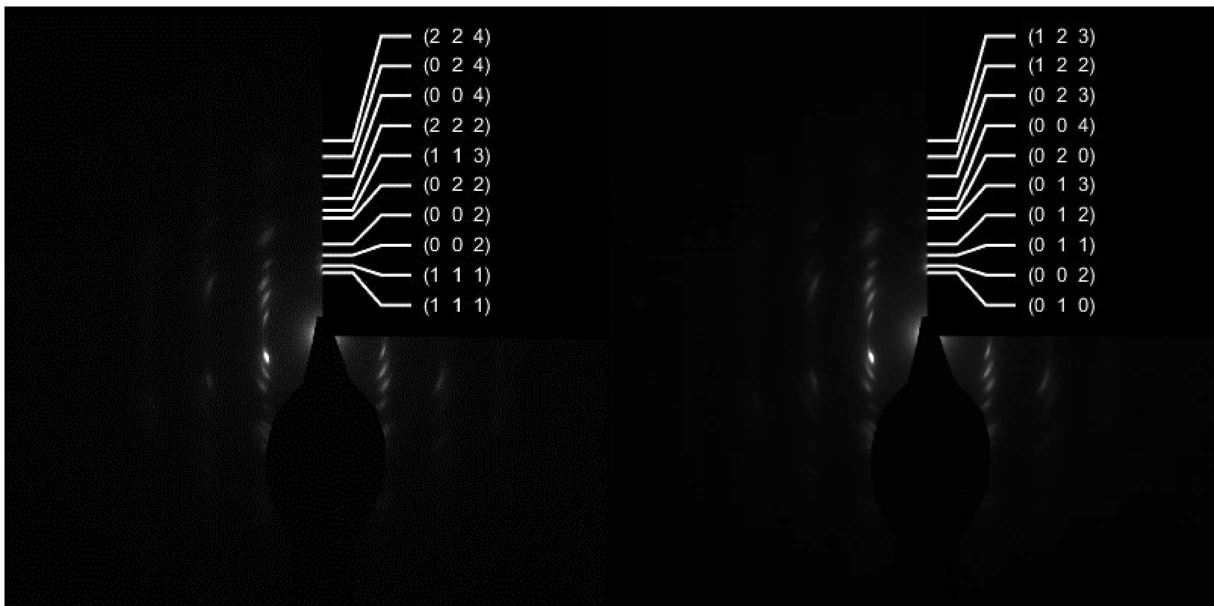

Figure 6.40. SAED ring pattern and assigned lattice planes of fcc-TiN (20/80 target).

Figure 6.41. SAED ring pattern and assigned lattice planes of hexagonal AlN (20/80 target).

Die approbierte gedruckte Originalversion dieser Diplomarbeit ist an der TU Wien Bibliothek verfügbar
The approved original version of this thesis is available in print at TU Wien Bibliothek.
TU Bibliothek Your knowledge hub WIEN

6.5 Mechanical Properties

Comparing the results of hardness and elastic modulus of the three material systems (see Figure 6.42), the samples of the 50/50 target provide the highest values of all measurements. The main reason for this is their crystal structure: All 50/50 coatings crystallized in the fcc structure (see Figure 6.21, Figure 6.22 and Figure 6.23) and Ti-Al-N phases are known to have much higher hardness values when they are in the cubic structure rather than in the hexagonal one. [6] Furthermore, all results of hardness and elastic modulus seem to depend mainly on the crystallographic properties of the coatings and are not directly influenced by the chemical composition.

For example, the hardness values of coatings produced with the 50/50 target and the DC mode decline from 33.64 GPa to 28.86 GPa as the substrate temperature rises (from no heating to 450 °C). The corresponding diffractograms (see Figure 6.21) show an increase of the (200) plane combined with a decrease of the (220) plane of the cubic (Ti,Al)N phase in this temperature range. At 600 °C the hardness reaches higher values again – 31.94 GPa –, explainable by the precipitation of a second hexagonal (Al,Ti)N phase, which leads to distortions in the lattice and therefore, the hardness is increased. Nevertheless, the hardness value is lower than that of the coating produced without additional heating, probably due to the significantly lower intensity of the (111) peak. The elastic modulus behaves contrary to the hardness (increase from 376 GPa to 428 GPa), except for a drop at 450 °C (390 GPa).

The BPDC-50 mode shows similar results to the DC mode, except that the lowest hardness value here is at 300 °C (29.27 GPa), presumably because here the coating deposited at 450 °C has a higher proportion of the (220) plane. At 600 °C, the coating with the highest hardness value of 38.21 GPa of the entire test series was produced. Compared to the DC mode, this thin film has a lower proportion of hexagonal phase relative to the cubic phase and shows a much higher intensity of the (111) peak (see Figure 6.22). It seems to be that the highest values can be obtained if the right amount of an Al-rich hexagonal phase forms, which leads to a distortion of the crystal lattice and subsequently to higher hardness values. If the amount of this phase is increasing further, the hardness decreases. This was observed also by others [39]. The other hardness values of this sputter mode are in the range of those measured in DC mode (31.59 GPa, 30.85 GPa and 31.25 GPa) and the elastic modulus (values: between 385 GPa and 504 GPa) also shows similar trends.

TU WIEN Bibliothek Your knowledge hub
Die approbierte gedruckte Originalversion dieser Diplomarbeit ist an der TU Wien Bibliothek verfügbar
The approved original version of this thesis is available in print at TU Wien Bibliothek.

The diffractograms of the BPDC-250 mode (see Figure 6.23) show hardly any (200) peaks, instead the intensity is higher at the (220) peak and in addition, the corresponding hardness values do not decrease as much as those of the other sputter modes. Another positive difference is the hardness value of 450 °C coatings (36.25 GPa), which is significantly higher than those of coatings produced at lower temperatures (31.88 GPa, 31.66 GPa and 31.61 GPa) and almost as high as that of 600 °C (36.81 GPa). The reason for this could be the higher proportion of the (220) plane compared to the (111) plane and the high distortion in the crystal lattice. For the sample produced at 600 °C, the (111) peak of the cubic phase shows a slight asymmetry and a strong peak shift compared to the reference, both of which lead to high stresses and thus to high hardness values. The elastic modulus of the BPDC-250 mode behaves similarly to the other sputter modes (values: from 388 GPa to 437 GPa).

The most obvious differences to coatings produced with the 33/67 target are first the lower hardness values (all are below 30 GPa), that the elastic modulus behaves mostly like the hardness, but also the dependence on the substrate temperature: In general, the hardness increases with rising temperature. The increase in hardness for DC mode samples can be explained first by an increase in crystallinity (from 17.02 GPa to 20.09 GPa), then precipitates of a cubic phase favor high hardness values (20.96 GPa and 22.55 GPa) – for the diffractograms see Figure 6.24. Between the coatings produced at 450 °C and 600 °C, there is a jump in hardness to 29.91 GPa (the highest value of samples from the 33/67 target), which occurs on the one hand due to a higher content of cubic phase, but on the other hand also due to greater distortions in the lattice. The values of the elastic modulus with rising temperature range from 185 GPa to 276 GPa.

This jump cannot be seen in hardness values of the BPDC-50 mode. Although more cubic phase is found in the sample produced at 600 °C (see diffractogram in Figure 6.25), the hardness value is lower than that of the DC mode. Therefore, there seems to be an upper limit to the amount of cubic phase precipitating from the hexagonal matrix, which is beneficial for high hardness. Otherwise, the same trends are observed: Increasing crystallinity, cubic phase content and lattice distortion lead to an increase in hardness with rising temperature. However, all hardness values of the BPDC-50 mode are lower than those of the DC mode: 15.99 GPa, 17.29 GPa, 19.84 GPa, 23.22 GPa and 25.99 GPa. The values of the elastic modulus are also increasing with rising temperature from 179 GPa to 269 GPa.

The hardness of the BPDC-250 mode shows a similar pattern to the other sputter modes, although there are some deviations: First, even though the hardness is increasing with rising

TU WIEN Bibliothek Your knowledge hub
Die approbierte gedruckte Originalversion dieser Diplomarbeit ist an der TU Wien Bibliothek verfügbar
The approved original version of this thesis is available in print at TU Wien Bibliothek.

temperature, there is a drop at 450 °C (24.57 GPa) and secondly, the elastic modulus values are jumping from 169 GPa to finally 361 GPa, but then decrease strongly to 263 GPa. There is also a jump in the hardness values between 200 °C and 300 °C (from 18.57 GPa to 25.50 GPa), which can be explained mainly by a sharp increase in crystallinity and a smaller intensity of the (200) peak of the cubic main phase (see diffractogram in Figure 6.26). Also, the precipitation of a second phase – here a hexagonal Al-rich one – leads to an increased hardness and gives at the same time an explanation for the drop at 450 °C, since the proportion of the second phase is lower in this sample compared to the other coatings. Especially the thin film produced at 600 °C shows a high hardness of 27.11 GPa, which is the second highest value of the 33/67 target. This was caused, among other things, by the appearance of the (103) plane of the hexagonal phase. In contrast, without additional heating of the substrates, the coating with the second lowest hardness value of the 33/67 target test series of 14.85 GPa was formed, which can be explained mainly by the low crystallinity and a high intensity of the cubic (200) peak.

The lowest hardness value of the whole test series of 14.39 GPa is found in samples of the 20/80 targets produced with the BPDC-50 mode and without additional heating, but also the counterpart made with the DC mode shows a low value of 15.55 GPa. Both are caused by a low crystallinity and a (nearly) X-ray amorphous structure (see diffractograms in Figure 6.24 and Figure 6.25). This in turn explains why a large jump of the hardness can be seen in both sputter modes compared to the 200°C coatings (DC: 22.02 GPa; BPDC-50: 20.68 GPa). According to their diffractograms, they have a significantly higher crystallinity. However, the DC mode shows little change beyond that, both in diffractograms (see Figure 6.24) and hardness values (22.70 GPa, 23.46 GPa and 23.39 GPa), the latter being similar in value to those of the 33/67 target. Only the values of the elastic modulus increase more significantly from 176 GPa to 290 GPa with rising temperature.

Unlike the DC mode, the hardness of coatings produced with the BPDC-50 mode increases continuously with rising temperature and in addition reaches higher values: 14.39 GPa, 20.68 GPa, 21.25 GPa, 22.40 GPa and 24.61 GPa. While deposition at 200 °C and 300 °C produced coatings with similar crystal structure (see diffractogram in Figure 6.25) and thus with similar hardness values, more stresses occur at the higher temperatures, which is also reflected in the higher hardness values. At 600 °C, the (103) plane was additionally formed, which also favors high hardness. The elastic modulus behaves similarly to the hardness with values from 174 GPa to 247 GPa, except at 300 °C where a small drop can be observed.

Die approbierte gedruckte Originalversion dieser Diplomarbeit ist an der TU Wien Bibliothek verfügbar
The approved original version of this thesis is available in print at TU Wien Bibliothek.
TU WIEN Bibliothek Your knowledge hub

The pattern of hardness values of the BPDC-250 mode is more like that of the 50/50 targets: Initially, the hardness falls, then rises again at higher temperatures. Furthermore, the hardness value of the coating produced without additional heating (24.00 GPa) is already comparable to those produced at higher temperatures with the other sputter modes, even to those of the 33/67 target. The reason for this is probably the significantly higher crystallinity and the beginning precipitation of a second cubic Ti-rich phase. Also, major stresses can be observed when looking at the diffractogram (see Figure 6.29). The decrease in hardness to the 200 °C coating can be explained with a decreased crystallinity and there seems to be no cubic phase anymore, but with a value of 21.32 GPa the hardness is still high compared to the others. In the samples produced at 300 °C such high stresses occurred that they cracked multiple times and a nanoindentation measurement would have led to wrong results. Although the coating produced at 450 °C has formed grains of a Ti-rich cubic phase, its hardness (21.72 GPa) is hardly exceeding that of the one produced at 200 °C. Since the content of the cubic phase is high relative to the hexagonal one compared to other diffractograms, it can be concluded that the proportion is too large to achieve a high hardness. Especially since the 600 °C coating has a lower cubic content and is at the same time the hardest coating of the 20/80 target (28.23 GPa), surpassed only by the hardness values of the 50/50 target and a single value of the 33/67 target. The elastic modulus behaves contrary to the hardness with the values ranging from 242 GPa to 292 GPa.

The elastic modulus is influenced by a complex array of parameters, for example grain size, morphology, or preferred orientation. In the scope of this project, no clear correlation was made between these factors. Rather, only the correlation to the change in hardness was noted.

Die approbierte gedruckte Originalversion dieser Diplomarbeit ist an der TU Wien Bibliothek verfügbar
The approved original version of this thesis is available in print at TU Wien Bibliothek.
TU WIEN Bibliothek Your knowledge hub

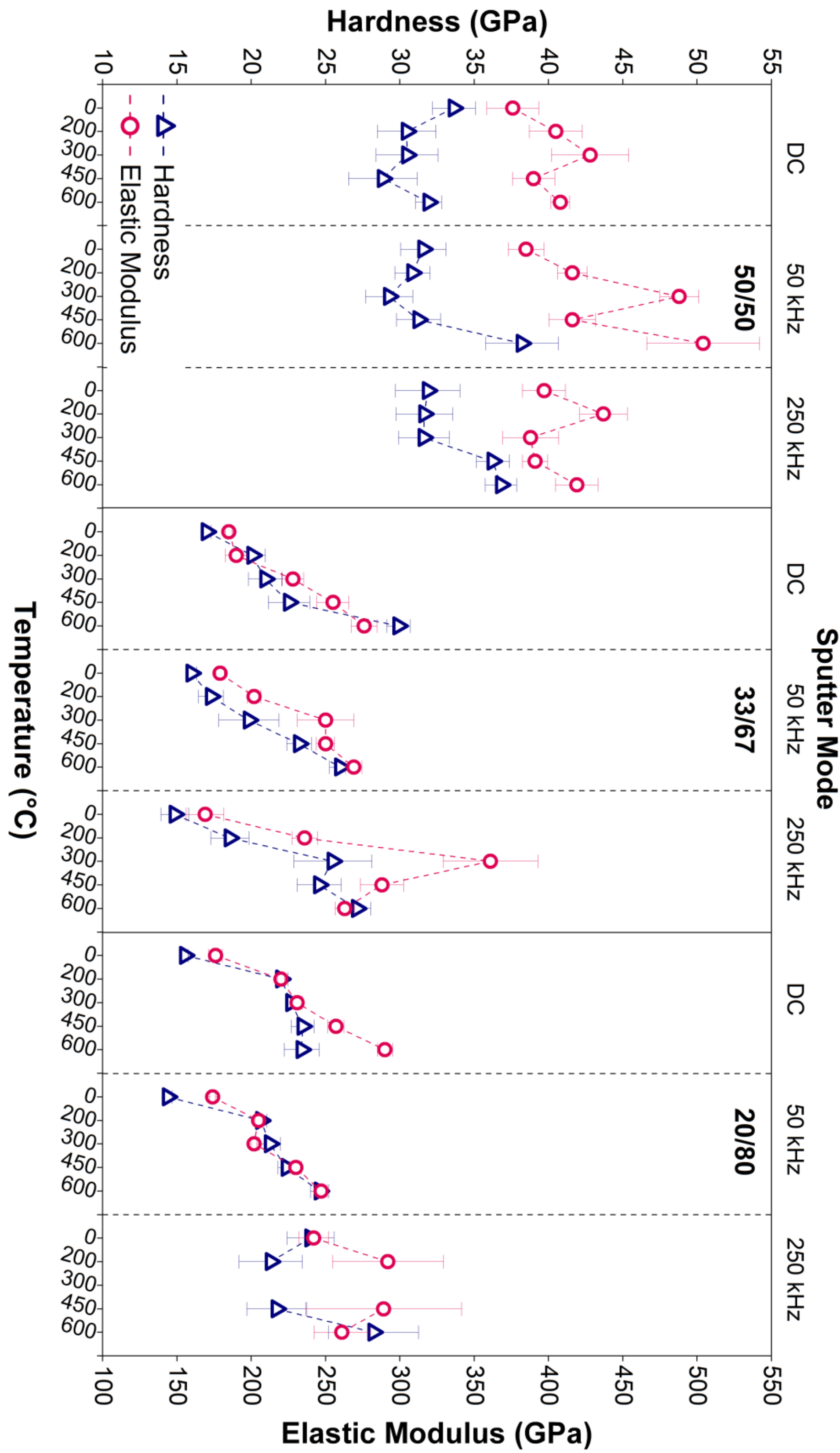

Figure 6.42. Hardness and Elastic Modulus in GPa for the three different targets with varying temperatures and sputter modes before annealing. 0 °C refers to no additional heating.

Die approbierte gedruckte Originalversion dieser Diplomarbeit ist an der TU Wien Bibliothek verfügbar
The approved original version of this thesis is available in print at TU Wien Bibliothek.
TU Bibliothek WIEN Your knowledge hub

6.6 Thermal Stability

6.6.1 Appearance of the Surface after Annealing

Images were taken of the surface of the coatings before and after annealing to investigate possible surface damages. An *Olympus BX41M-LED* light microscope was used for this purpose, and images were taken at a one hundred times magnification unless stated otherwise.

The coating produced from the 50/50 target with the DC mode at 200 °C shows macro-spalling (visible to the naked eye) and a high number of surface cracks, which could have formed because of high thermal stresses and microstresses in the coating during the annealing process (see Figure 6.43). The thin film deposited from the same target but with the BPDC-50 mode at 600 °C also seems to have experienced high stresses, leading to micro-spalling (only visible under a microscope; see Figure 6.44). The next sample (33/67 target, DC mode, 200 °C) was able to withstand annealing better and the surface shows no obvious signs of cracking or similar surface damages (see Figure 6.45). The surface of another sample (33/67 target, BPDC-50 mode, no additional heating) has experienced macro-spalling and cracked multiple times, giving an interesting picture with a remarkable high number of crack branches (see Figure 6.46 and Figure 6.47). After annealing, the coating produced from the 20/80 target using BPDC-50 mode at 300 °C shows only a higher number of large macropores, but no pronounced cracks in the surface (see Figure 6.48).

The reason, why some coatings experience more stresses and thus more surface damage than others is currently inconclusive and will be investigated further in the future.

Die approbierte gedruckte Originalversion dieser Diplomarbeit ist an der TU Wien Bibliothek verfügbar
The approved original version of this thesis is available in print at TU Wien Bibliothek.
TU WIEN Bibliothek Your knowledge hub

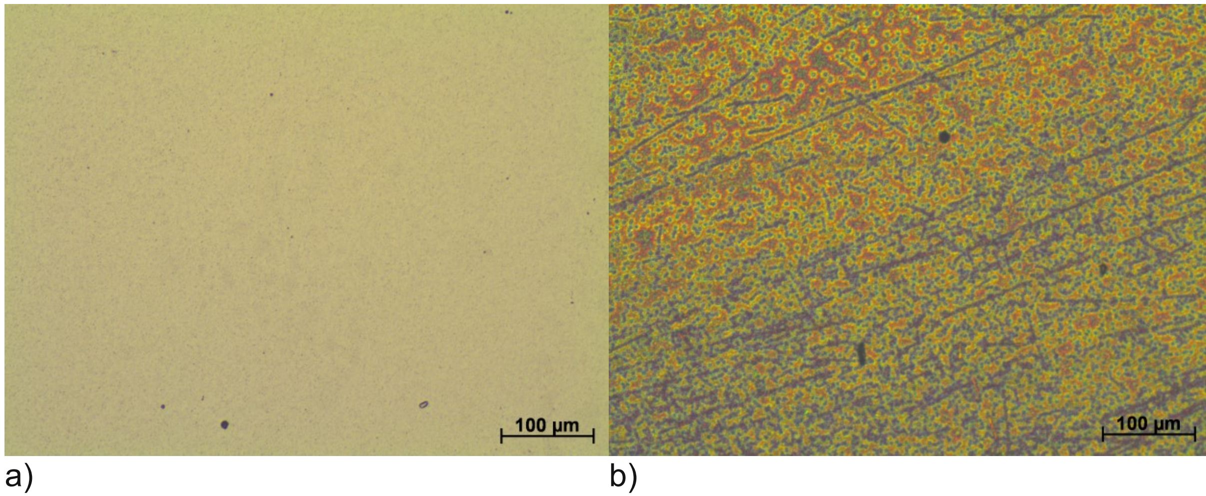

Figure 6.43. Surface of the coating **a)** before and **b)** after annealing (50/50 target, DC mode, 200 °C).

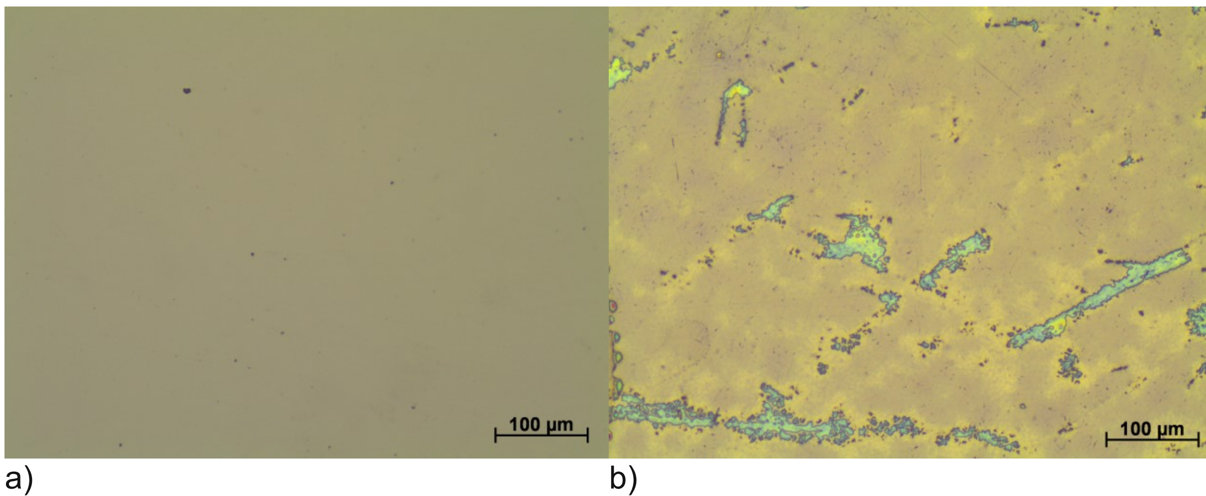

Figure 6.44. Surface of the coating **a)** before and **b)** after annealing (50/50 target, BPDC-50 mode, 600 °C).

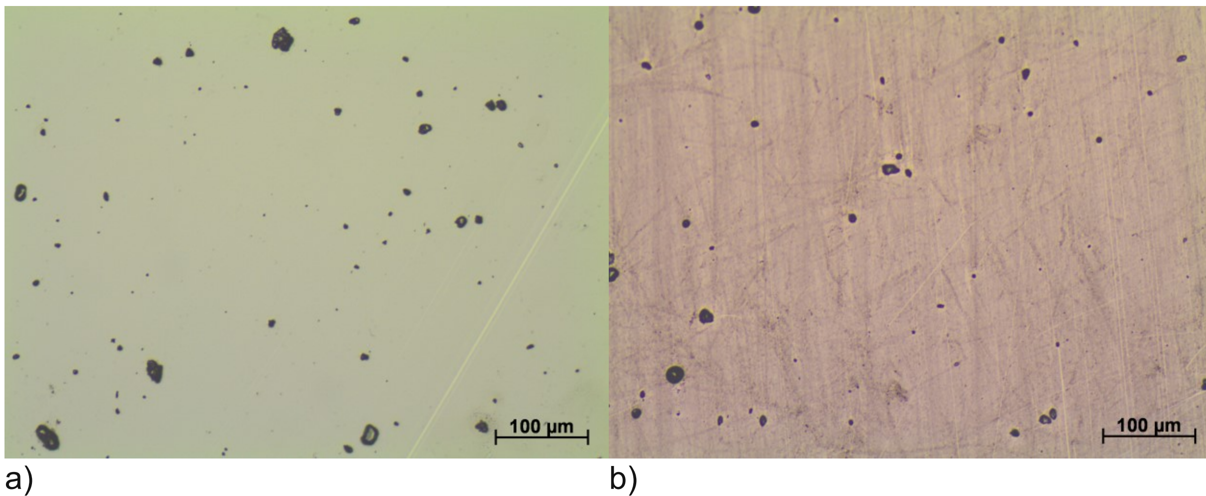

Figure 6.45. Surface of the coating **a)** before and **b)** after annealing (33/67 target, DC mode, 200 °C).

Die approbierte gedruckte Originalversion dieser Diplomarbeit ist an der TU Wien Bibliothek verfügbar
The approved original version of this thesis is available in print at TU Wien Bibliothek.
TU Bibliothek Your knowledge hub WIEN

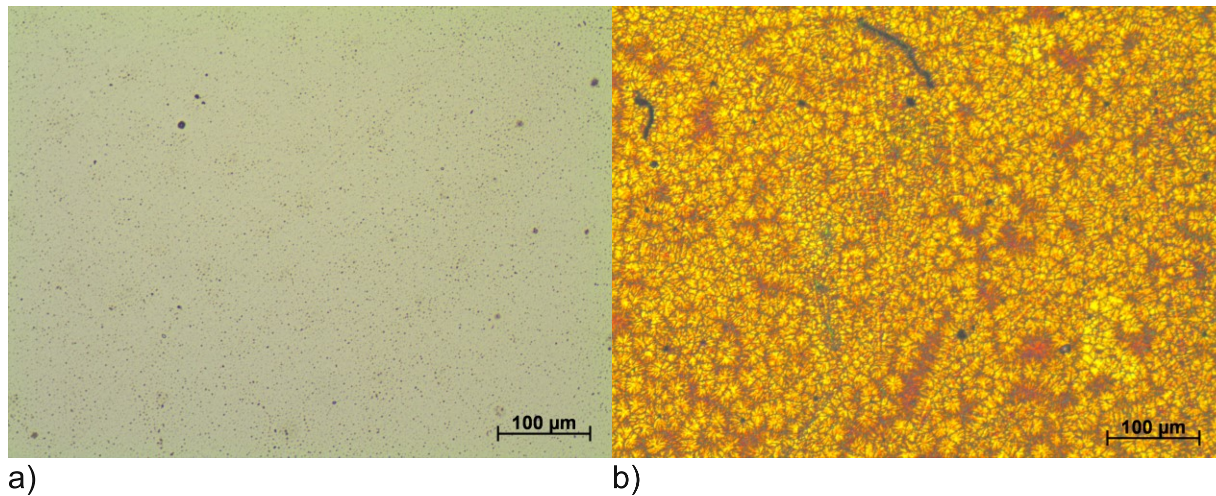

Figure 6.46. Surface of the coating **a)** before and **b)** after annealing (33/67 target, BPDC-50 mode, no heating).

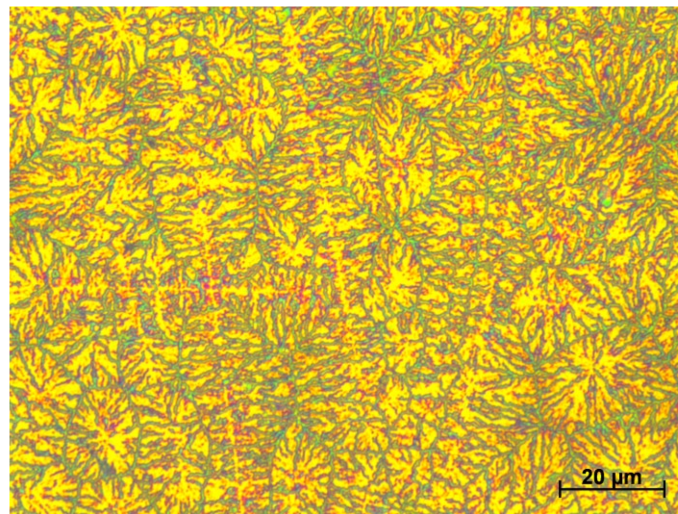

Figure 6.47. Surface of the coating after annealing (33/67 target, BPDC-50 mode, no heating); image taken at a five hundred magnification.

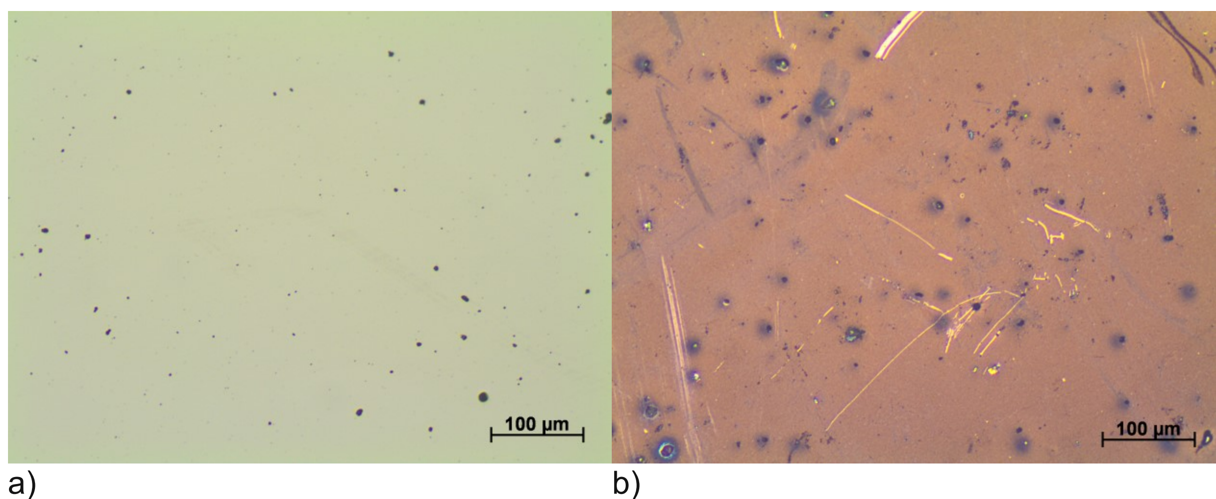

Figure 6.48. Surface of the coating **a)** before and **b)** after annealing (20/80 target, BPDC-50 mode, 300 °C).

Die approbierte gedruckte Originalversion dieser Diplomarbeit ist an der TU Wien Bibliothek verfügbar
The approved original version of this thesis is available in print at TU Wien Bibliothek.
TU WIEN Bibliothek Your knowledge hub

6.6.2 Crystal Structure during and after Annealing

The evolution of the crystal structure during annealing of the thin film deposited from the 50/50 target with the DC mode at 200 °C is not clear (see Figure 6.49). It started with a complete solid solution of fcc-Ti-Al-N with an already coarse-grained structure, whereby especially the (111) plane and therefore the (222) plane occur, but also (200), (220) and (311) planes. During annealing, the thermal expansion of the lattice leads to a leftward shift of the peaks, thus towards larger lattice spacing. This can be observed in all samples examined. The before mentioned structure hardly changes during annealing, except that the coating experiences additional stresses especially in the (222) orientation at higher temperatures and that the (220) plane nearly disappears. The stresses seem to have caused multiple cracks (see Figure 6.43), which in turn led to a relaxation of the coating after cooling. Looking at the diffractogram recorded after the annealing process, some small peaks can be noticed. They cannot be clearly assigned to a second phase but could indicate the formation of Ti-rich and Al-rich solid solution regions in the matrix.

Another sample from the 50/50 target (BPDC-50 mode, 600 °C; see Figure 6.50) shows similar trends to the first one, but here a hexagonal phase precipitates from the fcc-Ti-Al-N matrix, enriching the cubic matrix in Ti. This can be clearly seen in the left shift of the cubic peaks (111), (200), (220) and (311) towards pure fcc-TiN. However, similar to the previous coating, this sample also shows increasing stresses in the (220) orientation at higher temperatures. After cooling, the surface is damaged in wide areas by micro-spalling (see Figure 6.44). The hexagonal (Al,Ti)N phase occurs with the (100), (110) and maybe the (103) plane. Other visible peaks in the diffractograms might appear, as mentioned above, due to the formation of Al-rich solid solution regions.

The coatings from the 33/67 target, on the other hand, show a different picture. With the DC mode and at 200 °C (see Figure 6.51) a thin film was deposited which only consists of a hexagonal (Al,Ti)N phase with (100) and (110) planes. During annealing, it has decomposed into hexagonal AlN ((100) and (110) planes) and fcc-TiN ((220) plane). The Al content in the solid solution increases steadily as soon as TiN is precipitated (starting at approximately 700 °C), and the peaks move towards pure AlN. Furthermore, the TiN phase is oriented to the main plane of the hexagonal matrix, which is (110), to minimize coherency stresses. The peak shifts in the diffractogram seem to be mainly caused by thermal expansion and not because of stresses. Therefore, the surface remained undamaged (see Figure 6.45). As one can see, there are further peaks shown in the diffractogram to which none of the present phases fit. One

Die approbierte gedruckte Originalversion dieser Diplomarbeit ist an der TU Wien Bibliothek verfügbar
The approved original version of this thesis is available in print at TU Wien Bibliothek.
TU WIEN Bibliothek Your knowledge hub

possible explanation could be that they indicate the presence of (understoichiometric) oxides of Ti and Al, but the peak intensity is too low compared to the background noise to make exact phase indication possible.

The second sample from the 33/67 target, which was examined in more detail, was deposited using the BPDC-50 mode and without additional heating (see Figure 6.52). This resulted in an X-ray amorphous coating that crystallized into hexagonal AlN and fcc-TiN upon annealing. Different from other samples, the preferred planes of AlN are (002) followed by (110) and of TiN (200) followed by (111). This deviation from other coatings could be explained with a more stress-free formation of phases and grains. The X-ray amorphous starting material can segregate without previously determined orientations and prefers for this purpose planes with the lowest surface energies. For example, according to Gall et al., this is the (100) plane for TiN. [40] Although the diffraction pattern suggests that no stresses have occurred, the surface is characterized by a large number of cracks after annealing (see Figure 6.46 and Figure 6.47). It is possible that the high temperatures enabled grain growth and the formation of a structure with low stresses, but during cooling various stresses increased and eventually led to the cracking of the surface. At a 2θ angle of around 40° between approximately 700 °C and 1150 °C, an additional phase arises to which none of the references mentioned in this thesis fits. However, as the samples were mounted on a silicon wafer before the measurements, it is possible that silicon is reacting with remaining oxygen in the vacuum chamber in this temperature range. Thus, SiO_{θ} is formed, which volatilizes above 1200 °C. [41] Comparison with references showed that SiO_2 has in several crystal structures a peak around this angle. In Figure 6.52, a reference of SiO_2 in rutile structure is exemplarily shown.

The thin film produced from the 20/80 target with the BPDC-50 mode at 300 °C only consists of hexagonal (Al,Ti)N in the (110) orientation (see Figure 6.53). After annealing, a fcc-(Ti,Al)N phase is also present, which first formed at around 700 °C. This precipitation led to an increased content of Al in the matrix, visible by the small right shift of the (110) peak. Further, other orientations of the hexagonal phase appeared: (100), (103) and (200). The preferred plane of (Ti,Al)N is (220) because of the orientation relation with the hexagonal matrix, but also the (311) orientation can be observed. Based on the diffractograms and the surface after cooling (see Figure 6.48), the coating does not appear to have been subjected to stresses and the surface remained intact.

Die approbierte gedruckte Originalversion dieser Diplomarbeit ist an der TU Wien Bibliothek verfügbar
The approved original version of this thesis is available in print at TU Wien Bibliothek.
TU WIEN Bibliothek Your knowledge hub

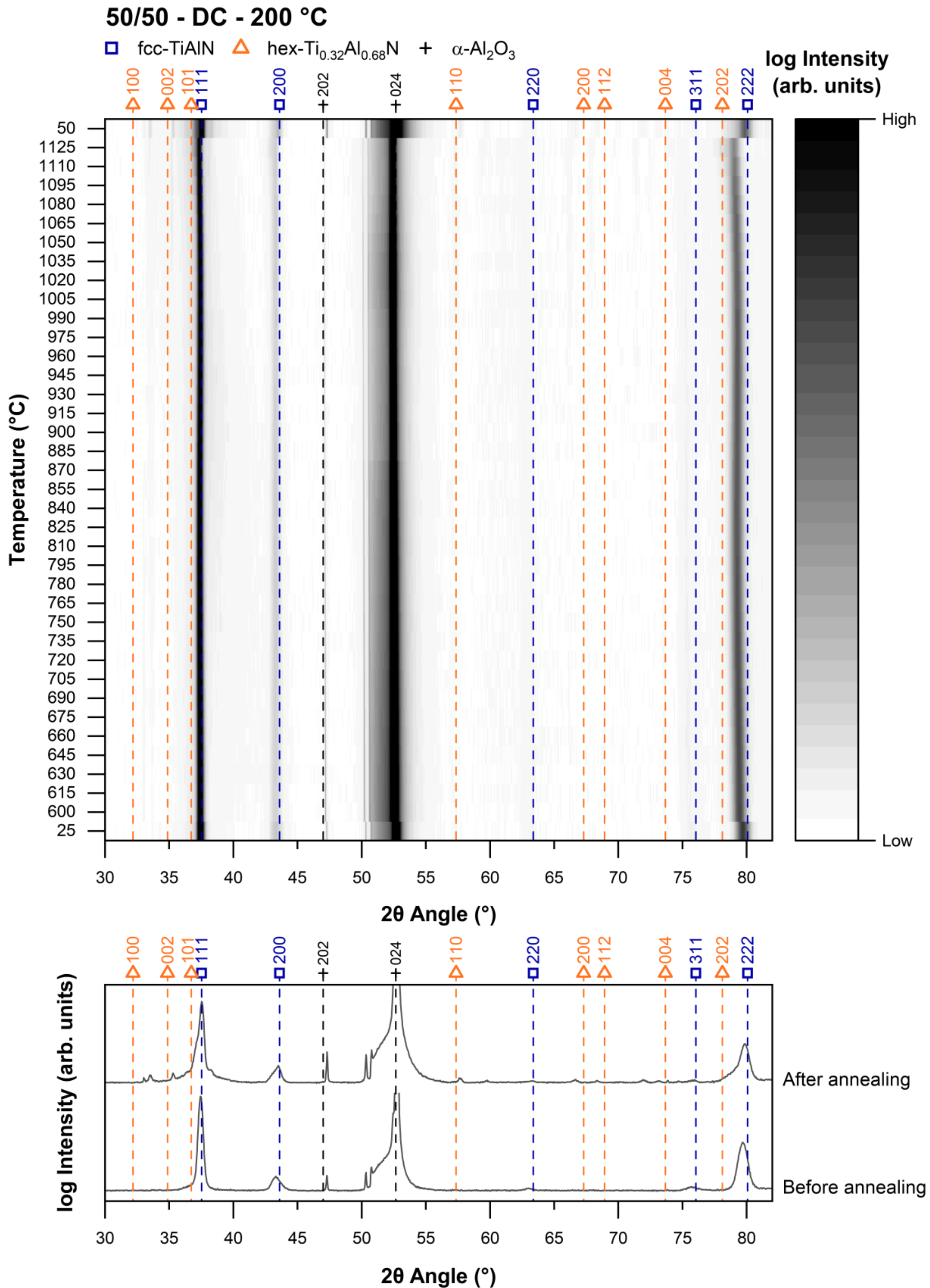

Figure 6.49. Evolution of the crystal structure during annealing from 600 °C to 1125 °C and diffractograms before and after annealing (sample: 50/50 target, DC mode, 200 °C). The cubic Ti-Al-N solid solution forms Ti-rich and Al-rich regions.

Die approbierte gedruckte Originalversion dieser Diplomarbeit ist an der TU Wien Bibliothek verfügbar
The approved original version of this thesis is available in print at TU Wien Bibliothek.
TU WIEN Bibliothek Your knowledge hub

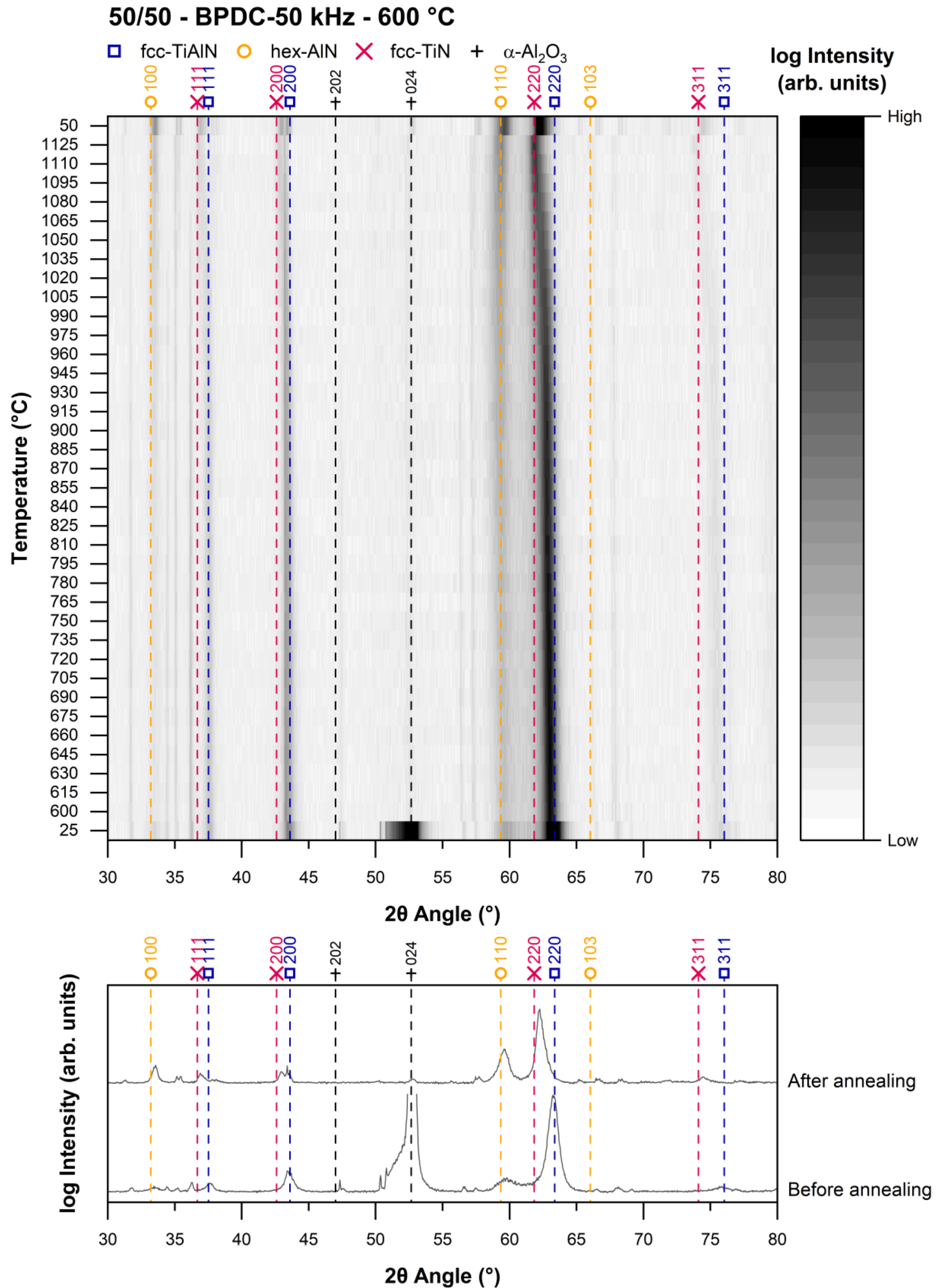

Figure 6.50. Evolution of the crystal structure during annealing from 600 °C to 1125 °C and diffractograms before and after annealing (sample: 50/50 target, BPDC-50 mode, 600 °C). Hexagonal (Al,Ti)N precipitates from the cubic Ti-Al-N matrix, making it richer in Ti.

Die approbierte gedruckte Originalversion dieser Diplomarbeit ist an der TU Wien Bibliothek verfügbar
The approved original version of this thesis is available in print at TU Wien Bibliothek.
TU WIEN Bibliothek Your knowledge hub

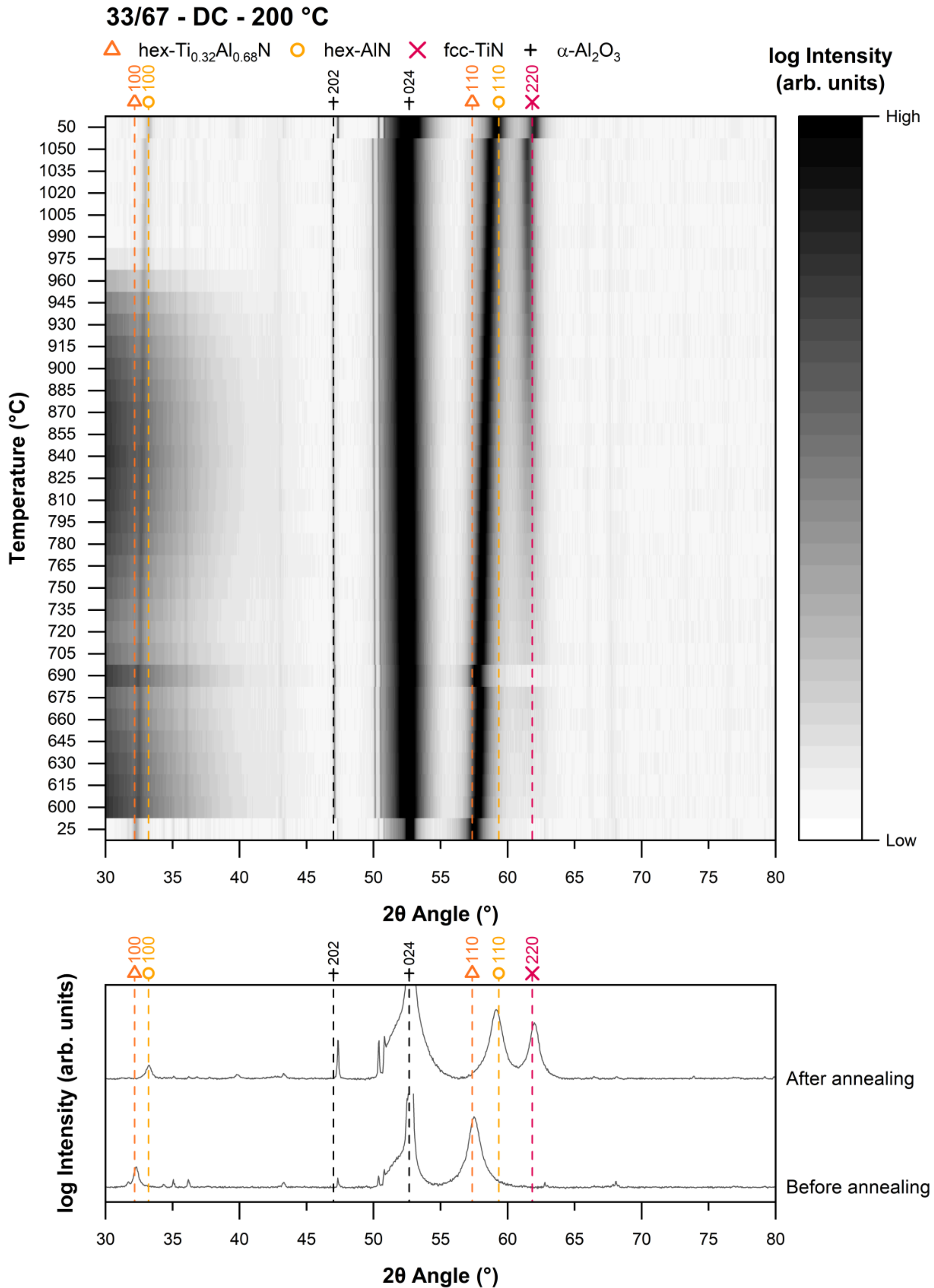

Figure 6.51. Evolution of the crystal structure during annealing from 600 °C to 1050 °C and diffractograms before and after annealing (sample: 33/67 target, DC mode, 200 °C). The hexagonal Ti-Al-N solid solution decomposes into hexagonal AlN and fcc-TiN.

Die approbierte gedruckte Originalversion dieser Diplomarbeit ist an der TU Wien Bibliothek verfügbar
The approved original version of this thesis is available in print at TU Wien Bibliothek.
TU WIEN Bibliothek Your knowledge hub

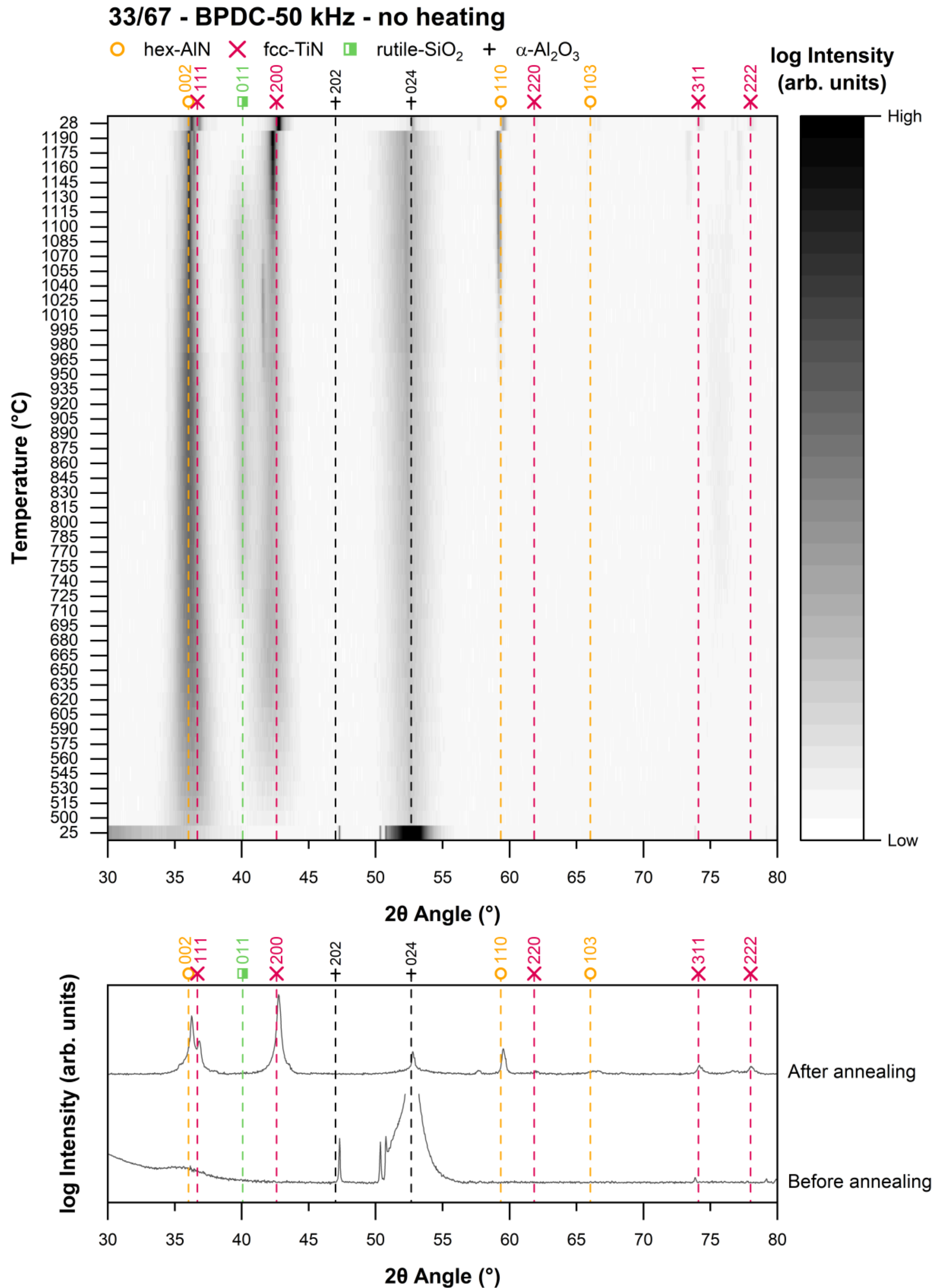

Figure 6.52. Evolution of the crystal structure during annealing from 500 °C to 1190 °C and diffractograms before and after annealing (sample: 33/67 target, BPDC-50 mode, no heating). Hexagonal AlN and fcc-TiN form from the X-ray amorphous matrix and SiO_2 (here in rutile structure) occurs between approximately 700 °C and 1150 °C.

Die approbierte gedruckte Originalversion dieser Diplomarbeit ist an der TU Wien Bibliothek verfügbar
The approved original version of this thesis is available in print at TU Wien Bibliothek.
TU WIEN Bibliothek Your knowledge hub

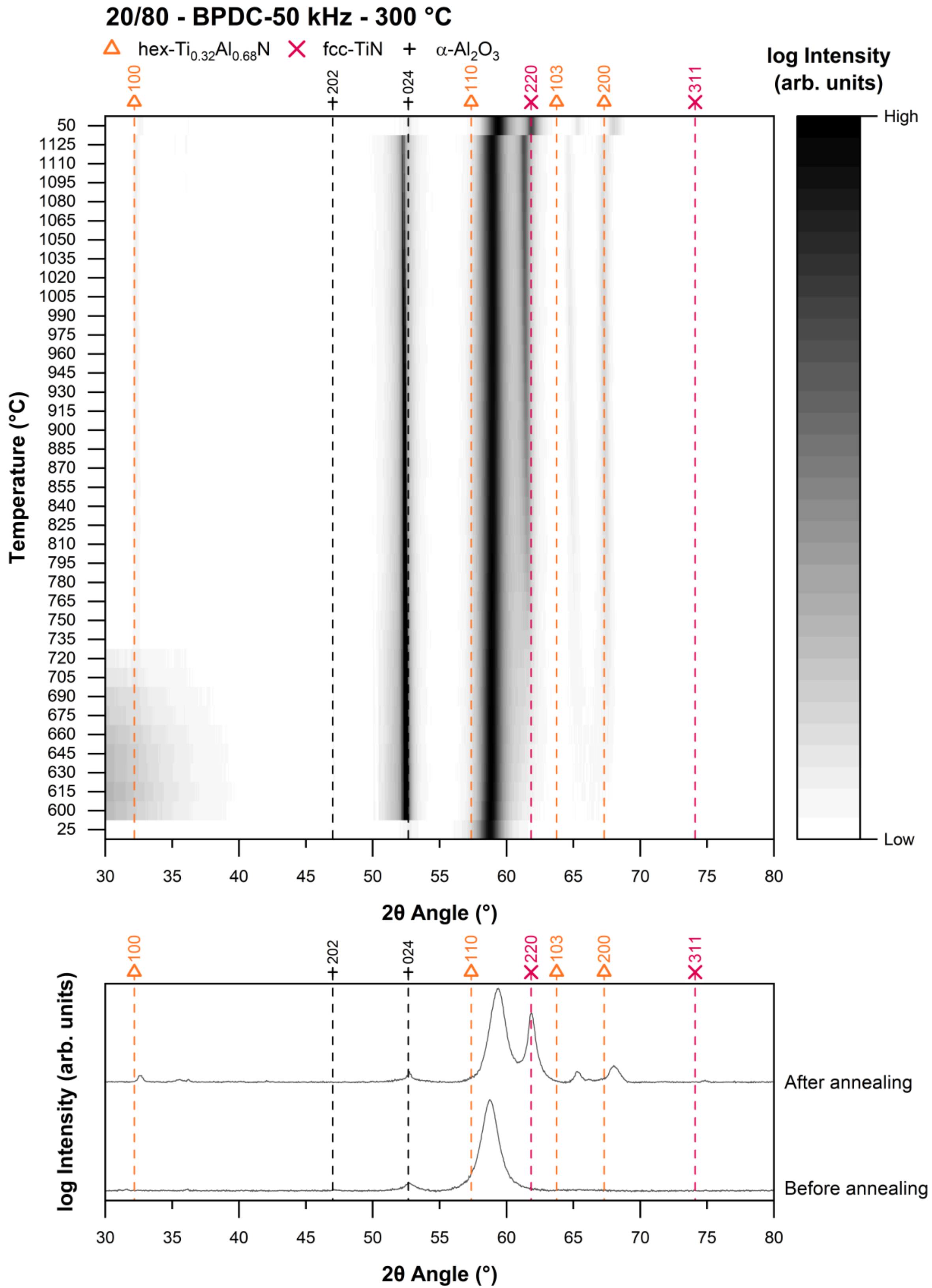

Figure 6.53. Evolution of the crystal structure during annealing from 600 °C to 1125 °C and diffractograms before and after annealing (sample: 20/80 target, BPDC-50 mode, 300 °C). The fcc-(Ti,Al)N phase precipitates from the hexagonal Ti-Al-N matrix, making it richer in Al.

Die approbierte gedruckte Originalversion dieser Diplomarbeit ist an der TU Wien Bibliothek verfügbar
The approved original version of this thesis is available in print at TU Wien Bibliothek.
TU WIEN Bibliothek Your knowledge hub

6.6.3 Mechanical Properties after Annealing

As some of the samples which were annealed showed a noticeable change of the crystal structure, the mechanical properties after annealing were also examined (see Figure 6.54).

The coating produced from the 50/50 target with the DC mode at 200 °C first showed a hardness of 30.47 GPa but experienced a significant decrease to 15.17 GPa during annealing. The elastic modulus behaves contrarily and showed an increasing value from 405 GPa to 467 GPa. Since the corresponding diffractograms (see Figure 6.49) do not reveal a considerable change of the crystal structure, the hardness decrease may be explained with the high number of surface cracks or other surface damages such as macro-spalling (see Figure 6.43). This led to a distorted result during nanoindentation measurements because the indented material has less support from the surroundings and can only withstand smaller forces.

For another coating of the same target but deposited with the BPDC-50 mode at 600 °C, both the hardness (from 38.21 GPa to 25.31 GPa) and elastic modulus (from 504 GPa to 293 GPa) decrease. The diffractograms (see Figure 6.50) show that the amount of the hexagonal phase is increasing during the annealing which may explain the drop, among others. Furthermore, the surface was significantly altered by the annealing test, mainly due to micro-spalling (see Figure 6.44), also resulting in distorted nanoindentation results as mentioned above.

On the contrary, both the hardness and the elastic modulus values of the next sample (33/67 target, DC mode, 200 °C) increase from 20.09 GPa to 28.29 GPa and 190 GPa to 329 GPa, respectively. The pure hexagonal solid solution decomposes into hexagonal AlN with the (110) plane and fcc-TiN with the (220) plane (see the diffractograms in Figure 6.51). Especially the (220) orientation results in high hardness values (see Chapter 6.5), which might be the reason for this increase. The surface shows no obvious signs of cracking or similar surface damages (see Figure 6.45).

However, with the next coating (33/67 target, BPDC-50 mode, no additional heating), there is again a slight drop in hardness from 15.99 GPa to 14.96 GPa, but the elastic modulus value rises from 179 GPa to 279 GPa. Although the crystallinity increases significantly during annealing (see the diffractograms in Figure 6.52), this is not reflected in the hardness values. The main reason for this could be on the one hand the formed preferred orientations (002) of the hexagonal AlN and (200) of fcc-TiN. The latter is often associated with lower hardness values (see Chapter 6.5), which can also be observed in this case. On the other hand, the surface

TU Bibliothek, WIEN Your knowledge hub
Die approbierte gedruckte Originalversion dieser Diplomarbeit ist an der TU Wien Bibliothek verfügbar
The approved original version of this thesis is available in print at TU Wien Bibliothek.

experienced many superficial cracks (see Figure 6.46 and Figure 6.47), which can also explain the low hardness values because of the lower support from the surroundings.

For the last sample examined (20/80 target, BPDC-50 mode, 300 °C), precipitation of fcc-TiN from a hexagonal solid solution resulted in an increase in both the hardness (from 21.25 GPa to 27.09 GPa) and elastic modulus values (from 202 GPa to 292 GPa). Here, the preferred orientations are (110) for the hexagonal phase and (220) for fcc-TiN, leading to this increase (see Chapter 6.5). Furthermore, this coating shows no pronounced cracks in the surface (see Figure 6.48).

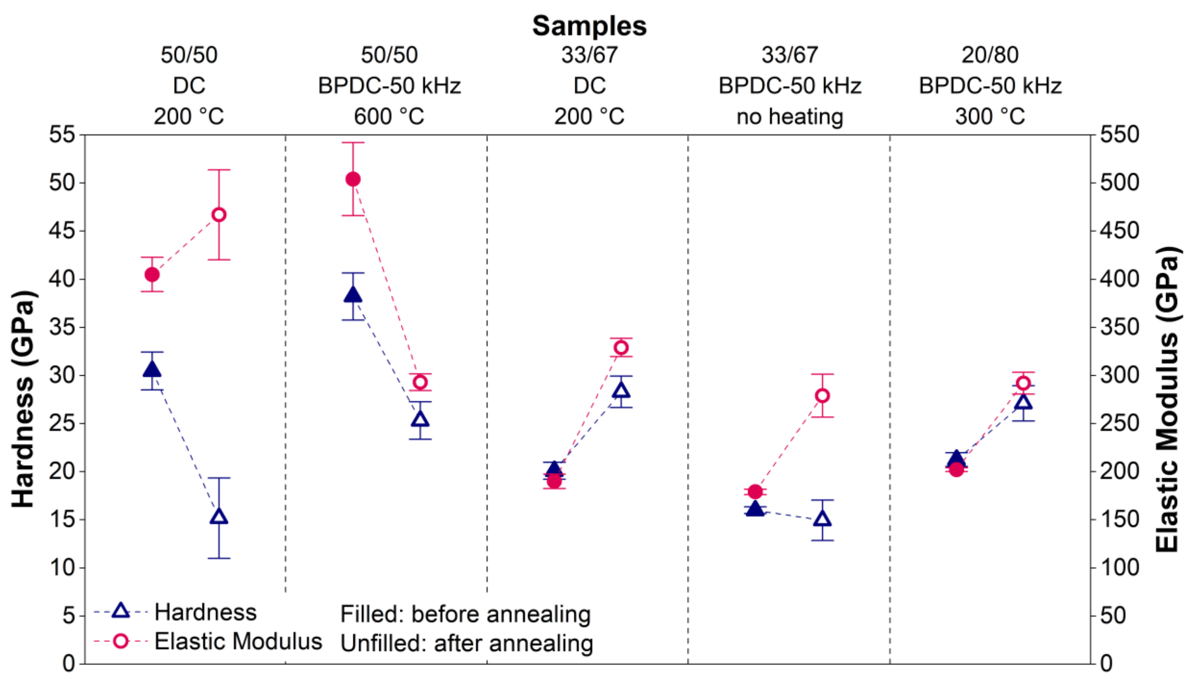

Figure 6.54. Hardness and Elastic Modulus in GPa for chosen samples before and after annealing.

Die approbierte gedruckte Originalversion dieser Diplomarbeit ist an der TU Wien Bibliothek verfügbar
The approved original version of this thesis is available in print at TU Wien Bibliothek.
TU Bibliothek WIEN Your knowledge hub

7 Summary and Conclusion

Deposition Rate

In general, the 50/50 target leads to the highest deposition rates of the whole test series. This is because of its better electrical conductivity compared to the other targets, which allows more power to be applied, especially with the DC mode. The higher the aluminum content in the target, the more suitable the BPDC modes are. Pulsing can neutralize the positive charge build-up and thus can be performed at higher powers than the direct current mode. This is especially true for the 20/80 target and the BPDC mode with 250 kHz.

Analysis of the Cross Section

The microstructure of the produced thin films depends highly on whether a single- or a multiphase system develops, resulting in either a more columnar or a more globular structure. In multiphase systems, the growth of each phase interferes with the growth of every other phase which leads to smaller grains and less directed growth like in a columnar structure. Furthermore, the combination of low electrical conductivity of the target and low temperature or no additional heating of the substrates results in coatings which show no pronounced structures.

Chemical Composition

The sputter mode has the most noticeable influence on the chemical composition of the coatings. With the DC and BPDC-50 modes, the differences in the angular distribution of Al and Ti predominate. Since the probability of sputtered atoms moving towards the substrates is higher for Al than for Ti, it is overstoichiometric in the coatings compared to the target concentrations. The BPDC-250 mode, on the other hand, led to an overstoichiometry of Ti as the high pulse frequency can cause an increase in pressure of the process gas above the target. As a result, the lighter Al atoms are deflected more often than the heavier Ti atoms and more Ti can reach the substrates. Furthermore, the ionization rate is increased which makes it more likely that the ions will bombard the substrates (because of the negative bias) and re-sputtering of especially the lighter Al will occur. While the samples of the DC and the BPDC-50 mode do not show a dependency of the concentration on the temperature, the Ti content increases and the Al content decreases in the coatings with rising temperature for the BPDC-250 mode – probably due to evaporation at the substrate, significantly enhanced by re-sputtering. In contrast to the EDX measurements, the EELS as well as the ERDA results reveal that N is understoichiometric because it is the lightest element of the present material system and thus

Die approbierte gedruckte Originalversion dieser Diplomarbeit ist an der TU Wien Bibliothek verfügbar
The approved original version of this thesis is available in print at TU Wien Bibliothek.
TU WIEN Bibliothek Your knowledge hub

more often deflected. The ERDA measurements also showed that a non-negligible amount of oxygen can be found in the coatings, which presumably originated from the targets.

Crystallographic Properties

As expected, coatings with Ti-rich fcc-(Ti,Al)N as the main phase were produced with the 50/50 target. Due to the high oxygen content, the preferred lattice plane was (111), but it changed to (220) when a second, Al-rich and hexagonal (Al,Ti)N phase appeared in the (110) orientation. Only one other test series showed this structure, which was produced with the 33/67 target and the BPDC-250 mode. In all other samples the Al-rich hexagonal (Al,Ti)N solid solution phase is either the main phase or the only phase at all. Using the targets 33/67 and 20/80 also led to the formation of X-ray amorphous coatings when the substrates were not additionally heated and in general resulted in smaller sized grains compared to thin films from the 50/50 target. Furthermore, the results show that almost all coatings are under compressive stresses, regardless of the target used to produce them.

The TEM results confirm not only the findings of the diffractogram analysis, but also the conclusions drawn from the SEM images of the cross sections.

Mechanical Properties

The hardest coatings were produced with the 50/50 target, as one would expect, since their grains mainly show the fcc structure. The highest hardness value of 38.21 GPa was measured on the 50/50-BPDC-50 (600 °C) sample, in which a beneficial amount of hexagonal (Al,Ti)N phase precipitated. For comparison, in the 50/50-DC coating the hexagonal phase can also be found, but in a higher proportion and the hardness is lower (31.94 GPa). The coatings from the 33/67 and 20/80 targets show much lower hardness values (maximum: 29.91 GPa), but they behave very similar with rising temperatures. It became apparent that the hardness values mainly depend on the crystal structure as the chemical composition hardly changes within a test series. In general, for high hardness, the (220) and (111) planes of the cubic phase have been found to be beneficial, as well as the (110) and (103) of the hexagonal phase. In addition, the presence of a second phase in the right amount, whether a hexagonal one in a cubic matrix or vice versa, increased the strains of the crystal lattice and subsequently the hardness. On the other hand, the cubic (200) plane and X-ray amorphous structures or very small grains were particularly unfavorable for a high hardness.

TU Bibliothek WIEN Your knowledge hub
Die approbierte gedruckte Originalversion dieser Diplomarbeit ist an der TU Wien Bibliothek verfügbar
The approved original version of this thesis is available in print at TU Wien Bibliothek.

Thermal Stability

Some of the coatings experienced high stresses either during annealing or subsequent cooling, resulting in surface damage such as cracks, macro- or micro-spalling. The exact reason for the occurrence of each crack evolution could not be determined in the scope of this project. Looking at the diffractograms of the 50/50 target, a hexagonal phase could only be identified in the cubic matrix if it was already present before the annealing. Otherwise, there appeared just inconclusive peaks. These coatings also experienced high stresses and thus macro- and micro-spalling and cracking, which distorted the hardness results. The samples produced with the 33/67 target either decomposed from a hexagonal (Al,Ti)N solid solution phase or crystallized from an X-ray amorphous phase into hexagonal AlN or cubic TiN. In the first case, the planes (110) and (220), respectively, which are preferred for high hardness, were preserved and the hardness increased. In the other case, the planes (002) and (200), respectively, formed, resulting in a slight decrease in hardness. However, this coating cracked multiple times and the hardness result is thus distorted. The last sample was produced with the 20/80 target and did not show a complete decomposition of the hexagonal solid solution phase, but precipitation of fcc-(Ti,Al)N. Both phases occur in (110) and (220) planes, respectively, and the coating remained intact, thus a hardness increase was observed.

Outlook

The experiments and their evaluation resulted in a baseline for further investigations. For example, the sample with the highest hardness will be reproduced with different parameters to determine whether this hardness can be exceeded, or other properties can be improved. These parameters could be higher power, higher substrate temperatures, different pulse frequencies or times, different bias potentials and/or additional gas supply of H_2 or N_2. The latter should either reduce oxides or compensate for understoichiometry, respectively. If the opportunity arises, additional coatings will be examined with ERDA to verify the results of the EDX measurements and to determine if there is a dependency of the crystal structure on the nitrogen content in the thin films. Furthermore, a follow-up project will focus on the deposition of all three target compositions using high impulse magnetron sputtering (HIPIMS).

TU WIEN Bibliothek Your knowledge hub
Die approbierte gedruckte Originalversion dieser Diplomarbeit ist an der TU Wien Bibliothek verfügbar
The approved original version of this thesis is available in print at TU Wien Bibliothek.

References

[1] D. M. Mattox, *Handbook of Physical Vapor Deposition (PVD) Processing*. William Andrew, 2010.

[2] J.-E. Sundgren, “Structure and properties of TiN coatings,” *Thin Solid Films*, vol. 128, no. 1–2, pp. 21–44, Jun. 1985, doi: 10.1016/0040-6090(85)90333-5.

[3] O. Knotek, M. Böhmer, and T. Leyendecker, “On structure and properties of sputtered Ti and Al based hard compound films,” *Journal of Vacuum Science & Technology A*, vol. 4, no. 6, pp. 2695–2700, Nov. 1986, doi: 10.1116/1.573708.

[4] S. PalDey and S. C. Deevi, “Single layer and multilayer wear resistant coatings of (Ti,Al)N: a review,” *Materials Science and Engineering: A*, vol. 342, no. 1, pp. 58–79, Feb. 2003, doi: 10.1016/S0921-5093(02)00259-9.

[5] P. H. Mayrhofer *et al.*, “Self-organized nanostructures in the Ti–Al–N system,” *Applied Physics Letters*, vol. 83, no. 10, pp. 2049–2051, Sep. 2003, doi: 10.1063/1.1608464.

[6] L. Chen, M. Moser, Y. Du, and P. H. Mayrhofer, “Compositional and structural evolution of sputtered Ti-Al-N,” *Thin Solid Films*, vol. 517, no. 24, pp. 6635–6641, Oct. 2009, doi: 10.1016/j.tsf.2009.04.056.

[7] J. W. Cahn, “On spinodal decomposition,” *Acta Metallurgica*, vol. 9, no. 9, pp. 795–801, Sep. 1961, doi: 10.1016/0001-6160(61)90182-1.

[8] S. Liu *et al.*, “Modeling of metastable phase formation for sputtered Ti1-xAlxN thin films,” *Acta Materialia*, vol. 165, pp. 615–625, Feb. 2019, doi: 10.1016/j.actamat.2018.12.004.

[9] J. Zhou *et al.*, “Phase equilibria, thermodynamics and microstructure simulation of metastable spinodal decomposition in c–Ti1−xAlxN coatings,” *Calphad*, vol. 56, pp. 92–101, Mar. 2017, doi: 10.1016/j.calphad.2016.12.006.

[10] P. H. Mayrhofer, “Oberflächentechnik/Surface Technology 308.875 Summer term 2022,” Wien, 2022.

[11] S. K. U. Cepheiden, *Deutsch: Schematischer Aufbau des Magnetonsputterns: Im ersten Schritt werden die Argonatome durch das Plasma ionisiert und auf das Target beschleunigt. Dadurch werden Targetionen herausgeschlagen, die aufgrund ihrer Ladung zum Substrat fliegen und sich dort anlagern.* 2008. Accessed: Jun. 09, 2023. [Online]. Available: https://commons.wikimedia.org/wiki/File:Schema_Magnetonsputtern.svg

[12] H. C. Barshilia, A. Ananth, J. Khan, and G. Srinivas, “Ar + H2 plasma etching for improved adhesion of PVD coatings on steel substrates,” *Vacuum*, vol. 86, no. 8, pp. 1165–1173, Feb. 2012, doi: 10.1016/j.vacuum.2011.10.028.

[13] L. B. Freund and S. Suresh, *Thin Film Materials: Stress, Defect Formation and Surface Evolution*. Cambridge: Cambridge University Press, 2004. doi: 10.1017/CBO9780511754715.

[14] A. at E. Wikipedia, *English: 薄膜生长模式*. 2007. Accessed: Jun. 14, 2023. [Online]. Available: https://commons.wikimedia.org/wiki/File:GrowthModes.png?uselang=en#Licensing

[15] A. Anders, “A structure zone diagram including plasma-based deposition and ion etching,” *Thin Solid Films*, vol. 518, no. 15, pp. 4087–4090, May 2010, doi: 10.1016/j.tsf.2009.10.145.

[16] A. Dey and A. K. Mukhopadhyay, *Nanoindentation of Brittle Solids*, no. ISBN: 9781466596900. Baton Rouge: Baton Rouge: CRC Press, 2014. doi: 10.1201/b17110.

Die approbierte gedruckte Originalversion dieser Diplomarbeit ist an der TU Wien Bibliothek verfügbar
The approved original version of this thesis is available in print at TU Wien Bibliothek.
TU Bibliothek WIEN Your knowledge hub

[17] A. C. Fischer-Cripps, "Critical review of analysis and interpretation of nanoindentation test data," *Surface and Coatings Technology*, vol. 200, no. 14, pp. 4153–4165, Apr. 2006, doi: 10.1016/j.surfcoat.2005.03.018.
[18] H. Bückle, *Mikrohärteprüfung und ihre Anwendung*. Stuttgart: Berliner Union, 1965.
[19] M. Hans *et al.*, "Stress-Dependent Elasticity of TiAlN Coatings," *Coatings*, vol. 9, no. 1, Art. no. 1, Jan. 2019, doi: 10.3390/coatings9010024.
[20] L. Spieß, G. Teichert, R. Schwarzer, H. Behnken, and C. Genzel, *Moderne Röntgenbeugung: Röntgendiffraktometrie für Materialwissenschaftler, Physiker und Chemiker*. Wiesbaden: Springer Fachmedien Wiesbaden, 2019. doi: 10.1007/978-3-8348-8232-5.
[21] Hydrargyrum, *English: Bragg diffraction from a cubic crystal lattice. Plane waves incident on a crystal lattice at angle*. 2011. Accessed: May 14, 2023. [Online]. Available: https://commons.wikimedia.org/wiki/File:Bragg_diffraction_2.svg
[22] F. Feret, D. Roy, and C. Boulanger, "Determination of alpha and beta alumina in ceramic alumina by X-ray diffraction," *Spectrochimica Acta Part B: Atomic Spectroscopy*, vol. 55, pp. 1051–1061, Jul. 2000, doi: 10.1016/S0584-8547(00)00225-1.
[23] R. Allmann, *Röntgen-Pulverdiffraktometrie*, 2nd ed. Berlin, Heidelberg: Springer Berlin Heidelberg, 2003. doi: 10.1007/978-3-642-56079-8.
[24] E. Abbe, "Beiträge zur Theorie des Mikroskops und der mikroskopischen Wahrnehmung," *Archiv f. mikrosk. Anatomie*, vol. 9, no. 1, pp. 413–468, Dec. 1873, doi: 10.1007/BF02956173.
[25] M. Knoll and E. Ruska, "Das Elektronenmikroskop," *Z. Physik*, vol. 78, no. 5, pp. 318–339, May 1932, doi: 10.1007/BF01342199.
[26] J. I. Goldstein, D. E. Newbury, J. R. Michael, N. W. M. Ritchie, J. H. J. Scott, and D. C. Joy, *Scanning Electron Microscopy and X-Ray Microanalysis*. New York, NY, UNITED STATES: Springer New York, 2017. Accessed: May 04, 2023. [Online]. Available: http://ebookcentral.proquest.com/lib/viennaut/detail.action?docID=6314883
[27] S. J. B. Reed, *Electron Microprobe Analysis and Scanning Electron Microscopy in Geology*, 2nd ed. Cambridge: Cambridge University Press, 2005. doi: 10.1017/CBO9780511610561.
[28] Ponor, *English: Teardrop-shaped electron–matter interaction volume and limits to the depths from which each signal type can be emitted or detected.* 2020. Accessed: May 14, 2023. [Online]. Available: https://commons.wikimedia.org/wiki/File:Electron-matter_interaction_volume_and_various_types_of_signal_generated_-_v2.svg
[29] Mglg, *Conceptual ray diagrams of ideal and spherically aberrated lenses. A perfect lens (top) focuses all incoming rays to a single point on the optic axis, but a real lens with spherical surfaces (bottom) focuses different rays to different points along the optic axis, depending on the radial position of each incoming ray.* 2006. Accessed: May 19, 2023. [Online]. Available: https://commons.wikimedia.org/wiki/File:Spherical_aberration_2.svg
[30] B. Kim and M. F. Hochella, "Chapter 4 - Analytical Transmission Electron Microscopy and Scanning Transmission Electron Microscopy Techniques for the Characterization of Nanomaterial Composition, Phase and Crystallinity," in *Frontiers of Nanoscience*, vol. 8, M. Baalousha and J. R. Lead, Eds., in Characterization of Nanomaterials in Complex Environmental and Biological Media, vol. 8. , Elsevier, 2015, pp. 123–152. doi: 10.1016/B978-0-08-099948-7.00004-X.
[31] M. De Graef, *Introduction to Conventional Transmission Electron Microscopy*. Cambridge: Cambridge University Press, 2003. doi: 10.1017/CBO9780511615092.
[32] N. Marturi, "Vision and visual servoing for nanomanipulation and nanocharacterization in scanning electron microscope.," Nov. 2013.

TU Bibliothek Your knowledge hub WIEN
Die approbierte gedruckte Originalversion dieser Diplomarbeit ist an der TU Wien Bibliothek verfügbar
The approved original version of this thesis is available in print at TU Wien Bibliothek.

[33] Klingm01, *Čeština: Porovnání STEMových snímků mikrostruktury zachycených různými detektory - BF, ADF a HAADF*. 2021. Accessed: May 21, 2023. [Online]. Available: https://commons.wikimedia.org/wiki/File:STEM_detectors.png
[34] M. Klinger, *CrysTBox - Crystallographic Toolbox*. Prague: Institute of Physics of the Czech Academy of Sciences, 2015. [Online]. Available: http://www.fzu.cz/~klinger/crystbox.pdf
[35] Albert Thompson *et al.*, *X-Ray Data Booklet*, 3rd ed. in Center for X-Ray Optics and Advanced Light Sources. Berkeley: University of California, Lawrence Berkeley National Laboratory, 2009. Accessed: May 18, 2023. [Online]. Available: https://xdb.lbl.gov/xdb-new.pdf
[36] G. Friedbacher and H. Bubert, *Surface and Thin Film Analysis: A Compendium of Principles, Instrumentation, and Applications*, Second. Weinheim, Germany: Wiley-VCH Verlag GmbH & Co. KGaA, 2011. Accessed: Jun. 09, 2023. [Online]. Available: https://onlinelibrary.wiley.com/doi/epub/10.1002/9783527636921
[37] Yu. V. Martynenko, A. V. Rogov, and V. I. Shul'ga, "Angular distribution of atoms during the magnetron sputtering of polycrystalline targets," *Tech. Phys.*, vol. 57, no. 4, pp. 439–444, Apr. 2012, doi: 10.1134/S1063784212040196.
[38] H. Riedl *et al.*, "Influence of oxygen impurities on growth morphology, structure and mechanical properties of Ti–Al–N thin films," *Thin Solid Films*, vol. 603, pp. 39–49, Mar. 2016, doi: 10.1016/j.tsf.2016.01.039.
[39] L. Zauner *et al.*, "Reactive HiPIMS deposition of Ti-Al-N: Influence of the deposition parameters on the cubic to hexagonal phase transition," *Surface and Coatings Technology*, vol. 382, p. 125007, Jan. 2020, doi: 10.1016/j.surfcoat.2019.125007.
[40] D. Gall, S. Kodambaka, M. A. Wall, I. Petrov, and J. E. Greene, "Pathways of atomistic processes on TiN(001) and (111) surfaces during film growth: an ab initio study," *Journal of Applied Physics*, vol. 93, no. 11, pp. 9086–9094, May 2003, doi: 10.1063/1.1567797.
[41] B. E. Deal and A. S. Grove, "General Relationship for the Thermal Oxidation of Silicon," *Journal of Applied Physics*, vol. 36, no. 12, pp. 3770–3778, Jul. 2004, doi: 10.1063/1.1713945.

Die approbierte gedruckte Originalversion dieser Diplomarbeit ist an der TU Wien Bibliothek verfügbar
The approved original version of this thesis is available in print at TU Wien Bibliothek.
TU WIEN Bibliothek Your knowledge hub

Appendices

This section lists additional data and images that are either presented in figures or have not been shown in this paper for reasons of clarity.

Die approbierte gedruckte Originalversion dieser Diplomarbeit ist an der TU Wien Bibliothek verfügbar
The approved original version of this thesis is available in print at TU Wien Bibliothek.
TU WIEN Bibliothek Your knowledge hub

Table A. 1. Process parameters of the 50/50 Target

Number	Target	Sputter Mode	Substrate Temperature	Argon Gasflow	Pressure	Bias	Amperage	Power	Voltage	Target-Substrate Distance	Time
			(°C)	(sscm)	(mbar)	(V)	(A)	(W)	(V)	(mm)	(min)
1	$Ti_{0.5}Al_{0.5}N$	DC	0	35.4	0.004	-50	1.00	430	430	39	60
2	$Ti_{0.5}Al_{0.5}N$	DC	200	35.4	0.004	-50	1.00	434	434	39	60
3	$Ti_{0.5}Al_{0.5}N$	DC	300	35.4	0.004	-50	1.00	432	432	39	60
4	$Ti_{0.5}Al_{0.5}N$	DC	450	32.0	0.004	-50	1.00	437	437	39	60
5	$Ti_{0.5}Al_{0.5}N$	DC	600	33.0	0.004	-50	1.00	390	390	39	25
6	$Ti_{0.5}Al_{0.5}N$	BPDC-50	0	35.0	0.004	-50	1.00	380	380	39	60
7	$Ti_{0.5}Al_{0.5}N$	BPDC-50	200	34.8	0.004	-50	1.00	380	380	39	60
8	$Ti_{0.5}Al_{0.5}N$	BPDC-50	300	34.9	0.004	-50	1.01	380	376	39	60
9	$Ti_{0.5}Al_{0.5}N$	BPDC-50	450	35.0	0.004	-50	0.94	380	404	39	60
10	$Ti_{0.5}Al_{0.5}N$	BPDC-50	600	33.6	0.004	-50	1.00	380	380	39	60
11	$Ti_{0.5}Al_{0.5}N$	BPDC-250	0	34.9	0.004	-50	1.17	300	256	39	60
12	$Ti_{0.5}Al_{0.5}N$	BPDC-250	200	34.6	0.004	-50	1.16	300	259	39	60
13	$Ti_{0.5}Al_{0.5}N$	BPDC-250	300	35.0	0.004	-50	1.14	300	263	39	60
14	$Ti_{0.5}Al_{0.5}N$	BPDC-250	450	33.0	0.004	-50	1.16	300	259	39	45
15	$Ti_{0.5}Al_{0.5}N$	BPDC-250	600	34.0	0.004	-50	1.14	300	263	39	45

Die approbierte gedruckte Originalversion dieser Diplomarbeit ist an der TU Wien Bibliothek verfügbar
The approved original version of this thesis is available in print at TU Wien Bibliothek.
TU WIEN Bibliothek Your knowledge hub

Die approbierte gedruckte Originalversion dieser Diplomarbeit ist an der TU Wien Bibliothek verfügbar
The approved original version of this thesis is available in print at TU Wien Bibliothek.

Table A. 2. Process parameters of the 33/67 target

Number	Target	Sputter Mode	Substrate Temperature (°C)	Argon Gasflow (sscm)	Pressure (mbar)	Bias (V)	Amperage (A)	Power (W)	Voltage (V)	Target-Substrate Distance (mm)	Time (min)
16	$Ti_{0.33}Al_{0.67}N$	DC	0	35.4	0.004	-50	0.60	283	472	39	60
17	$Ti_{0.33}Al_{0.67}N$	DC	200	35.4	0.004	-50	0.60	295	492	39	60
18	$Ti_{0.33}Al_{0.67}N$	DC	300	35.4	0.004	-50	0.60	300	500	39	60
19	$Ti_{0.33}Al_{0.67}N$	DC	450	35.4	0.004	-50	0.60	291	485	39	60
20	$Ti_{0.33}Al_{0.67}N$	DC	600	35.4	0.004	-50	0.60	301	502	39	60
21	$Ti_{0.33}Al_{0.67}N$	BPDC-50	0	35.0	0.004	-50	0.48	250	521	39	60
22	$Ti_{0.33}Al_{0.67}N$	BPDC-50	200	34.8	0.004	-50	0.50	250	500	39	60
23	$Ti_{0.33}Al_{0.67}N$	BPDC-50	300	35.4	0.004	-50	0.49	250	510	39	60
24	$Ti_{0.33}Al_{0.67}N$	BPDC-50	450	34.8	0.004	-50	0.49	250	510	39	60
25	$Ti_{0.33}Al_{0.67}N$	BPDC-50	600	34.4	0.004	-50	0.51	250	490	39	60
26	$Ti_{0.33}Al_{0.67}N$	BPDC-250	0	35.2	0.004	-50	0.98	300	306	39	60
27	$Ti_{0.33}Al_{0.67}N$	BPDC-250	200	35.2	0.004	-50	0.98	300	306	39	60
28	$Ti_{0.33}Al_{0.67}N$	BPDC-250	300	35.4	0.004	-50	0.96	300	313	39	60
29	$Ti_{0.33}Al_{0.67}N$	BPDC-250	450	34.7	0.004	-50	0.97	300	309	39	60
30	$Ti_{0.33}Al_{0.67}N$	BPDC-250	600	34.6	0.004	-50	0.98	300	306	39	60

Table A. 3. Process parameters of the 20/80 target

Number	Target	Sputter Mode	Substrate Temperature (°C)	Argon Gasflow (sscm)	Pressure (mbar)	Bias (V)	Amperage (A)	Power (W)	Voltage (V)	Target-Substrate Distance (mm)	Time (min)
31	$Ti_{0.2}Al_{0.8}N$	DC	0	36.0	0.004	-50	0.25	172	688	39	60
32	$Ti_{0.2}Al_{0.8}N$	DC	200	36.0	0.004	-50	0.25	172	688	39	75
33	$Ti_{0.2}Al_{0.8}N$	DC	300	36.0	0.004	-50	0.25	173	692	39	90
34	$Ti_{0.2}Al_{0.8}N$	DC	450	35.0	0.004	-50	0.25	174	696	39	60
35	$Ti_{0.2}Al_{0.8}N$	DC	600	35.0	0.004	-50	0.25	172	688	39	60
36	$Ti_{0.2}Al_{0.8}N$	BPDC-50	0	35.4	0.004	-50	0.34	200	588	39	60
37	$Ti_{0.2}Al_{0.8}N$	BPDC-50	200	35.0	0.004	-50	0.34	200	588	39	60
38	$Ti_{0.2}Al_{0.8}N$	BPDC-50	300	35.0	0.004	-50	0.28	200	714	39	90
39	$Ti_{0.2}Al_{0.8}N$	BPDC-50	450	34.7	0.004	-50	0.33	200	606	39	60
40	$Ti_{0.2}Al_{0.8}N$	BPDC-50	600	34.2	0.004	-50	0.33	200	606	39	60
41	$Ti_{0.2}Al_{0.8}N$	BPDC-250	0	35.1	0.004	-50	0.89	300	337	39	60
42	$Ti_{0.2}Al_{0.8}N$	BPDC-250	200	34.8	0.004	-50	0.90	300	333	39	60
43	$Ti_{0.2}Al_{0.8}N$	BPDC-250	300	35.1	0.004	-50	0.90	300	333	39	60
44	$Ti_{0.2}Al_{0.8}N$	BPDC-250	450	34.8	0.004	-50	0.86	300	349	39	60
45	$Ti_{0.2}Al_{0.8}N$	BPDC-250	600	34.2	0.004	-50	0.85	300	353	39	60

TU WIEN Bibliothek Your knowledge hub
Die approbierte gedruckte Originalversion dieser Diplomarbeit ist an der TU Wien Bibliothek verfügbar
The approved original version of this thesis is available in print at TU Wien Bibliothek.

Table A. 4. Values of thickness and deposition rate of all samples

Number	Target	Sputter Mode	Substrate Temperature (°C)	Thickness (µm)	Thickness Standard Error (µm)	Deposition Rate (µm/h)	Deposition Rate Standard Error (µm/h)
1	50/50	DC	0	6.10	0.04	6.10	0.04
2	50/50	DC	200	6.42	0.07	6.42	0.07
3	50/50	DC	300	6.30	0.03	6.30	0.03
4	50/50	DC	450	6.53	0.08	6.53	0.08
5	50/50	DC	600	2.67	0.06	6.40	0.15
6	50/50	BPDC-50	0	5.11	0.05	5.11	0.05
7	50/50	BPDC-50	200	5.42	0.07	5.42	0.07
8	50/50	BPDC-50	300	5.01	0.02	5.01	0.02
9	50/50	BPDC-50	450	5.27	0.05	5.27	0.05
10	50/50	BPDC-50	600	5.06	0.03	5.06	0.03
11	50/50	BPDC-250	0	3.73	0.05	3.73	0.05
12	50/50	BPDC-250	200	3.54	0.02	3.54	0.02
13	50/50	BPDC-250	300	3.63	0.03	3.63	0.03
14	50/50	BPDC-250	450	2.58	0.04	3.43	0.05
15	50/50	BPDC-250	600	0.70	0.02	0.93	0.03
16	33/67	DC	0	5.30	0.10	5.30	0.10
17	33/67	DC	200	4.85	0.08	4.85	0.08
18	33/67	DC	300	4.94	0.02	4.94	0.02
19	33/67	DC	450	4.92	0.32	4.92	0.32
20	33/67	DC	600	4.97	0.11	4.97	0.11
21	33/67	BPDC-50	0	4.19	0.05	4.19	0.05
22	33/67	BPDC-50	200	4.05	0.15	4.05	0.15
23	33/67	BPDC-50	300	3.59	0.27	3.59	0.27
24	33/67	BPDC-50	450	3.69	0.14	3.69	0.14
25	33/67	BPDC-50	600	3.94	0.03	3.94	0.03
26	33/67	BPDC-250	0	3.88	0.08	3.88	0.08
27	33/67	BPDC-250	200	3.88	0.09	3.88	0.09
28	33/67	BPDC-250	300	3.56	0.09	3.56	0.09
29	33/67	BPDC-250	450	3.36	0.14	3.36	0.14
30	33/67	BPDC-250	600	3.63	0.12	3.63	0.12
31	20/80	DC	0	1.47	0.02	1.47	0.02
32	20/80	DC	200	2.10	0.01	1.68	0.01
33	20/80	DC	300	2.33	0.04	1.56	0.02
34	20/80	DC	450	1.29	0.02	1.29	0.02
35	20/80	DC	600	1.27	0.03	1.27	0.03
36	20/80	BPDC-50	0	2.87	0.04	2.87	0.04
37	20/80	BPDC-50	200	2.78	0.23	2.78	0.23
38	20/80	BPDC-50	300	4.26	0.05	4.26	0.03
39	20/80	BPDC-50	450	2.76	0.01	2.76	0.01
40	20/80	BPDC-50	600	2.94	0.02	2.94	0.02
41	20/80	BPDC-250	0	2.60	0.09	2.60	0.09
42	20/80	BPDC-250	200	3.14	0.08	3.14	0.08
43	20/80	BPDC-250	300	2.12	0.01	2.12	0.01
44	20/80	BPDC-250	450	3.17	0.04	3.17	0.04
45	20/80	BPDC-250	600	2.88	0.28	2.88	0.28

Die approbierte gedruckte Originalversion dieser Diplomarbeit ist an der TU Wien Bibliothek verfügbar
The approved original version of this thesis is available in print at TU Wien Bibliothek.
TU WIEN Bibliothek Your knowledge hub

Table A. 5. Values of the EDX measurements

Number	Target	Sputter Mode	Substrate Temperature (°C)	EDX (at%)		
				N	Al	Ti
1	50/50	DC	0	58.73	22.30	18.97
2	50/50	DC	200	58.17	22.29	19.55
3	50/50	DC	300	58.02	22.27	19.70
4	50/50	DC	450	58.30	22.46	19.24
5	50/50	DC	600	60.21	21.38	18.41
6	50/50	BPDC-50	0	58.21	21.93	19.86
7	50/50	BPDC-50	200	57.83	22.43	19.74
8	50/50	BPDC-50	300	58.98	21.98	19.04
9	50/50	BPDC-50	450	58.73	22.03	19.24
10	50/50	BPDC-50	600	58.83	22.01	19.16
11	50/50	BPDC-250	0	58.66	20.08	21.27
12	50/50	BPDC-250	200	59.09	19.68	21.24
13	50/50	BPDC-250	300	59.92	18.83	21.25
14	50/50	BPDC-250	450	61.15	18.52	20.32
15	50/50	BPDC-250	600	61.88	17.58	20.54
16	33/67	DC	0	53.24	32.96	13.80
17	33/67	DC	200	54.55	32.15	13.31
18	33/67	DC	300	53.91	32.40	13.69
19	33/67	DC	450	55.18	32.06	12.76
20	33/67	DC	600	54.27	32.21	13.52
21	33/67	BPDC-50	0	50.55	34.57	14.88
22	33/67	BPDC-50	200	54.16	31.91	13.93
23	33/67	BPDC-50	300	53.54	32.48	13.98
24	33/67	BPDC-50	450	55.47	30.89	13.63
25	33/67	BPDC-50	600	53.91	32.09	14.00
26	33/67	BPDC-250	0	52.11	31.09	16.80
27	33/67	BPDC-250	200	56.58	27.68	15.74
28	33/67	BPDC-250	300	56.45	27.42	16.12
29	33/67	BPDC-250	450	58.29	26.40	15.32
30	33/67	BPDC-250	600	56.50	27.15	16.35
31	20/80	DC	0	50.66	40.44	8.90
32	20/80	DC	200	50.73	40.34	8.92
33	20/80	DC	300	50.08	40.69	9.23
34	20/80	DC	450	47.39	43.28	9.33
35	20/80	DC	600	50.26	40.85	8.89
36	20/80	BPDC-50	0	47.02	43.58	9.40
37	20/80	BPDC-50	200	51.91	39.56	8.53
38	20/80	BPDC-50	300	49.44	41.13	9.44
39	20/80	BPDC-50	450	50.86	40.36	8.78
40	20/80	BPDC-50	600	49.87	41.07	9.06
41	20/80	BPDC-250	0	50.84	38.23	10.93
42	20/80	BPDC-250	200	50.59	38.84	10.57
43	20/80	BPDC-250	300	57.82	32.57	9.61
44	20/80	BPDC-250	450	55.19	33.69	11.13
45	20/80	BPDC-250	600	54.34	34.71	10.95

Die approbierte gedruckte Originalversion dieser Diplomarbeit ist an der TU Wien Bibliothek verfügbar
The approved original version of this thesis is available in print at TU Wien Bibliothek.
TU WIEN Bibliothek Your knowledge hub

Table A. 6. Values of the EELS and ERDA measurements

Number	Target	Sputter Mode	Substrate Temperature (°C)	EELS (at%)			ERDA (at%)			
				N	Al	Ti	N	Al	Ti	O
3	50/50	DC	300				45.39	28.62	24.08	1.91
10	50/50	BPDC-50	600	38.80	30.15	31.05				
19	33/67	DC	450	39.61	41.58	18.81				
22	33/67	BPDC-50	200				42.69	39.29	16.34	1.68
34	20/80	DC	450				39.74	48.28	10.35	1.63
45	20/80	BPDC-250	600	38.03	47.55	14.42				

Table A. 7. Values of the hardness and the elastic modulus after annealing

Number	Target	Sputter Mode	Substrate Temperature (°C)	Hardness (GPa)	Hardness Standard Error (GPa)	Elastic Modulus (GPa)	Elastic Modulus Standard Error (GPa)
2	50/50	DC	200	15.18	4.17	467	46.79
10	50/50	BPDC-50	600	25.31	1.95	293	8.75
17	33/67	DC	200	28.29	1.64	329	9.52
21	33/67	BPDC-50	0	14.96	2.10	279	22.31
38	20/80	BPDC-50	300	27.09	1.84	292	11.29

Die approbierte gedruckte Originalversion dieser Diplomarbeit ist an der TU Wien Bibliothek verfügbar
The approved original version of this thesis is available in print at TU Wien Bibliothek.
TU WIEN Bibliothek Your knowledge hub

Table A. 8. Values of the hardness and the elastic modulus before annealing

Number	Target	Sputter Mode	Substrate Temperature (°C)	Hardness (GPa)	Hardness Standard Error (GPa)	Elastic Modulus (GPa)	Elastic Modulus Standard Error (GPa)
1	50/50	DC	0	33.64	1.45	376	17.48
2	50/50	DC	200	30.47	1.97	405	17.84
3	50/50	DC	300	30.49	2.08	428	25.87
4	50/50	DC	450	28.86	2.31	390	14.24
5	50/50	DC	600	31.94	0.87	408	6.22
6	50/50	BPDC-50	0	31.59	1.52	385	12.03
7	50/50	BPDC-50	200	30.85	1.17	416	10.03
8	50/50	BPDC-50	300	29.27	1.60	488	13.13
9	50/50	BPDC-50	450	31.25	1.48	416	15.72
10	50/50	BPDC-50	600	38.21	2.45	504	37.89
11	50/50	BPDC-250	0	31.88	2.17	397	14.46
12	50/50	BPDC-250	200	31.66	1.90	437	16.01
13	50/50	BPDC-250	300	31.61	1.71	388	18.85
14	50/50	BPDC-250	450	36.25	1.13	391	8.49
15	50/50	BPDC-250	600	36.81	1.06	419	14.23
16	33/67	DC	0	17.02	0.28	185	2.18
17	33/67	DC	200	20.09	0.87	190	7.40
18	33/67	DC	300	20.96	1.13	228	7.30
19	33/67	DC	450	22.55	1.40	255	10.72
20	33/67	DC	600	29.91	0.79	276	8.78
21	33/67	BPDC-50	0	15.99	0.35	179	2.80
22	33/67	BPDC-50	200	17.29	0.84	202	4.41
23	33/67	BPDC-50	300	19.84	2.03	250	19.14
24	33/67	BPDC-50	450	23.22	0.83	250	6.27
25	33/67	BPDC-50	600	25.99	0.72	269	5.49
26	33/67	BPDC-250	0	14.85	0.94	169	12.76
27	33/67	BPDC-250	200	18.57	1.28	236	8.56
28	33/67	BPDC-250	300	25.50	2.63	361	31.92
29	33/67	BPDC-250	450	24.57	1.48	288	14.55
30	33/67	BPDC-250	600	27.11	0.92	263	6.61
31	20/80	DC	0	15.55	0.21	176	4.60
32	20/80	DC	200	22.02	0.43	220	2.48
33	20/80	DC	300	22.70	0.22	231	3.36
34	20/80	DC	450	23.46	0.76	257	5.42
35	20/80	DC	600	23.39	1.18	290	5.14
36	20/80	BPDC-50	0	14.39	0.28	174	1.92
37	20/80	BPDC-50	200	20.68	0.35	205	2.58
38	20/80	BPDC-50	300	21.25	0.72	202	1.96
39	20/80	BPDC-50	450	22.40	0.60	230	3.97
40	20/80	BPDC-50	600	24.61	0.63	247	4.15
41	20/80	BPDC-250	0	23.99	1.58	242	9.99
42	20/80	BPDC-250	200	21.32	2.12	292	37.41
43	20/80	BPDC-250	300	no measurement possible			
44	20/80	BPDC-250	450	21.72	2.02	289.00	52.49
45	20/80	BPDC-250	600	28.23	3.02	261.00	18.77

Die approbierte gedruckte Originalversion dieser Diplomarbeit ist an der TU Wien Bibliothek verfügbar
The approved original version of this thesis is available in print at TU Wien Bibliothek.
TU WIEN Bibliothek Your knowledge hub

All the following images were taken at a ten-thousand-fold magnification and 0.95 cm correspond to 1 µm.

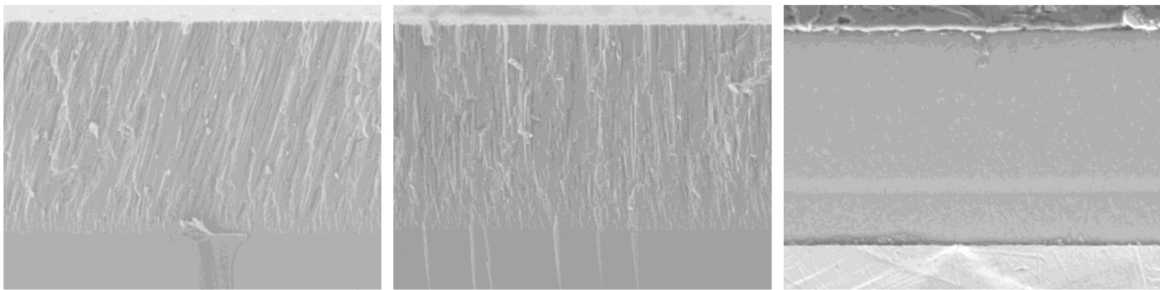

Figure A. 1. 50/50 target - DC mode - 200 °C.

Figure A. 2. 50/50 target - DC mode - 300 °C.

Figure A. 3. 50/50 target - DC mode - 450 °C.

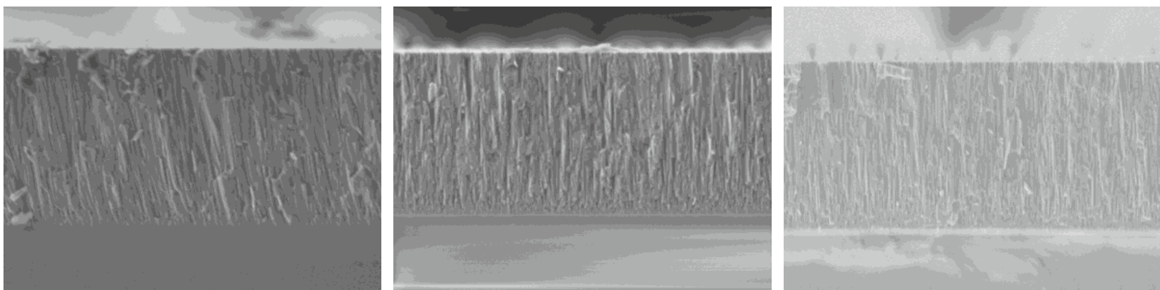

Figure A. 4. 50/50 target - BPDC-50 mode - 200 °C.

Figure A. 5. 50/50 target - BPDC-50 mode - 300 °C.

Figure A. 6. 50/50 target - BPDC-50 mode - 450 °C.

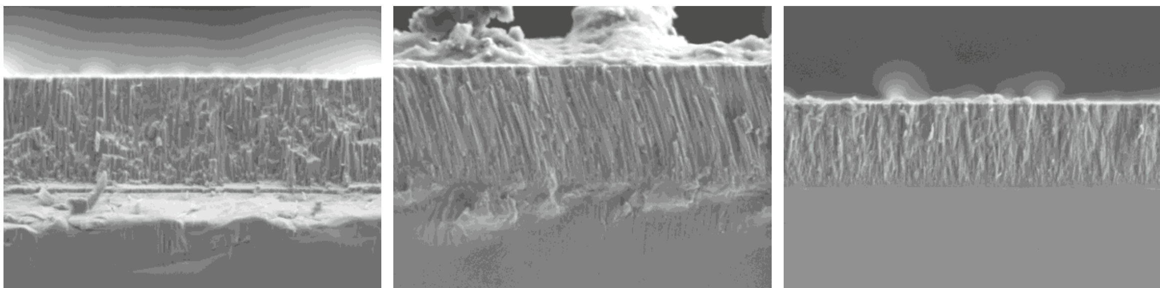

Figure A. 7. 50/50 target - BPDC-250 mode - 200 °C.

Figure A. 8. 50/50 target - BPDC-250 mode - 300 °C.

Figure A. 9. 50/50 target - BPDC-250 mode - 450 °C.

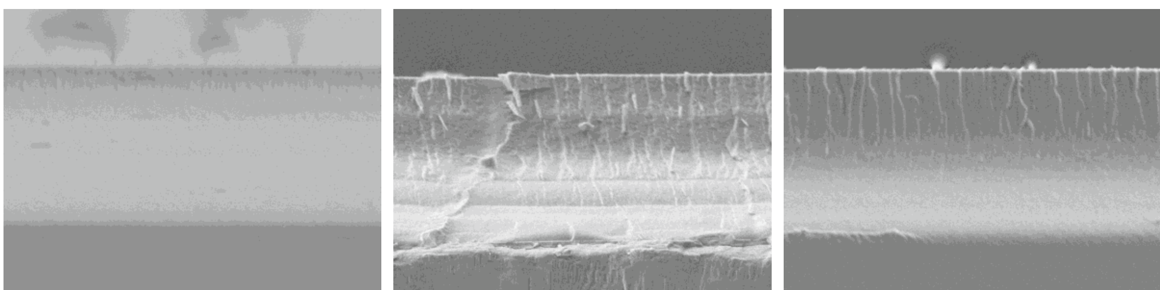

Figure A. 10. 33/67 target - DC mode - 200 °C.

Figure A. 11. 33/67 target - DC mode - 300 °C.

Figure A. 12. 33/67 target - DC mode - 450 °C.

Die approbierte gedruckte Originalversion dieser Diplomarbeit ist an der TU Wien Bibliothek verfügbar
The approved original version of this thesis is available in print at TU Wien Bibliothek.
TU WIEN Bibliothek Your knowledge hub

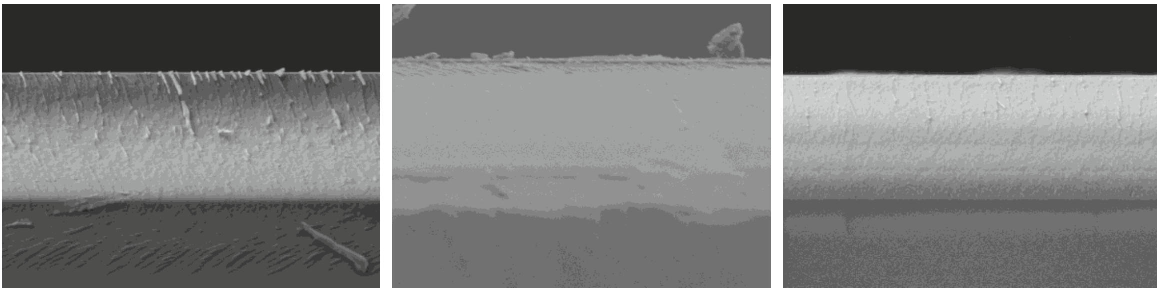

Figure A. 13. 33/67 target - BPDC-50 mode - 200 °C.

Figure A. 14. 33/67 target - BPDC-50 mode - 300 °C.

Figure A. 15. 33/67 target - BPDC-50 mode - 450 °C.

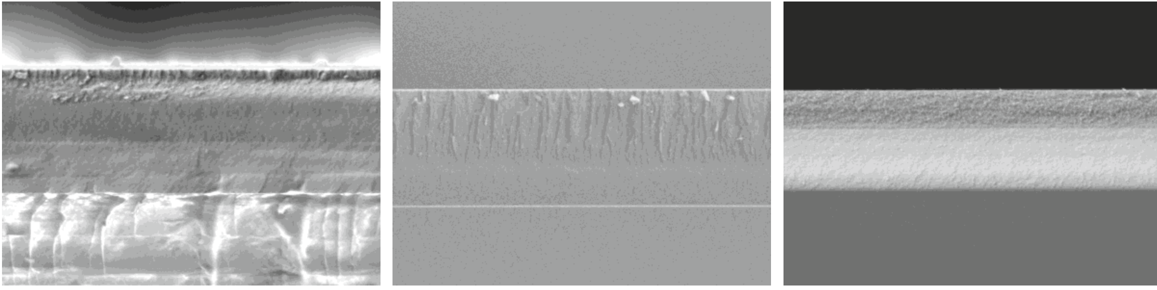

Figure A. 16. 33/67 target - BPDC-250 mode - 200 °C.

Figure A. 17. 33/67 target - BPDC-250 mode - 300 °C.

Figure A. 18. 33/67 target - BPDC-250 mode - 450 °C.

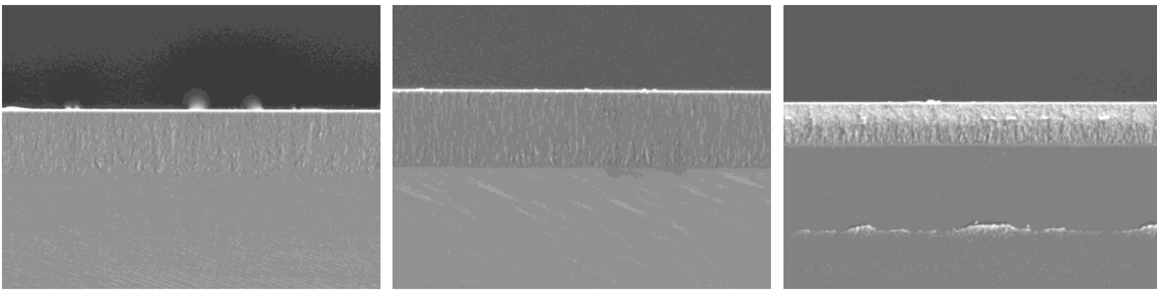

Figure A. 19. 20/80 target - DC mode - 200 °C.

Figure A. 20. 20/80 target - DC mode - 300 °C.

Figure A. 21. 20/80 target - DC mode - 450 °C.

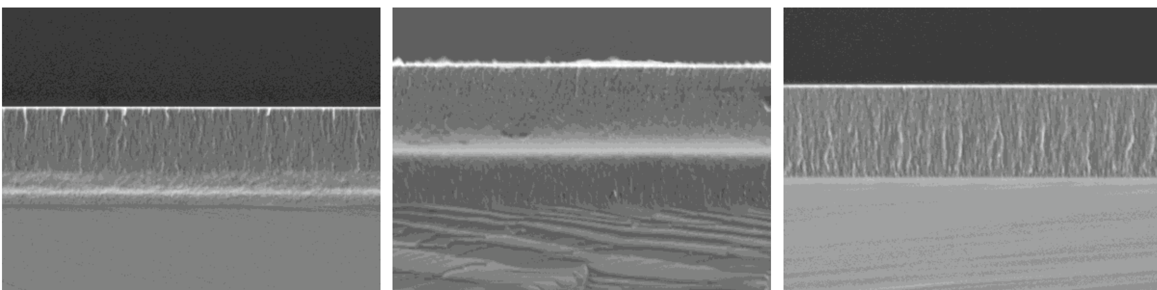

Figure A. 22. 20/80 target - BPDC-50 mode - 200 °C.

Figure A. 23. 20/80 target - BPDC-50 mode - 300 °C.

Figure A. 24. 20/80 target - BPDC-50 mode - 450 °C.

Die approbierte gedruckte Originalversion dieser Diplomarbeit ist an der TU Wien Bibliothek verfügbar
The approved original version of this thesis is available in print at TU Wien Bibliothek.
TU WIEN Bibliothek Your knowledge hub

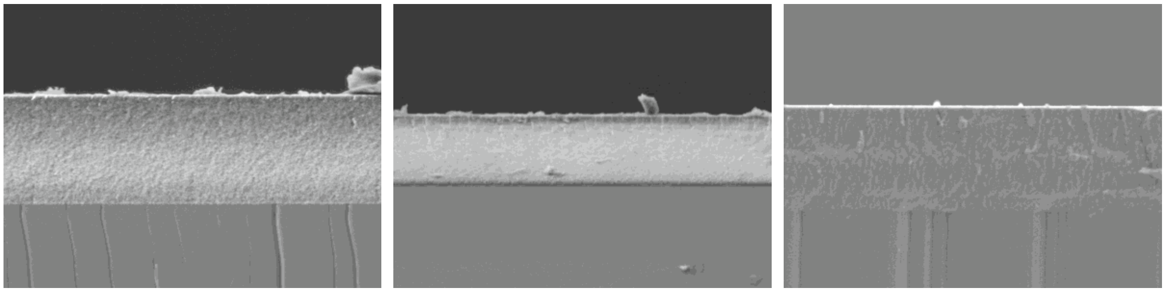

Figure A. 25. 20/80 target - BPDC-250 mode - 200 °C.

Figure A. 26. 20/80 target - BPDC-250 mode - 300 °C.

Figure A. 27. 20/80 target - BPDC-250 mode - 450 °C.

TU Bibliothek Your knowledge hub WIEN
Die approbierte gedruckte Originalversion dieser Diplomarbeit ist an der TU Wien Bibliothek verfügbar
The approved original version of this thesis is available in print at TU Wien Bibliothek.